SYNTHESIS OF THIOPHENE π-BRIDGE MODIFIED BENZODITHIOPHENE AND QUINOXALINE BASED CONJUGATED POLYMERS FOR ORGANIC BULK HETEROJUNCTION SOLAR CELL APPLICATIONS

A THESIS SUBMITTED TO
THE GRADUATE SCHOOL OF NATURAL AND APPLIED SCIENCES
OF
MIDDLE EAST TECHNICAL UNIVERSITY

BY

MELTEM TÜRKATAR

IN PARTIAL FULFILLMENT OF THE REQUIREMENTS
FOR
THE DEGREE OF MASTER OF SCIENCE
IN
POLYMER SCIENCE AND TECHNOLOGY

JUNE 2025

Approval of the thesis:

SYNTHESIS OF THIOPHENE π-BRIDGE MODIFIED BENZODITHIOPHENE AND QUINOXALINE BASED CONJUGATED POLYMERS FOR ORGANIC BULK HETEROJUNCTION SOLAR CELL APPLICATIONS

submitted by **MELTEM TÜRKATAR** in partial fulfillment of the requirements for the degree of **Master of Science** i**n Polymer Science and Technology, Middle East Technical University** by,

Prof. Dr. Naci Emre Görür
Dean, **Graduate School of Natural and Applied Sciences** _____

Prof. Dr. Necati Özkan
Head of the Department, **Polymer Science and Technology** _____

Prof. Dr. Ali Çırpan
Supervisor, **Chemistry, METU** _____

Dr. Gönül Hızalan Özsoy
Co-Supervisor, **GÜNAM, METU** _____

Examining Committee Members:

Prof. Dr. Necati Özkan
Polymer Science and Technology, METU _____

Prof. Dr. Ali Çırpan
Chemistry, METU _____

Prof. Dr. Gülay Ertaş
Chemistry, METU _____

Prof. Dr. İrem Erel Göktepe
Chemistry, METU _____

Prof. Dr. Yasemin Arslan Udum
Chemistry and Chemical Processing Technologies, Gazi University _____

Date: 13.06.2025

I hereby declare that all information in this document has been obtained and presented in accordance with academic rules and ethical conduct. I also declare that, as required by these rules and conduct, I have fully cited and referenced all material and results that are not original to this work.

Name Last name : Meltem Türkatar

Signature :

ABSTRACT

SYNTHESIS OF THIOPHENE π-BRIDGE MODIFIED BENZODITHIOPHENE AND QUINOXALINE BASED CONJUGATED POLYMERS FOR ORGANIC BULK HETEROJUNCTION SOLAR CELL APPLICATIONS

Türkatar, Meltem
Master of Science, Polimer Science and Technology
Supervisor : Prof. Dr. Ali Çırpan
Co-Supervisor: Dr. Gönül Hızalan Özsoy

June 2025, 133 pages

In this study, six different donor-acceptor type benzodithiophene–quinoxaline-based conjugated polymers were synthesized via Stille cross-coupling reaction, incorporating a thiophene π-bridge, to investigate the effect of monofluorinated, difluorinated and dichlorinated quinoxaline units on device performance. Structural diversity was achieved by employing two distinct BDT cores one bearing a thienothiophene unit synthesized during this study, and the other a commercially available BDT with chlorine-substituted side chains, alongside systematic variation of halogen substituents on the quinoxaline unit. The six polymers are systematically categorized based on their quinoxaline halogenation and BDT core structures: **P1**, **P3**, and **P5** incorporate a thienothiophene-based BDT unit, while **P2, P4**, and **P6** utilize a chlorine-substituted BDT. Regarding the acceptor moiety, **P1** and **P2** feature difluorinated quinoxaline, **P3** and **P4** contain dichlorinated quinoxaline, and **P5** and **P6** are based on monofluorinated quinoxaline. The synthesized polymers were characterized using Nuclear Magnetic Resonance (NMR), Gel Permeation Chromatography (GPC), Thermal Gravimetric Analysis (TGA), UV-Vis

Spectrometry, and Differential Pulse Voltammetry (DPV). The polymers exhibited E_g^{op} values of 1.72–1.98 eV and HOMO/LUMO levels ranging from −5.62/−3.86 to −6.26/−3.81 eV. The synthesized polymers were employed in the fabrication of organic solar cell devices using an architecture consisting of ITO/PEDOT:PSS/Donor:Acceptor/PDINN or PDINO/Ag. Conjugated polymer:acceptor-based organic solar cells were fabricated in a nitrogen-filled glove box, and their current–voltage characteristics were analyzed under AM 1.5G light using a solar simulator.The performances of the best devices are 5.99% for **P1**, 8.16% for **P2**, 1.48% for **P3**, 4.84% for **P5**, and 7.02% for **P6**.

Keywords: Benzodithiophene, Thiophene, Quinoxaline, Solar Cells, Polymers.

ÖZ

ORGANİK TOPLU HETEROJONKSIYON GÜNEŞ HÜCRESİ UYGULAMALARI İÇİN TİYOFEN π-KÖPRÜSÜ MODİFİYE BENZODİTİYOFEN VE KİNOKSALİN TEMELLİ KONJUGE POLİMERLERİN SENTEZİ

Türkatar, Meltem
Yüksek Lisans, Polimer Bilim ve Teknolojisi
Tez Yöneticisi: Prof. Dr. Ali Çırpan
Ortak Tez Yöneticisi: Dr. Gönül Hızalan Özsoy

Haziran 2025, 133 sayfa

Bu çalışmada, cihaz performansı üzerinde monoflorlanmış, diflorlanmış ve diklorlanmış kinoksalin ünitelerinin etkisini araştırmak için, bir tiyofen π köprüsü içeren, Stille çapraz-bağlantı reaksiyonu yoluyla altı farklı donör-akseptör tipi benzoditiyofen-kinoksalin bazlı konjuge polimer sentezlendi. Yapısal çeşitlilik, biri bu çalışma kapsamında sentezlenen tiyenotiyofen içeren ve diğeri klor ikame edilmiş yan zincirlere sahip ticari olarak temin edilen iki farklı BDT çekirdeği ile, ayrıca kinoksalin ünitesindeki halojen ikamelerinin sistematik olarak değiştirilmesiyle sağlandı. Altı polimer, kinoksalin ünitesindeki halojenleme derecesi ve BDT çekirdek yapısına göre sistematik olarak sınıflandırıldı: **P1**, **P3** ve **P5** tiyenotiyofen temelli BDT içerirken; **P2**, **P4** ve **P6** polimerlerinde ise klor ikame edilmiş BDT kullanıldı. Akseptör birimine bakıldığında, **P1** ve **P2** diflorlu kinoksalin, **P3** ve **P4** diklorlu kinoksalin, **P5** ve **P6** ise monoflorlu kinoksalin kullanılarak sentezlendi. Sentezlenen polimerler Nükleer Manyetik Rezonans (NMR), Jel Geçirgenlik Kromatografisi (GPC), Termal Gravimetrik Analiz (TGA), UV-Vis Spektrometrisi ve Diferansiyel Darbe Voltametrisi (DPV) kullanılarak karakterize edildi.

Polimerlerin E_g^{op} değerleri 1.72–1.98 eV aralığında, HOMO/LUMO enerji seviyeleri ise −5.62/−3.86 ile −6.26/−3.81 eV aralığında tespit edildi. Sentezlenen polimerler, ITO/PEDOT:PSS/Donör:Akseptör/PDINN veya PDINO/Ag yapısal düzenine sahip organik güneş pili cihazlarının üretiminde kullanıldı. Konjüge polimer:akseptör bazlı organik güneş pilleri, azot atmosferinde çalışan bir eldivenli kabin sistemi içerisinde üretildi ve akım-gerilim karakteristikleri AM 1.5G ışığı altında bir güneş simülatörü kullanılarak analiz edildi. En iyi cihazların verimleri; **P1** için %5,99, **P2** için %8,16, **P3** için %1,48, **P5** için %4,84 ve **P6** için %7,02 olarak belirlendi.

Anahtar Kelimeler: Benzoditiyofen, Tiyofen, Kinoksalin, Güneş Hücreleri, Polimerler.

To my family and friends…

ACKNOWLEDGMENTS

I would like to express my sincere gratitude to Prof. Dr. Ali Çırpan for giving me the opportunity to conduct my research at ÇRG laboratory and for introducing me to the world of academia.

I am sincerely grateful to Dr. Gönül Hızalan Özsoy, my co-advisor, for her consistent support, insightful guidance, and clarity throughout the critical stages of this study.

I would like to thank Dr. Elif Demir Arabacı for her kind support during the thesis writing process and her invaluable emotional encouragement.

I also thank Oğuzhan Karakurt for his inspiring analytical thinking, disciplined approach, and generous knowledge-sharing.

I appreciate Duygu Yalvaç for her contributions to photovoltaics, which offered valuable perspective during my research.

I am grateful to Sevgi Aydın for being a constant source of calm and kindness. Her quiet strength and heartfelt presence reminded me that even in the busiest times, genuine connection matters most.

I am truly grateful to Cem Maraşlıoğlu for his sincere friendship, which brought motivation, comfort, and laughter throughout this journey. His presence made even the hardest days lighter, and his support and kindness have left a lasting mark on both my academic and personal life.

I am endlessly thankful to Alper Çürük, whose love and support have been the heart of this journey. In moments of doubt, he reminded me of my worth; in moments of exhaustion, he lifted me with his quiet presence and endless support. Sharing this chapter of my life with him has been the greatest gift of all.

To my brother Ozan Mert Türkatar, my mother Şengül Türkatar, and my father Şükrü Türkatar thank you for being the kind of family whose support I never had to question. I always knew you were there, fully and unconditionally. In every decision I made, I felt your quiet confidence in me. That steady presence gave me the courage to move forward, even when things felt uncertain. More than anything, I'm grateful for the comfort of knowing I could always rely on you without asking, without explaining.

This study is supported by the Scientific and Technological Research Council of TURKEY (TUBITAK) with project number 222Z151.

TABLE OF CONTENTS

ABSTRACT v

ÖZ vii

ACKNOWLEDGMENTS x

TABLE OF CONTENTS xii

LIST OF TABLES xv

LIST OF FIGURES xvi

LIST OF ABBREVIATIONS xx

LIST OF SYMBOLS xxv

CHAPTERS

1 INTRODUCTION 1

1.1 Polymers 1

1.2 Conjugated Polymers 2

1.3 Low Band Gap Conjugated Polymers 3

1.4 Palladium-Catalyzed Cross-Coupling Reactions 4

1.4.1 Stille Cross-Coupling Reaction 5

1.4.2 Mechanism of Stille Cross-Coupling Reaction 6

1.5 Applications of Conjugated Polymers 8

1.6 Organic Solar Cells 9

1.6.1 Device Architectures of Organic Solar Cells 10

1.6.2 Working Principle of Organic Solar Cells 13

1.6.3 Performance of Organic Solar Cells 19

1.6.4 Analysis of Organic Solar Cell Metrics 20

1.7 Structural Improvements in Organic Solar Cells 22
1.7.1 Active Layer 22
1.7.2 Fullerene and Non-Fullerene Acceptor Unit 23
1.7.3 Polymeric Donor Unit 25
1.8 Literature Research 37
1.9 Aim of the Study 40
2 RESULTS AND DISCUSSION 43
2.1 Gel Permeation Chromatography 43
2.2 Optical Studies 44
2.3 Electrochemical Studies 50
2.4 Photovoltaic Characterizations 54
2.4.1 P1-Based Device 54
2.4.2 P2-Based Device 58
2.4.3 P3-Based Device 60
2.4.4 P4-Based Device 62
2.4.5 P5-Based Device 63
2.4.6 P6-Based Device 65
3 EXPERIMENTAL PART 71
3.1 Materials 71
3.2 Instrumentation and Methods 71
3.3 Synthesis Pathway of Acceptor Monomers 72
3.3.1 Synthesis Pathway of Molecule 2 73
3.3.2 Synthesis Pathway of Molecule 3 73
3.3.3 Synthesis Pathway of Molecules 7, 8, 9 74

3.3.4 Synthesis Pathway of Molecules 10, 11, 12 75
3.3.5 Synthesis Pathway of Molecules 13, 14, 15 76
3.3.6 Synthesis Pathway of Molecules 16, 17, 18 77
3.3.7 Synthesis Pathway of Molecules 19, 20, 21 78
3.3.8 Synthesis Pathway of Molecule 29 80
3.3.9 Synthesis Pathway of Molecules 22, 23, 24 81
3.3.10 Synthesis Pathway of Acceptor Monomers (Molecules 25, 26, 27) . 82
3.4 Synthesis Pathway of Donor Monomers 84
3.4.1 Synthesis Pathway of Donor Monomer 1 84
3.4.2 Synthesis Pathway of Donor Monomer 2 85
3.5 Synthesis Pathway of Polymers 86
3.5.1 Synthesis Pathway of P1 86
3.5.2 Synthesis Pathway of P3 87
3.5.3 Synthesis Pathway of P5 88
3.5.4 Synthesis Pathway of P2 89
3.5.5 Synthesis Pathway of P4 90
3.5.6 Syntesis Pathway of P6 91
4 CONCLUSIONS 93
REFERENCES 95
APPENDICES
A. Nuclear Magnetic Resonance 113
B. High Resolution Mass Spectrometry 129
C. Thermogravimetric Analysis 131

LIST OF TABLES

TABLES

Table 1.1 Photovoltaic properties of literature review polymers 40
Table 2.1 Gel Permeation Chromatography results of six synthesized polymers .. 44
Table 2.2 Optical properties of six synthesized polymers 45
Table 2.3 Optical properties of literature review polymer and synthesized polymer P2 48
Table 2.4 Electrochemical properties of six synthesized polymers 51
Table 2.5 Device performance of P1-based device..... 55
Table 2.6 Device performance of P2-based device..... 58
Table 2.7 Device performance of P3-based device..... 61
Table 2.8 Device performance of P5-based device..... 63
Table 2.9 Device performance of P6-based device..... 65
Table 3.1 Reactants and yields of Molecule 8 and Molecule 9 75
Table 3.2 Reactants and yields of Molecule 11 and Molecule 12 76
Table 3.3 Reactants and yields of Molecule 14 and Molecule 15 77
Table 3.4 Reactants and yields of Molecule 17 and Molecule 18 78
Table 3.5 Reactants and yields of Molecule 20 and Molecule 21 79
Table 3.6 Reactants and yields of Molecule 23 and Molecule 24 82
Table 3.7 Reactants and yields of Molecule 25 and Molecule 26 83

LIST OF FIGURES

FIGURES

Figure 1.1. Shows the general mechanism of Pd-catalyzed reactions 5
Figure 1.2. Mechanism of the oxidative addition step 7
Figure 1.3. Mechanism of the transmetalation step 7
Figure 1.4. Mechanism of the reductive elimination step 8
Figure 1.5. Device structure of single layer OSC 11
Figure 1.6. Device Structure of bilayer OSC 12
Figure 1.7. Device structure of bulk heterojunction solar cells 13
Figure 1.8. Working principle of OSC 14
Figure 1.9. Device structure of bulk heterojunction solar cell used in this thesis study 19
Figure 1.10. J-V curves of a solar cell in the dark and under illumination (Petrus, 2014) 20
Figure 1.11. Structures of Y6 and ITIC 25
Figure 1.12. Main parts of donor 26
Figure 1.13. Structure of PBDB-TF polymer 28
Figure 1.14. Structure of PBQ6 polymer 29
Figure 1.15. Structures of PTPD[2F]T(2HD) and PTPD[2F]T(2DT) 34
Figure 1.16. Structures of Z1 and Z2 polymers 37
Figure 1.17. Structures of literature review polymers 39
Figure 1.18. Structures of synthesized polymers fort his thesis study 42
Figure 2.1. Normalized absorption spectra of polymers in solution and thin film .. 46
Figure 2.2. Differential pulse voltammogram of the polymers in 0.1 M $TBAPF_6$/ACN 52
Figure 2.3. Energy level diagram of P1-based device 54
Figure 2.4. J-V characteristics of P1:Y6 with 2500 and 3000 rpm coating rates 57

Figure 2.5. J-V characteristics of a) P1:Y6 with 0.6% CN and 1% DIO and b) P1:Y6 with 1%DIO with 2500 and 300 rpm 57
Figure 2.6. J-V characteristics of a) P1:ITIC-Th with 0.6% CN and b) P1:ITIC-Th with 1% DIO 57
Figure 2.7. Energy level diagram of P2-based device 58
Figure 2.8. J-V characteristics of P2:Y6 with a) 2500 rpm and b) 3000 rpm..... 60
Figure 2.9. J-V characteristics of P2:Y6 with PDINO..... 60
Figure 2.10. Energy level diagram of P3-based device 60
Figure 2.11. J-V characteristics of P3:Y6 with 2500 rpm coating rate and P3:Y6 with 3000 rpm coating rate 62
Figure 2.12. Energy level diagram of P5-based device 63
Figure 2.13. J-V characteristics of a) P5:Y6 with 2500 rpm coating rate and 10 minutes anneal and b) P5:Y6 with 3000 rpm coating rate and 10 minutes anneal . 64
Figure 2.14. J-V characteristics of P5:Y6 with 5 minutes anneal..... 65
Figure 2.15. Energy level diagram of P6-based device 65
Figure 2.16. J-V characteristic of a) P6:Y6 with 2500 rpm coating rate and b) P6:Y6 with 3000 rpm coating rate 66
Figure 2.17. EQE spectrum of the polymers..... 67
Figure 3.1. Synthesis pathway of acceptor monomers 72
Figure 3.2. Synthesis Pathway of Molecule 29..... 80
Figure 3.3. Synthesis Pathway of Donor Monomer 1..... 84
Figure 3.4. Structure of donor monomer 2 85
Figure 3.5. Synthesis pathway of P1..... 86
Figure 3.6. Synthesis pathway of P3..... 87
Figure 3.7. Synthesis Pathway of P5 88
Figure 3.8. Synthesis pathway of P2..... 89
Figure 3.9. Synthesis Pathway of P4 90
Figure 3.10. Synthesis pathway of P6..... 91
Figure A.1. ^{1}H NMR spectrum of **Molecule 2** in $CDCl_3$..... 113
Figure A.2. ^{13}C NMR spectrum of **Molecule 2** in $CDCl_3$ 114

Figure A.3. ^{1}H NMR spectrum of **Molecule 3** in $CDCl_3$ 114
Figure A.4. ^{13}C NMR spectrum of **Molecule 3** in $CDCl_3$ 115
Figure A.5. ^{1}H NMR spectrum of **Molecule 13** in $CDCl_3$ 115
Figure A.6. ^{13}C NMR spectrum of **Molecule 13** in $CDCl_3$ 116
Figure A.7. ^{1}H NMR spectrum of **Molecule 14** in $CDCl_3$ 116
Figure A.8. ^{13}C NMR spectrum of **Molecule 14** in $CDCl_3$ 117
Figure A.9. ^{1}H NMR spectrum of **Molecule 15** in $CDCl_3$ 117
Figure A.10. ^{13}C NMR spectrum of **Molecule 15** in $CDCl_3$ 118
Figure A.11. ^{1}H NMR spectrum of **Molecule 19** in $CDCl_3$ 118
Figure A.12. ^{13}C NMR spectrum of **Molecule 19** in $CDCl_3$ 119
Figure A.13. ^{1}H NMR spectrum of **Molecule 20** in $CDCl_3$ 119
Figure A.14. ^{13}C NMR spectrum of **Molecule 20** in $CDCl_3$ 120
Figure A.15. ^{1}H NMR spectrum of **Molecule 21** in $CDCl_3$ 120
Figure A.16. ^{13}C NMR spectrum of **Molecule 21** in $CDCl_3$ 121
Figure A.17. ^{1}H NMR spectrum of **Molecule 22** in $CDCl_3$ 121
Figure A.18. ^{13}C NMR spectrum of **Molecule 22** in $CDCl_3$ 122
Figure A.19. ^{1}H NMR spectrum of **Molecule 23** in $CDCl_3$ 122
Figure A.20. ^{13}C NMR spectrum of **Molecule 23** in $CDCl_3$ 123
Figure A.21. ^{1}H NMR spectrum of **Molecule 24** in $CDCl_3$ 123
Figure A.22. ^{13}C NMR spectrum of **Molecule 24** in $CDCl_3$ 124
Figure A.23. ^{1}H NMR spectrum of **Molecule 25** in $CDCl_3$ 124
Figure A.24. ^{13}C NMR spectrum of **Molecule 25** in $CDCl_3$ 125
Figure A.25. ^{1}H NMR spectrum of **Molecule 26** in $CDCl_3$ 125
Figure A.26. ^{13}C NMR spectrum of **Molecule 26** in $CDCl_3$ 126
Figure A.27. ^{1}H NMR spectrum of **Molecule 27** in $CDCl_3$ 126
Figure A.28. ^{13}C NMR spectrum of **Molecule 27** in $CDCl_3$ 127
Figure A.29. ^{1}H NMR spectrum of **Molecule 29** in $CDCl_3$ 127
Figure A.30. ^{13}C NMR spectrum of **Molecule 29** in $CDCl_3$ 128
Figure A.31. ^{1}H NMR spectrum of **Molecule 31** in $CDCl_3$ 128
Figure A.32. HRMS spectrum of **Molecule 25** 129

Figure A.33. HRMS spectrum of **Molecule 26** 129
Figure A.34. HRMS spectrum of **Molecule 27** 130
Figure A.35. Thermogram of **P1**..... 131
Figure A.36. Thermogram of **P2**..... 131
Figure A.37. Thermogram of **P3**..... 132
Figure A.38. Thermogram of **P4**..... 132
Figure A.39. Thermogram of **P5**..... 133
Figure A.40. Thermogram of **P6**..... 133

LIST OF ABBREVIATIONS

ABBREVIATIONS

GPC Gel Permeation Chromatography

TGA Thermal Gravimetric Analysis

UV-Vis Ultraviolet-visible spectroscopy

HRMS High Resolution Mass Spectrometry

DPV Differential Pulse Voltammetry

HOMO Highest occupied molecular orbital

LUMO Lowest unoccupied molecular orbital

FF Fill Factor

PCE Power Conversion Efficiency

J_{SC} Short Circuit Current

V_{OC} Open Circuit Voltage

PU Polyurethane

PVC Polyvinyl chloride

PTFE Polyvinyltetrafluoroethylene

OLED Organic Light-emitting Diodes

OECT Organic Electrochemical Transistors

LED Light-emitting Diodes

FET Field-effect Transistors

PPV Poly(phenylenevinylene)

PFP Poly(fluorene-co-phenylene)

PDA Polydiacetylenes

PPE Poly(p-phenylene ethynylene) and

PT Poly(thiophene)

CP Conjugated Polymer

D-A Donor-Acceptor

QX Quinoxaline

C-C Carbon-Carbon

Pd Palladium

OSC Organic Solar Cell

ITO Indıum Tin Oxide

PEDOT: PSS Poly(2,3-dihydrothieno-1,4-dioxin)-poly(styrenesulfonate)

PDINN N,N'-Bis{3-[3- (Dimethylamino)propylamino]propyl}perylene-3,4,9,10-tetracarboxylic diimide

LiF Lithium Fluoride

BHJ Bulk Heterojunction

E_b Exciton binding energy

$PC_{60}BM$ [6,6] phenyl-C60-butyric acid methyl ester

ETL Electron Transport Layer

HTL Hole Transport Layer

NFA Non-Fullerene Acceptor

V_{MPP} Voltage at Maximum Power Point

J_{MPP} Current Density at Maximum Power Point

MPP Maximum Power Point

P_{in} Input Power

P_m Maximum Power

OPV Organic Photovoltaic

LHE Light Harvesting Efficiency

NIR Near Infrared

ITIC-Th 3,9-bis(2-methylene-(3-(1,1-dicyanomethylene)indanone))-5,5,11,11-tetrakis(4-hexylphenyl)-dithieno[2,3-d:2',3'-d']-s-indaceno[1,2-b:5,6-b']dithiophene

BDD benzo[1,2-c:4,5-c′]-dithiophene-4,8-dione

BDT benzo[1,2-b:4,5-b′]dithiophene

TDz thiadiazole

ICT Intermolecular Charge Transfer

TT thieno, [3,2-b]thiophene

BT benzothiadiazole

Da Dalton

Mn Number Average Molecular Weight

Mw Weight Average Molecular Weight

PDI Polydispersity İndices

eV Electron Volt

nm Nanometer

mL Milliliter

$TBAPF_6$ Tetrabutylammonium Hexafluorophosphate

ACN Acetonitrile

M Molar

DMSO Dimethyl Sulfoxie

TCI Tokyo Chemical Industry

TMS Trimethylsilane

PPM Parts per Million

TLC Thin-layer Chromatography

DCM Dichloromethane

$CHCl_3$ Chloroform

L_D Exciton Diffusion Length

$MgSO_4$ Magnesium sulfate

DMF N,N-Dimethylformamide

K_2CO_3 Potassium carbonate

$ALCl_3$ Aluminum chloride

$C_2O_2Cl_2$ Oxalyl chloride

HCl Hydrochloric acid

NaOH Sodium hydroxide

Na_2SO_4 Sodium sulfate

Sn Tin

N_2 Nitrogen gas

ET_3N Triethylamine

EtOAc Ethyl acetate

nBuLi n-Butyllithium

$SnBu_3Cl$ Tributylchlorostannane

THF Tetrahydrofuran

$SOCI_2$ Thionyl chloride

NBS N-Bromosuccinimide

H_2SO_4 Sulfuric acid

$NaBH_4$ Sodium borohydride

$PdCl_2(PPh_3)_2$ Bis(triphenylphosphine)palladium(II) chloride

TMEDA Tetramethylethylenediamine

$SnClMe_3$ Trimethyltin chloride

LIST OF SYMBOLS

SYMBOLS

E_g^{op} optical bandgap

E_g^{el} optical bandgap

η_{abs} the fraction of photons absorbed

λ lambda

E_{ox}^{onset} oxidation onset

E_{red}^{onset} reduction onset

J coupling constant

CHAPTER 1

INTRODUCTION

1.1 Polymers

A polymer is a large molecule formed by linking many smaller repeating units together. Both natural and synthetic polymers are found in many areas of everyday life due to their diverse range of properties. The word "polymer" comes from the Greek words polus (meaning "many") and meros (meaning "parts"), and it refers to molecules made up of repeating units, which gives them a high molecular weight and certain characteristics (Patil et al., 2018) The field of polymer research is fairly new and explores substances such as plastics, rubbers, glues, paints, insulating materials, and different kinds of fibers, whether natural or synthetic (Feldman, 2008). The study of polymers began in the 1830s when Jöns Jacob Berzelius first used the word "polymer" to explain molecules made of repeating atom groups. Later, in 1920, Hermann Staudinger laid the groundwork for modern polymer science by suggesting that substances like rubber and cellulose are made up of long chains of monomers connected by covalent bonds. Staudinger studied chemically modified rubber from 1922 to 1930, offering additional proof for his macromolecular theory. Wallace H. Carothers and DuPont created polyamides, sometimes known as nylons, in 1928, demonstrating the presence of macromolecules and opening the route for synthetic fiber development. The "golden age" of polymer research occurred in the 1930s and 1940s, with the production of major synthetic polymers such as polyurethane (PU), polyvinyl chloride (PVC), neoprene, nylon, polystyrene, and polytetrafluoroethylene ("Teflon" or PTFE). Throughout the development of polymer science, certain discoveries attracted attention by introducing new materials and influencing multiple fields. One of the earliest major recognitions came in 1953, when Hermann Staudinger was awarded the Nobel Prize in Chemistry for showing that

macromolecules are made of linked units. A decade later, in 1963, Karl Ziegler and Giulio Natta received the same award for their breakthrough in catalytic processes, which opened the door to producing plastics like polyethylene and polypropylene on an industrial level. Methods were developed that made it possible to produce plastics such as polypropylene and polyethylene in large quantities. Over time, polymer science has made significant progress. Paul J. Flory, known for his contributions to this field, especially his work on molecular weight distribution and polymer behavior, was awarded the Nobel Prize in 1974. In 2000, Alan G. MacDiarmid, Alan J. Heeger, and Hideki Shirakawa won the Nobel Prize in Chemistry for the discovery of conductive polymers. This discovery greatly contributed to the development of organic electronics and laid the foundation for technologies such as OLEDs. Such developments demonstrate that polymer science is not just a theoretical framework but has come to play a central role in the development of today's technologies. This field, which started with Staudinger's idea of macromolecular structure, has become indispensable in the design of contemporary materials with Flory's work on polymer behavior and the discovery of conductive polymers. (Feldman, 2008).

1.2 Conjugated Polymers

Organic chains containing alternating σ and π bonds in their structures are called conjugated polymers. This regular bond structure enables delocalization of π electrons, which directly affects the electrical conductivity and optoelectronic properties of the material. These remarkable properties of conjugated polymers have long attracted the attention of scientists. In 1977, Shirakawa, Heeger and MacDiarmid showed that some conjugated polymers can conduct electricity, and this important discovery earned them the Nobel Prize in Chemistry in 2000 (Shirakawa et al., 1977). People have shown growing interest in these materials ever since, mainly because of their usefulness and the exciting possibilities they offer for future technologies. Some of the applications where conjugated polymers have been investigated are as follows: solar cells, organic electrochemical transistors (OECT),

light-emitting diodes (OLED), field-effect transistors (OFET), energy storage devices, biosensors, and most recently, chemosensors. In the last few years, many conjugated polymers have been designed and synthesized thanks to their similar conjugated backbone structures. These polymers include different forms that can be classified according to their backbone structures, such as poly(phenylenevinylene) (PPV), poly(fluorene-co-phenylene) (PFP), polydiacetylenes (PDA), poly(p-phenylene ethynylene) (PPE), and poly(thiophene) (PT) (B. Liu et al., 2003). Some of the processes frequently used in the production of different conjugated polymers are: Suzuki, Heck, Sonogashira, Wessling, photopolymerization, $FeCl_3$ oxidative polymerization, and Stille (Bao et al., 1993). In addition to these, conjugated polymers have potential advantages such as easy processability, better optical absorption, flexible structure, renewability, and a wider production range. (Yadav et al., 2022) This thesis study provides an overview of synthesizing benzodithiophene and quinoxaline-based conjugated polymers (CPs) and their application in solar cells.

1.3 Low Band Gap Conjugated Polymers

There are several important factors in determining the optical and electrical properties of a conjugated polymer. These factors can be listed as the energy positions of the HOMO-LUMO energy levels. These factors, which are important in determining the optical and electrical capabilities, also have an impact on the overall photovoltaic performance. Since conjugated polymers have smaller optical band gaps but can absorb light over a wider spectrum, the design of conjugated polymers is of increasing interest. However, one important consideration when designing conjugated polymers is to maintain the high attenuation coefficients of conjugated polymers without losing their strong light absorption ability. Researchers have been working on low-band gap polymers that mimic the properties of organic metals but do not require doping for more than two decades. There are several methods of narrowing the band gap, but studies have shown that the most important of these

methods is to increase the HOMO level of the polymer or decrease its LUMO level, while simultaneously compressing the HOMO-LUMO levels closer together has the same effect (Cheng et al., 2009). A common strategy for designing low band gap conjugated polymers involves the donor-acceptor (D-A) approach, where electron-rich and electron-poor units alternate along the polymer chain. Orbital hybridization between the donor and acceptor units of this polymer reduces the band gap (X. Zhao et al., 2021). This thesis uses the quinoxaline core as the acceptor unit and the benzodithiophene core as the donor unit of the donor polymers.

1.4 Palladium-Catalyzed Cross-Coupling Reactions

Carbon-carbon bonds, one of the most important parts of organic chemistry, are also one of the primary ways to do cross-coupling reactions. Research in this area dates back to Charles Adolphe Wurtz. Charles Adolph Wurtz tried to bond carbon atoms by experimenting with sodium metal, and these pioneering studies continued until the 19th century. Later, Wilhelm Rudolph Fittig continued these studies by Wurt, and later Fritz Ullmann expanded the studies by using metals such as copper in the early 20th century. In addition to these, Ullmann's studies using copper pioneered reactions such as Corey-House and Castro-Stephens and led to the development of similar reactions. In the 1970s, scientists gradually began to use palladium catalysts, and this situation slowly began to change the world of science. This step led to the development of various methods, some of which are Suzuki and Heck coupling reactions, which remain widely employed in modern organic synthesis (Salih & Baqi, 2020). Subsequently, researchers explored a variety of catalysts and ligands to improve the efficiency and selectivity of these reactions, particularly for structurally complex molecules. Ongoing studies now focus on the reuse of palladium, including its application in nanoparticle form. (Pagliaro et al., 2012) (Nicolaou et al., 2005). As a result, palladium-catalyzed reactions are now one of the most important ways to build complex chemical structures. These reactions play a major role, especially in drug development and the production of specialty fine chemicals. Actually, the

recognition of these methods is due to Suzuki, Heck, and Negishi receiving the Nobel Prize in 2010 (H. Li et al., 2012). Furthermore, palladium-based catalytic systems are extensively utilized in the synthesis of conjugated polymers, facilitating both monomer preparation and polymer chain formation via carbon–carbon bond-forming reactions (Nicolaou et al., 2005).

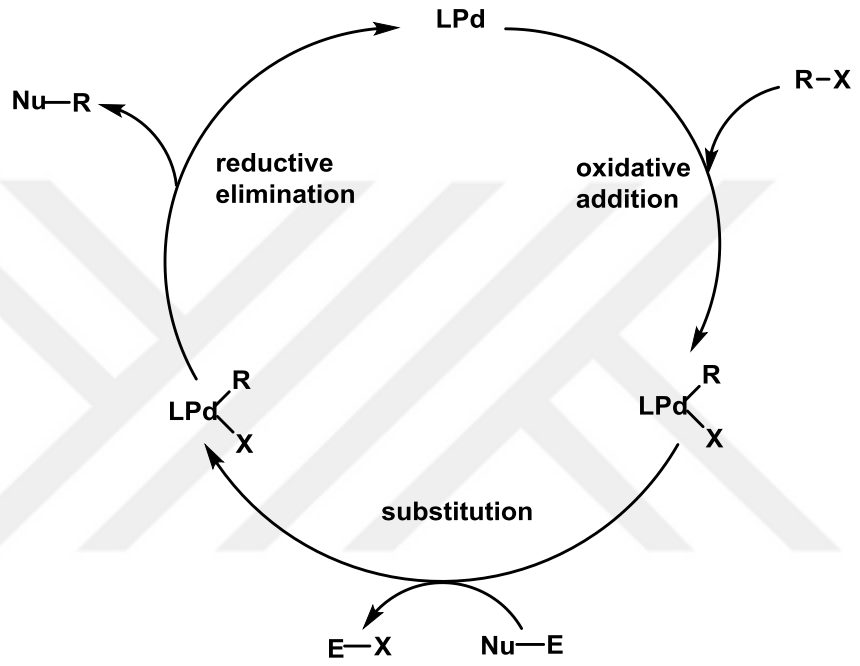


Figure 1.1. Shows the general mechanism of Pd-catalyzed reactions

1.4.1 Stille Cross-Coupling Reaction

The reaction involving palladium-catalyzed C–C bond formation via cross-coupling of vinyl organotin substrates with organic electrophiles, commonly referred to today as the Stille reaction, was initially introduced and later refined by the late Professor J. K. Stille in 1978 (Chemical, 1979). Nevertheless, the groundwork for this discovery had already been established by Kosugi and his team, who had published pioneering studies on transition-metal-catalyzed C-C bond formation using organotin compounds a year earlier. Almost three decades after its development, the

Stille reaction continues to be one of the most extensively utilized palladium-catalyzed methods for C-C bond formation. One of the key reasons for the widespread adoption of this method is its ability to proceed under relatively mild conditions, often with easily accessible starting materials. It also handles a wide variety of functional groups well, which makes it useful for building complex molecular architectures. The Stille reaction, in particular, has found a strong place in total synthesis. Its reliability and adaptability have led many researchers to select it for challenging synthetic targets. Its effectiveness in complex synthetic challenges highlights chemists' confidence in this transformation. Fundamentally, the Stille reaction can be considered a modified version of the Heck reaction, in which a hydrogen atom is substituted with a tin-containing group.(Espinet & Echavarren, 2004)

1.4.2 Mechanism of Stille Cross-Coupling Reaction

The three primary steps of the reaction mechanism are oxidative addition, transmetalation, and reductive elimination. In the case of organic halides acting as electrophiles, there is also a cis-to-trans isomerization that occurs before transmetalation. Although new ideas are constantly being proposed, the oxidative addition and reductive elimination are fairly well understood and shared by other catalytic coupling processes (Negishi, Hiyama, Suzuki etc.) (Nova et al., 2006).

1.4.2.1 Oxidative Addition

A Pd(II) complex is created in the first step when Pd(0) combines with an organic halide. This process builds a tetrasubstituted palladium complex by enabling the formation of a new palladium-carbon bond (Alfano et al., 2025). There is a fast equilibrium between the trans and cis square planar products. Most intermediates tend to shift into the trans form, mainly because the large ligands on the catalyst

make that version more stable from a thermodynamic point of view (Espinet & Echavarren, 2004).

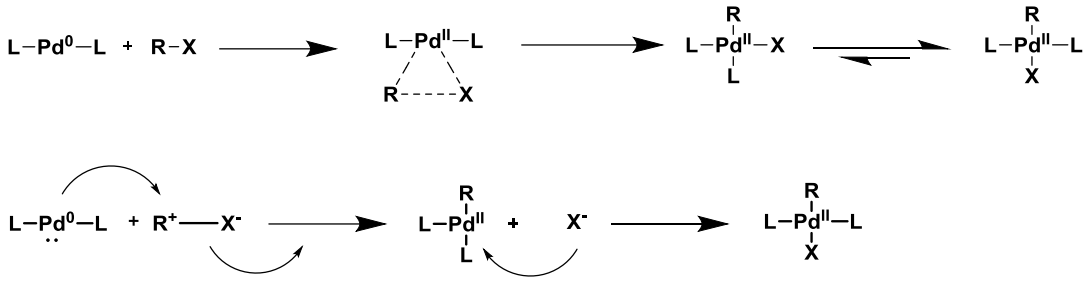


Figure 1.2. Mechanism of the oxidative addition step

1.4.2.2 Transmetalation

Depending on the type of reaction, the Pd(II) complex interacts with an organometallic nucleophile to form a new Pd complex bearing the desired organic moiety. (Alfano et al., 2025) In the case of tin-based nucleophiles, such as in the Stille reaction, the organostannane (R_1 –Sn) and the halide coordinated to the Pd(II) center form a transient four-membered cyclic intermediate. An 18-electron transition state is the outcome of this. Upon elimination of the tin halide byproduct, the R_2 group remains bound to the palladium center, setting the stage for the final reductive elimination step (Braga et al., 2013).

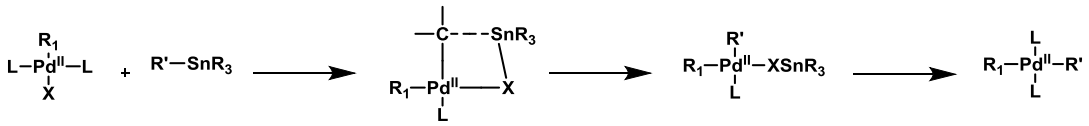


Figure 1.3. Mechanism of the transmetalation step

1.4.2.3 Reductive Elimination

The Pd(0) species is reformed when the new Pd complex releases a new C-C (or C-heteroatom) bond product. (Alfano et al., 2025) The reductive elimination step has three suggested mechanisms. The first method requires that both trans-R groups be in the trans conformation before the complex can be eliminated reductively. Another

way to approach this is by adding a second ligand to reach an 18-electron system, which leads to a trigonal pyramidal geometry. When this shape forms, the R groups are pushed into the equatorial positions, which helps trigger the formation of the C–C bond. There's also a different proposed pathway where the complex forms a 14-electron T-shaped structure. In that case, the process begins with ligands breaking away and ends with reductive elimination (Braga et al., 2013).

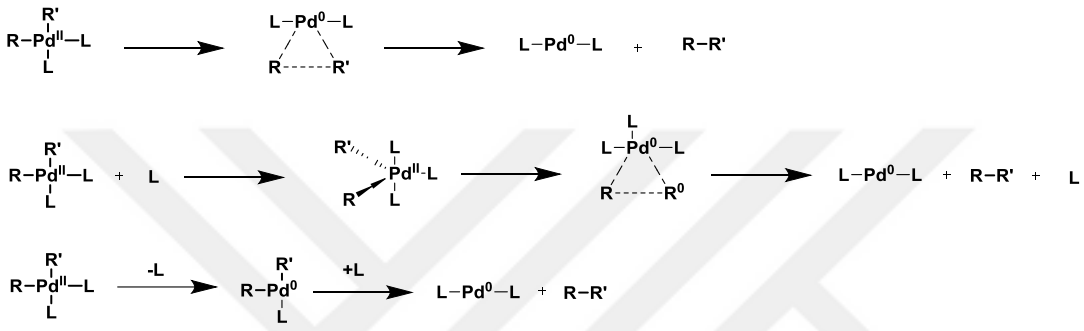


Figure 1.4. Mechanism of the reductive elimination step

1.5 Applications of Conjugated Polymers

Since the metals are poisonous and dangerous to the environment, conjugated polymers are potential candidates for various uses. The recent use of conjugated polymers in organic light-emitting diodes, organic solar cells, flexible electronic and display circuits, and sensors makes them promising materials (Nguyen, 2022). More importantly, these materials are inexpensive, easily deposited on large surface substrates, and have good electrical and physical qualities. Additionally, conjugated polymers can be used in batteries, radars, and corrosion protection (Harun et al., 2007). This thesis specifically focuses on the application of conjugated polymers in organic solar cells.

1.6 Organic Solar Cells

One of the most important issues of the twenty-first century is lowering the net carbon emissions to net zero to mitigate the effects of global warming. Achieving this within the remaining time for the 1.5 °C target will require efficiency measures and a rapid shift away from fossil fuels and towards sustainable technologies in the heating, electricity sectors and transportation (Riede et al., 2021). The most significant regenerative energy source is solar light, which is also the source of water power, biomass and wind. It is also the only limitless energy source available to humanity. On Earth, the annual energy input from solar radiation (43% visible, 52% infrared and 5% UV) is thousands of times greater than the annual energy consumption (Wohrle & Meissner, 1991). Fundamentally novel advancements are crucial for solar energy conversion. The direct conversion of solar energy into electrical energy in photovoltaic cells is one of today's most promising technologies. In this context, organic solar cells stand out due to their low cost, suitability and flexibility for roll-to-roll production (Cheng et al., 2009). Although research on organic solar cells has advanced over the past 30 years, a sharp rise in power conversion efficiencies in the last ten years has drawn considerable scientific and commercial interest (Hoppe & Sariciftci, 2004). Organic solar cells have certain features that make them stand out from older technologies like silicon-based or perovskite solar cells. For instance, they’re often much lighter, and they can bend or flex without getting damaged. Some designs even allow them to be more visually appealing, which can matter in architectural use. Another key point is that their light absorption can be adjusted depending on the materials used. Because of all this, different types of OSCs have been explored more seriously in the past decade, especially ones that are flexible, allow some light to pass through, or are made for indoor settings (J. Wu et al., 2021). In summary, the main benefits of OSCs are:

- OSC modules are lightweight and flexible.
- Transparency in part.
- Simple integration into different products.

- New market prospects, including wearable photovoltaics.
- Considerably cheaper production costs than traditional inorganic processes.
- OSC is continuously manufactured with cutting-edge printing equipment.
- Low environmental impact in production and operations and quick energy payback periods.

Organic solar cells (OSCs) have attracted extensive interest due to all of these benefits (Scharber & Sariciftci, 2013).

1.6.1 Device Architectures of Organic Solar Cells

Single, bilayer, and bulk heterojunction organic solar cells are the three categories into which organic solar cells belong.

1.6.1.1 Single Layer Organic Solar Cells

One of the simplest ways to make an organic solar cell is by using just a single layer of organic material between two electrodes. This setup often includes a conjugated polymer as the light-absorbing layer, placed between materials like indium tin oxide (ITO) and aluminum. Because the active layer in this kind of device is extremely thin which is usually only 10 to 20 nanometers, it isn't able to absorb much light, which means the amount of electricity it can generate is also limited (Kesinro et al., 2021). As for the internal electric field that helps separate charges in these cells, there's more than one possible source. In some cases, charge separation in single-layer organic solar cells arises from the formation of a Schottky barrier at the interface between the metal electrode and the organic semiconductor. In others, it's simply caused by the fact that the two electrodes have different work functions. Whatever the case, the choice of electrode materials can make a big difference in how the device ends up working. One common issue with these single-layer cells is their low fill factor (FF). This is often linked to how charges are generated in the material since it depends on the internal electric field; generation isn't always

efficient. Also, the organic layer itself can behave like an insulator, which increases resistance and further reduces efficiency (Tang, 1986).

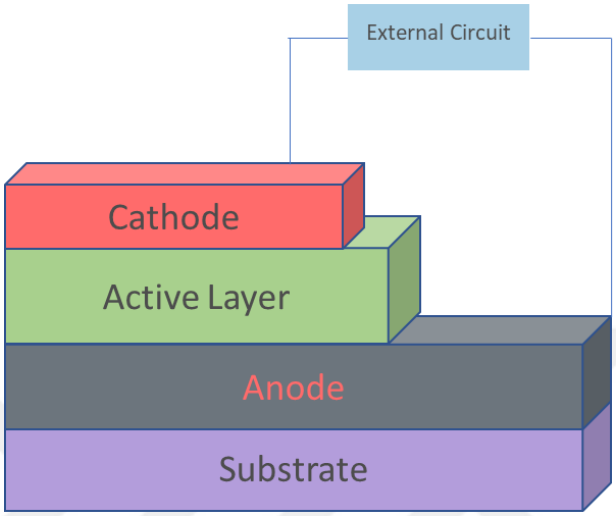


Figure 1.5. Device structure of single layer OSC

1.6.1.2 Bilayer Organic Solar Cells

One type of solar cell composed of organic materials is called a bilayer organic solar cell. It is composed of two separate layers that lie between electrodes. An acceptor layer promotes separating these charges so that electricity can flow after a donor layer absorbs sunlight and forms electron-hole pairs (Revoju, 2018). Due to their short diffusion lengths, excitons (electron-hole pairs) in bilayer organic solar cells only remain long enough to dissociate and contribute to the generation of charge; others undergo recombination. As a result, the donor-acceptor interface plays a crucial role in determining the device's photovoltaic performance. Bilayer structures allow for more effective charge generation at the interface, minimizing dependence on the bias field and greatly increasing the fill factor, in contrast to single-layer organic solar cells, where charge separation mainly depends on the built-in electric field. Furthermore, the characteristics of the organic-organic interface have a greater impact on the open-circuit voltage (V_{oc}) in bilayer cells than do the electrode-organic

interfaces, indicating that the electrodes mainly function as ohmic contacts (Tang, 1986). This difference shows why bilayer solar cells work better than single-layer ones, they separate charges more efficiently and generate more power overall. In 1986, Tang reported a bilayer solar cell with a high fill factor of 65% and approximately 1% PCE. The groundbreaking work, however, marked a significant turning point and opened the door for the creation of additional donor/acceptor type architectures (Revoju, 2018).

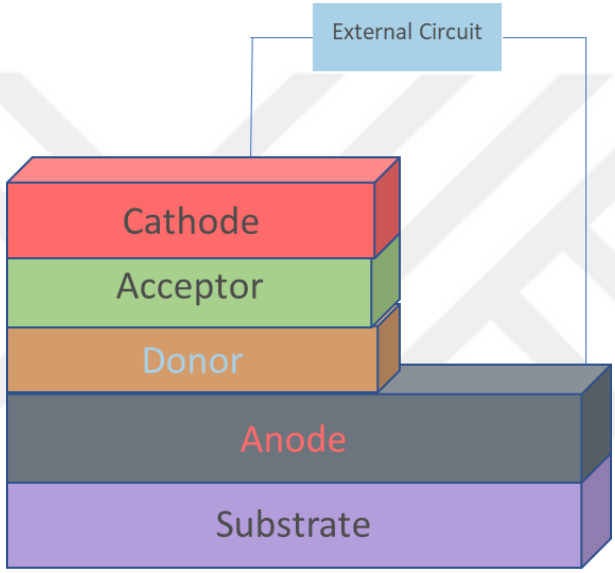


Figure 1.6. Device Structure of bilayer OSC

1.6.1.3 Bulk Heterojunction Solar Cells

Yu et al. first proposed the bulk-heterojunction architecture in 1995 as a solution to previous OSC designs' low photocurrent and short exciton diffusion length (G. Yu, J. Gao, J. C. Hummelen, F. Wudi, 1995). A bicontinuous interpenetrating donor-acceptor network with big interfacial areas is produced when donor and acceptor materials are blended in a typical BHJ structure. Such a bicontinuous nanoscale network produces an ideal domain size, which is advantageous for effective exciton diffusion and dissociation (D. Yang et al., 2019). Therefore, in addition to the opto-

electronics characteristics of the materials, the morphology of the blend layer also affects the performance of BHJ devices. But the formation of BHJ morphology is a complicated matter that depends on several factors, including the ratio of donor to acceptor, miscibility, and structural characteristics (backbone, substituents, and side chains), as well as different device fabrication techniques like solvent selection, solvent additives, and solvent and thermal annealing (Collins et al., 2017).

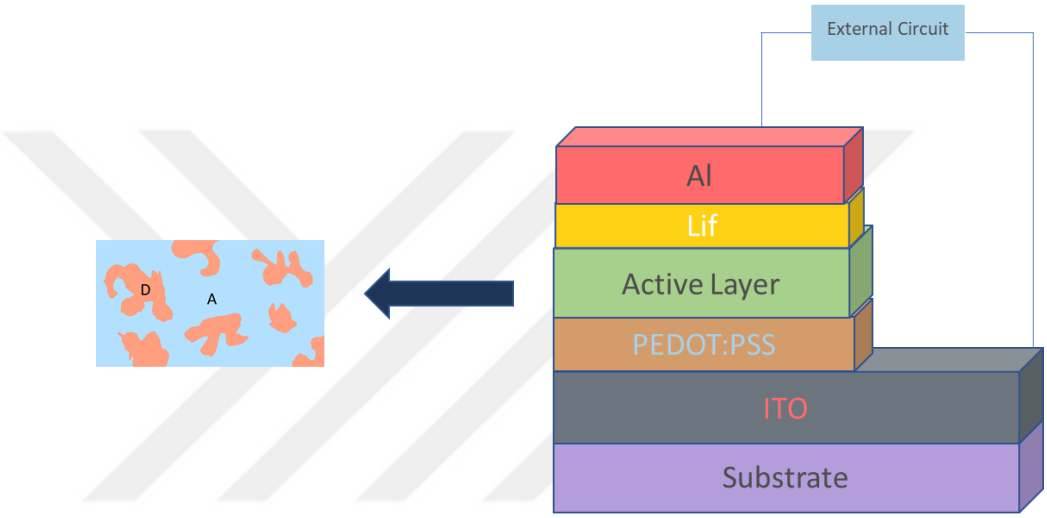


Figure 1.7. Device structure of bulk heterojunction solar cells

1.6.2 Working Principle of Organic Solar Cells

The conventional organic solar cell device has six layers. The process begins with a glass substrate onto which a transparent and conductive anode most commonly indium tin oxide (ITO) is deposited. This is followed by the deposition of an ultrathin layer of N'-Bis{3-[3-(dimethylamino)propylamino]propyl}perylene-3,4,9,10-tetracarboxylic diimide (PDINN), which serves as an interfacial layer. The focus of this thesis is the synthesis of donor-type polymeric materials intended for use in the active layer of organic solar cells. To facilitate efficient hole transport and enhance device performance, an interfacial layer of poly(3,4-ethylenedioxythiophene):poly(styrenesulfonate) (PEDOT:PSS) is incorporated to

the active layer. This is followed by the photoactive layer, which is then topped with an additional ultrathin interfacial layer typically lithium flüoride (LiF) and a thin silver cathode. The active layer itself generally consists of a conjugated polymer serving as the electron donor and an acceptor. In high-performance OSCs, the conjugated polymer donor and fullerene derivative acceptor constitute the core photovoltaic materials. Therefore, understanding the essential properties of these materials and how to design them effectively is crucial for advancing the development of efficient photovoltaic systems (Hou & Guo, 2013). The conversion process in organic solar cells starts with the production of excitons. Excitons (bounded electron-hole pairs) are formed when sunlight is absorbed by semiconducting donor and acceptor materials in the photoactive layer. These excitons diffuse to the donor/acceptor interfaces and dissociate into electrons on the acceptor's LUMO level and holes on the donor's HOMO level (Hou & Guo, 2013). The energy required to dissociate an exciton into free charge carriers is referred to as the exciton binding energy (E_b). Organic materials typically have E_b values ranging from 0.1-1.0 eV (Y. Zhu et al., 2022). The built-in electric field drives dissociated electrons and holes to negative and positive electrodes, where they are collected to convert photons to electrons (Hou & Guo, 2013).

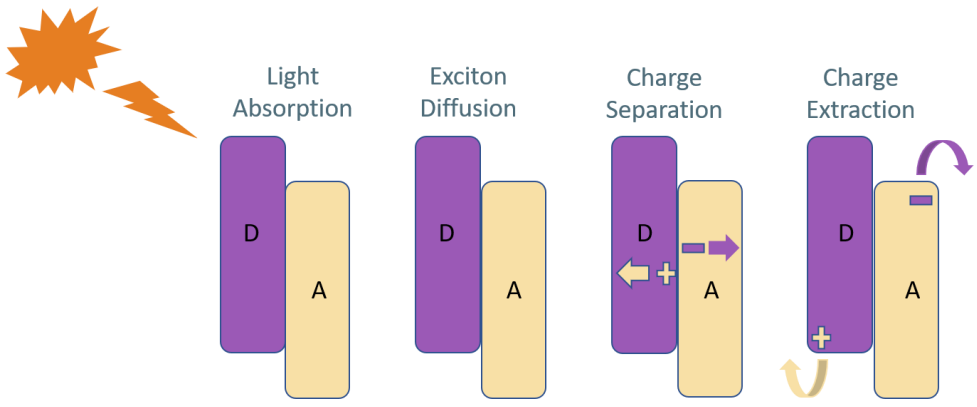


Figure 1.8. Working principle of OSC

1.6.2.1 Light Absorption

Polymers in solar cells must have a high absorption coefficient in the film state to be effective, as photon absorption is the fundamental principle of photovoltaic technology. For wavelengths longer than 400 nm, the acceptor component in the BHJ blend—typically $PC_{60}BM$ or $PC_{70}BM$—has poor absorption efficiency (J. Y. Kim et al., 2007). Consequently, the polymer's function is to absorb photons with wavelengths longer than 400 nm. The following are some strategies to increase the photoactive layer's light absorption:

1) Extending the photoactive layer's thickness (This approach is limited because the charge-carrier mobility of polymeric semiconductors can be as low as 10^{-4} $cm^2/V \cdot s$).
2) Increasing the absorption coefficient.
3) Matching the solar spectrum to the polymer's absorption (Hoppe & Sariciftci, 2004).

The device's series resistance increases dramatically as the thickness of the photoactive layer increases, making thick active layer devices difficult to operate. Since charge carriers are not very mobile, the short-circuit current (J_{SC}) might decrease. To achieve a photocurrent greater than 10 mA/cm^{-2}, in the film state, a high absorption coefficient (10^5 to 10^6) is preferred because increasing the thickness is limited (Hoppe & Sariciftci, 2004). Reducing the band gap allows the polymer to absorb light over a wider wavelength range, capturing photons with $\lambda >$ 800 nm (Ye & Chi, 2011).

1.6.2.2 Charge Generation

In organic solar cells (OSCs), charge generation is typically explained in stages, beginning with photon absorption in the active layer and ending with the extraction of free charge carriers at the electrodes (Clarke & Durrant, 2010). As excitons have a short lifetime, they must first migrate to the interface between the D-A phases of

the bulk heterojunction (BHJ) quickly in order to dissociate into free charges before recombining. This migration process participates in both radiative and non-radiative exciton decay mechanisms. An exciton's lifetime and exciton diffusion coefficient affect its diffusion length, which is usually between 5 and 20 nm (Bruno et al., 2013). Exciton diffusion length determines the maximum path an exciton can take before recombining. Long exciton diffusion lengths can have positive effects for organic photovoltaic systems. Sajjad and colleagues reported that long exciton diffusion lengths allow bulk heterojunctions to use larger donor-acceptor domain sizes, which provides better results in charge extraction and charge pair separation. Due to the increased phase separation, the larger exciton diffusion length can increase the tolerance of the ideal morphology of bulk heterojunctions, which can lead to reduced device degradation. (Sajjad et al., 2020).

1.6.2.3 Charge Separation

When the charge separation occurs, at the point of contact between the donor material and the acceptor, that is, at the interface, an electron is transferred from the donor to the acceptor, and thus the exciton turns into two separate charges, a free electron and a hole. Following separation, electrons travel toward the electron transport layer (ETL) and eventually the cathode via the acceptor phase, which is usually a fullerene derivative like PCBM or a non-fullerene acceptor like Y6 (Lattante, 2014). Before reaching the anode, holes migrate via the donor phase (conjugated polymer) and the hole transport layer (HTL). According to Yeh and his associates, a charge may recombine or become trapped in a disordered interpenetrating organic material on its way to the electrode, resulting in a decrease in efficiency (Yeh & Yeh, 2013). Sarıçifçi and his associates also propose that to balance the needs of charge transport and exciton dissociation, the phase separation between the donor and acceptor must have an ideal domain size (Hoppe & Sariciftci, 2004).

1.6.2.4 Charge Extraction

When the charge separation occurs, at the point of contact between the donor material and the acceptor, that is, at the interface, an electron is transferred from the donor to the acceptor, and thus the exciton turns into two separate charges, a free electron and a hole. Following separation, electrons travel toward the electron transport layer (ETL) and eventually the cathode via the acceptor phase (Lattante, 2014). Before reaching the anode, holes migrate via the donor phase (conjugated polymer) and the hole transport layer (HTL). According to Yeh and his associates, a charge may recombine or become trapped in a disordered interpenetrating organic material on its way to the electrode, resulting in a decrease in efficiency (Yeh & Yeh, 2013). Sarıçifçi and his associates also propose that to balance the needs of charge transport and exciton dissociation, the phase separation between the donor and acceptor must have an ideal domain size (Hoppe & Sariciftci, 2004).

1.6.2.5 Device Engineering and Characterization of Organic Solar Cells

As previously stated in the section on the working principle of organic solar cells, the device comprises six distinct layers. The process begins with a glass substrate, which is the most widely used substrate because of its stability, low cost, and extremely strong barrier qualities (Centre, 2012). The glass substrate is followed by a transparent and conductive anode. In this thesis study, ITO (Indium Tin-Oxide) is used as an anode due to its transparency and conductivity (Scharber & Sariciftci, 2013). The work function significantly affects the device's performance in organic solar cell applications. ITO can be used to inject holes into the highest occupied molecular orbitals (HOMO) of conjugated semiconductors rather than electrons into the lowest unoccupied molecular orbital (LUMO) because of its relatively large work function, which ranges from 4 to 5 eV, depending on the treatment. The drive voltage of the devices must rise because the HOMO for the majority of polymers is more than 5 eV below vacuum, creating a substantial energy barrier to hole injection

into the polymer. Inserting a hole transport layer could be a solution to the issue. According to Kim and his colleagues multiple groups have reported a significant increase in lifetime and luminous efficiency when a conducting polymer is inserted between the emissive layer and the indium-tin oxide anode, especially for poly(3,4-ethylenedioxythiophene)-poly(styrenesulfonate) (PEDOT: PSS)(J. S. Kim et al., 1998), which is used as hole transport layer in this thesis study. In this thesis, silver was used as cathode material, aluminum and copper can also be used as an alternative to silver cathode. The reason for not using Al as a cathode is that the OSCs with Al as a cathode show poor stability due to the high reactivity of the Al electrode in air. Studies show that replacing Al with Ag for the cathode typically results in a higher work function of the cathode, thus a lower open-circuit voltage (V_{OC}) of the OSCs due to a low built-in potential across the device (Page et al., 2014). With these concerns, in this thesis study Ag is used as cathode and PDINN (N'-Bis{3-[3-(Dimethylamino)propylamino]propyl}perylene-3,4,9,10-tetracarboxylic diimide) is used as cathode interlayer material. PDINN has a suitable dipole moment to reduce the work function of air stable metal Ag, and the secondary amine in the side chains of PDINN can form hydrogen bonds with the photovoltaic materials in the active layer, resulting in good contact with the active layer (J. Yao et al., 2020). In the middle of the device, there is an active (or photoactive) layer, and this active layer is formed by the combination of acceptor components such as quantum dots, polymers, or small molecules and donor materials such as fullerenes or non-fullerene-based structures. Within the scope of this thesis, a polymer was preferred as the donor material, and devices working with both non-fullerene-based (NFA) and fullerene-based acceptors were designed and developed.

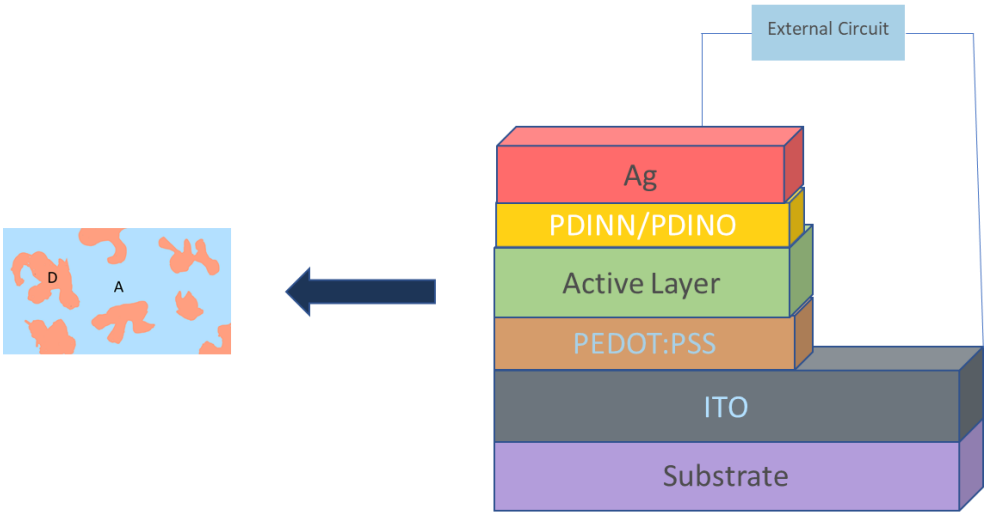


Figure 1.9. Device structure of bulk heterojunction solar cell used in this thesis study

1.6.3 Performance of Organic Solar Cells

There are four key factors that determine the performance of organic solar cells they are short-circuit current density (J_{SC}), open-circuit voltage (V_{OC}), fill factor (FF), and power conversion efficiency (PCE). By analyzing these factors, the efficiency of solar cell devices is evaluated, potential problems that may occur in the device are prevented, and areas for improvement of the device are determined. The maximum voltage that will occur across a solar cell if there is no external load is called V_{OC}. The maximum current that occurs when a short circuit occurs in a solar cell is called the short-circuit current (J_{SC}). The fill factor (FF) is a parameter that shows how close the J-V curve is to the square, and this value is directly related to the series and shunt resistances of the device.

The power conversion efficiency of a solar cell can be calculated from the J-V curve data taken in the AM 1.5 G spectrum and under a light intensity of 100 mW/cm² (standard sunlight conditions) (Benanti & Venkataraman, 2006). The AM 1.5 G spectrum is the light that reaches the Earth on a bright, sunny day when the sun is at an incident angle of 48.2 to the zenith. Measuring the J-V characteristics both under

illumination and in the dark is crucial for evaluating a photovoltaic device's performance. In the dark, a functional photovoltaic device behaves like a diode, ideally exhibiting high current density in the forward bias region and low leakage current in the reverse bias region.

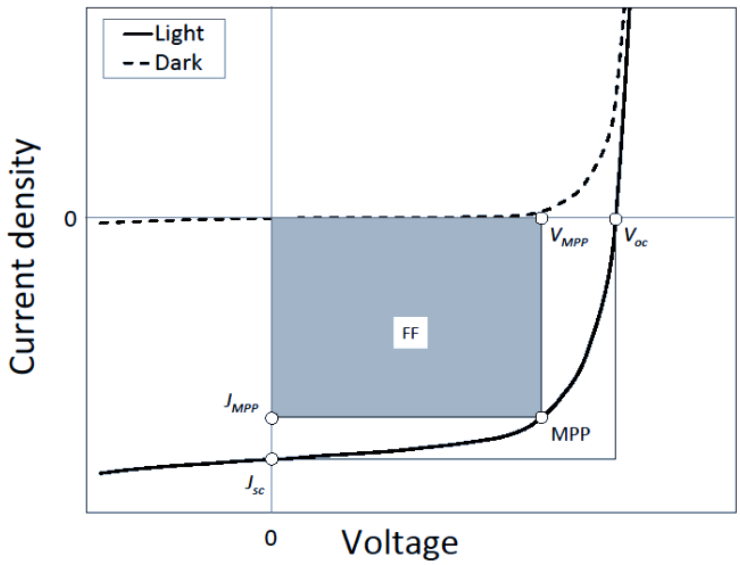


Figure 1.10. J- V curves of a solar cell in the dark and under illumination (Petrus, 2014)

1.6.4 Analysis of Organic Solar Cell Metrics

As previously mentioned, the performance of organic solar cells is determined by four key parameters, one of them is;

Open Circuit Voltage (V_{OC}): It stands for the highest voltage that the cell can produce when there is no current flowing through it. The maximum cell voltage and this value are the same. It has a direct bearing on the alignment of the energy levels in the solar cell and is a crucial metric for evaluating the device's capacity to produce electricity without a load. As a result, the parameter that reflects the quality of the absorber material used, the band gap and the main recombination mechanisms

operating inside the device is called V_{OC}. (Tvrdy & Kamat, 2011). Zhou and his colleagues state that the V_{OC} value of solar cells is equal to the energy difference between the HOMO energy level of the donor and the LUMO energy level of the acceptor (Zhou et al., 2012).

Fill Factor (FF): The parameter obtained by dividing the maximum power density by the V_{OC} and J_{SC} multiplier, which affects the performance of the device, is called the fill factor. The efficiency of collecting the charges and the leakage currents that may occur can be understood from the FF value. FF also indicates how square the J-V curve is. The ease with which carriers generated by light can be collected from the device can be understood by looking at this value. When the J-V curve is a rectangle, the optimal value for FF is unity (100%). The current density can rise perpendicular to the maximum value (J_{SC}) with only a small voltage deviation from the V_{OC} ($<V_{OC}$) (Qi & Wang, 2013). It can remain constant even when the applied voltage changes from V_{OC} to zero and even with a significant reversed bias. FF is unable to achieve 100%. The highest FF recorded is roughly 90%, even in inorganic solar cells, whose PCE is significantly greater than that of OSCs (Dongaonkar et al., 2010). The electrode interface, the layer thickness, and the equilibrium between electron and hole transport are a few of the variables that can affect the fill factor (M. S. Kim et al., 2009). FF is expressed by;

$$FF=\frac{P_m}{J_{SC}xV_{OC}} = \frac{J_m xV_m}{J_{SC}xV_{OC}}$$

Short Circuit Current (J_{SC}): In a condition where a solar cell is short-circuited—that is, when there is no potential difference across its terminals—the current that flows is identified as the short-circuit current. This current results from the generation and collection of charge carriers stimulated by light exposure. In an ideal scenario with negligible internal resistance, this current closely corresponds to the total amount of current generated by light absorption. Therefore, the short-circuit current serves as a key indicator of the solar cell's ability to generate current under illumination and is directly influenced by the absorption properties of the active layer and the efficiency of charge transport and collection (Dongaonkar et al., 2010).

Power Conversion Efficiency (PCE): The power conversion efficiency (PCE or η) is the parameter that shows the efficiency of a solar cell. This value can be calculated using the open circuit voltage, short circuit current and filling factor. The PCE value can be reached by dividing the maximum electrical power produced by the device to the total light energy it receives.

$$\text{PCE} = \frac{P_{MPP}}{P_{in}} = \frac{J_{SC} x V_{OC} x FF}{P_{in}}$$

This equation indicates that to enhance the efficiency of the solar cell, the short-circuit current, open-circuit voltage, and fill factor must be increased (Petrus, 2014).

1.7 Structural Improvements in Organic Solar Cells

1.7.1 Active Layer

The layers that make up an organic solar cell are the anode, cathode, electron transport layer and active layer, respectively. The morphology of the active layer is a very important issue for organic solar cells. For example, the dissociation of excitons into charge carriers and their subsequent extraction are greatly affected by the morphology of the active layer. The factors that determine the morphology of the active layer are its thickness, concentration and pre- and post-treatment (Khandelwal et al., 2023). For a long time, researchers have explored various methods to control the nano-morphology of thin films. One of the first major advances was the realization that the power conversion efficiency of BHJ could be significantly improved by post-production treatments such as thermal annealing under an applied external voltage (Hoppe & Sariciftci, 2004). Other applied methods include using solvents with appropriate boiling points to control evaporation, slowing down film drying during spin coating, matching the solubility properties of the materials, and applying the double-layer melting technique (Y. Kim et al., 2005). Recent studies have shown that chemical additives can serve as an alternative to post-processing for BHJs and can increase both PCE and the overall performance of OPV devices. These

additives are preferred due to their ease of application and are a practical solution for large-scale production processes that do not require complex conditions. (Moore, 2008).

1.7.2 Fullerene and Non-Fullerene Acceptor Unit

An ideal acceptor material should have three main properties:

1) An absorption range that can absorb a wide range of wavelengths to increase the light harvesting efficiency (LHE);
2) Well-designed lowest unoccupied molecular orbital (LUMO) energy level, which helps both increase the open circuit voltage and provides sufficient driving force for charge transfer (Guo et al., 2022).
3) To avoid inhibiting exciton dissociation and support charge transport, a nearly flat but slightly curved structure that allows strong π-π interactions between molecules without causing excessive aggregation is required.

Although fullerene-based acceptors are known for their spherical structure and high electron transport capabilities, their electronic behavior is mostly limited by their rigid molecular structure. Due to their rigid structure, their molecular structure cannot be easily modified and it is not possible to control their optoelectronic properties. The symmetric structure of fullerenes limits the low-energy electron transitions, thus reducing their ability to absorb light in the near-infrared region, which makes them a limited contributor to photocurrent generation. In addition to these, chemical changes made to fullerene acceptors cause several things; the formation of isomers with different electronic properties and molecular structures, i.e., those that do not have the desired properties. This mixture of isomers increases the need for purification, causing both material waste and a decrease in device performance (Q. Wu et al., 2024). In addition, the high production costs of fullerene-based acceptors hinder their economic viability. Despite these limitations, Yan and colleagues stated that PCBM is a strong n-type semiconductor that can act as both

an electron acceptor and a carrier, and they also stated that this property has the potential to increase efficiency in organic solar cells (Yan & Saunders, 2014). For example, adding a PCBM layer to the P3HT: PCBM mixture increased the device's PCE to 4.24%. (Chi et al., 2014) representing a notable improvement over previous values. PCBM is a frequently used component in organic solar cells due to its good solubility and high electron acceptability. However, PCBM has low stability, high cost and poor visible absorption, which has led researchers to search for long-lasting substitutes. In contrast, non-fullerene acceptors allow more flexible and effective tuning of optoelectronic properties with different structural combinations thanks to their easily interchangeable molecular building blocks. To synthesize NFAs, specific molecular components are usually designed and combined, which makes it easier to control their final structures. Moreover, intramolecular charge transfer efficiency increases due to the expansion of π-conjugated systems, thus enhancing the absorption in the visible and near-infrared (NIR) regions, thus allowing light capture in a wide spectrum. This strong light absorption property, when used with compatible donor and acceptor materials in the active layer, can increase the optical current generated and the overall efficiency of the device. Since the charge transfer state is energetically closer to the singlet excited state in organic solar cells with non-fullerene acceptors, the energy loss due to radiative recombination is minimized and the electroluminescence efficiency is increased (Y. Xu et al., 2023).

In recent years, researchers have been focusing on various synthetic strategies for non-fullerene acceptors. These approaches can be listed as acceptor-donor-acceptor (A-D-A) type structures, fused ring acceptors such as ITIC, conjugated backbones without sp^3-hybridized carbon atoms, and simpler ring systems consisting of a single aromatic unit. The A-D-A design of ITIC combines a planar and broadly conjugated backbone with strong electron-withdrawing end groups, which has the advantage of increasing the spread of π-electrons, supporting efficient charge transfer and transport within the molecule. Hou and colleagues showed that adding chlorine to the ITIC molecule stabilized the energy levels better and additionally broadened the absorption range more than adding fluorine. They also observed that the position of

the halogens greatly changed the crystallinity of halogenated ITIC. They compared organic photovoltaic devices using two halogen substituents (F, Cl, Br) as nonfullerene acceptors and an electron donor as PBDB-T, and observed some surprising performance differences. The fluorine-containing form provided the highest short-circuit current density, while the bromine-containing form achieved the highest fill factor of 0.71. (Y. Zhang et al., 2018). In addition, K.S. Nithya and colleagues developed a non-fullerene acceptor organic solar cell containing PBDB-T:ITIC and achieved 15.68% power conversion efficiency under optimum conditions with this system (Nithya & Sudheer, 2020). Apart from ITIC, another important non-fullerene acceptor is Y6. Y6 receptors provide multiple effective pathways by forming three-dimensional complex structures, which facilitate charge transport, so researchers have placed special emphasis on optimizing mixtures using Y6 and its derivatives and understanding the reasons behind this high performance (L. Zhu et al., 2020). Furthermore, Li and his colleagues found that the PM6:Y6:ITIC-M ternary mixture formed an alloy-like structure with Y6, increasing the open-circuit voltage (Z. Li et al., 2021). In this thesis in the active layer blend, Y6 and ITIC were used as NFA.

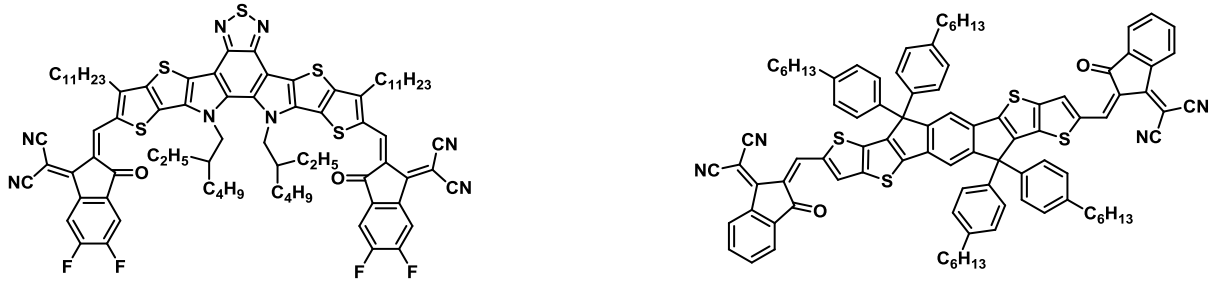


Figure 1.11. Structures of Y6 and ITIC

1.7.3 Polymeric Donor Unit

As mentioned before in organic solar cells, the active layer is typically made up of a donor and an acceptor. That is why having a high-performance polymer donor is an important factor in determining the power conversion efficiency of OSCs. To

accomplish this, polymer donors must be designed and synthesized with physical properties that are closely related to their acceptor counterparts (Luo et al., 2025). To ensure high efficiency, donor units should have the following specialties:

1) Ideally, a well-designed donor polymer should dissolve easily in commonly used organic solvents for solution processability (Gedefaw et al., 2016).
2) Air stability is essential for lifespan and long-lasting use (Gedefaw et al., 2016).
3) An appropriate band gap for efficient light harvesting. To match the solar spectrum and increase J_{SC}, a broad and strong absorption band in the visible and near-infrared regions is needed, which means a smaller E_g is ideal (Y. Li, 2012).
4) Low-lying highest occupied molecular orbital (HOMO) level to increase the V_{OC} of the OSC devices as well as to facilitate exciton dissociation at the donor/acceptor interface (Y. Li, 2012).
5) High hole mobility for the donor is good to boost the devices' FF and charge transport efficiency (to raise J_{SC}) (Y. Li, 2012).
6) Donors should have excellent film-forming capability with acceptor moiety (Gedefaw et al., 2016).
7) The interpenetrating network of the donor/acceptor mixture active layer must have optimal morphology and nanoscale phase separation, which has a major impact on the J_{SC}, V_{OC}, and FF of OSCs (Y. Li, 2012).

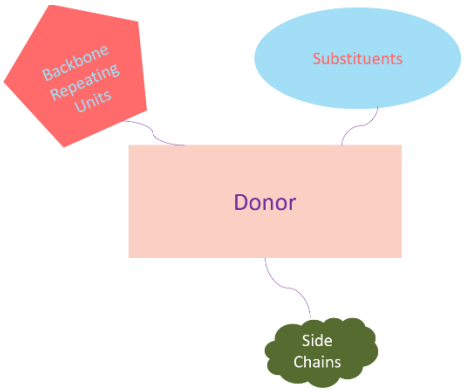


Figure 1.12. Main parts of donor

1.7.3.1 Benzodithiophene as a Polymeric Donor Unit

Researchers have long studied different conjugated building blocks to produce high-efficiency organic solar cells. One of the reasons for investigating different conjugated building blocks is to try to obtain high-performance polymer donors. The most important and promising of these donor polymers are dithieno[3′,2′:3,4;2″,3″:5,6]benzo-[1,2-c][1,2,5]thiadiazole, [1,2,3]triazolo[4,5-f]isoindole-5,7-(2H,6H)-dione, thiophene, benzo[1,2-c:4,5-c′]-dithiophene-4,8-dione (BDD), 6,7-difluoroquinoxaline and 1,3,4-thiadiazole (TDz). Among these donor polymers, benzo[1,2-b:4,5-b′]dithiophene (BDT) has attracted great attention due to its strong effect in improving both charge transport and morphology of the BHJ structure. In addition, due to the alkylation of its side chains, it is one of the most preferred polymers in the design of high-efficiency polymer donors (Huo et al., 2010). To maximize the performance of organic solar cells, halogen atoms are often incorporated into conjugated side chains. By lowering the HOMO energy level and strengthening the intermolecular interactions, the open circuit voltage can be increased and the BHJ morphology can be improved, which positively affects the overall efficiency of the device. Firstly, BDT derivatives are converted to organotin compounds and then undergo Stille cross-coupling reaction with different dibromo compounds to form target polymers; this method has enabled the development of many BDT-based conjugated polymers. The change in power conversion efficiencies in recent years has been highly correlated with BDT-based polymer donors. For example, An and co-workers achieved an efficiency of 11.21% by pairing the PBDB-T donor with the ITIC acceptor (W. Zhao et al., 2016). In 2019, Zou and his colleagues further increased the efficiency by 11.21%, achieving a PCE of 15.7%. To achieve this efficiency, they combined the donor PM6 that contains a BDT unit with the Y6 acceptor (Yuan et al., 2019). Finally, An and colleagues utilized PBDB-TF as a donor in a tandem device, achieving a 20.2% PCE with this method (An & Hou, 2022).

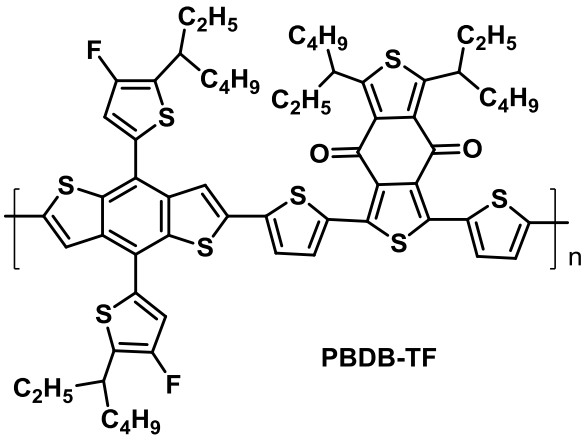


Figure 1.13. Structure of PBDB-TF polymer

1.7.3.2 Quinoxaline as a Polymeric Acceptor Unit

Among high-performance polymer donors, the alternating donor-acceptor stands out. It is possible to improve the optical and electronic properties of these conjugated polymers by controlling the intermolecular charge transfer (ICT) between donors and acceptors. The sp^2-sp^2 bonds in the polymer chain stabilize the resonance between the donor-acceptor and their charged counterparts, which narrows the band gap and makes the energy levels more suitable. Thanks to this method, researchers have designed thousands of different D-A type polymers to develop polymer solar cells with high energy conversion efficiency (M. Liu et al., 2017). In this thesis, quinoxaline is used as the acceptor unit of the polymeric donor part, and BDT is used as the donor unit. Quinoxaline attracts electrons because it is an electron-deficient molecule, and it provides this due to the two nitrogen atoms in the 1,4 positions. Palladium-catalyzed Suzuki or Stille polymerization methods are preferred in the synthesis of donor-acceptor type polymers (Suzuki & Miyaura, 1995). In this method, the donor containing diboronic or distannyl groups reacts with dihalogenated quinoxaline units via a chain growth mechanism to form the polymer (Johansson Seechurn et al., 2012). Quinoxaline has a strong quinoid structure, and if conjugated molecules with such a structure are added to the D-A type donor structure, the band gap of the polymers decreases. In order to improve the

photovoltaic properties of conjugated polymers, it is of great importance not only to control the band gap but also to adjust the energy levels such as HOMO and LUMO. Many modifications can be made on the quinoxaline molecule, and one of them is alkylation. Alkylated quinoxaline increases the solubility of conjugated polymers without causing steric hindrance. In addition, alkylated benzo units can be added to quinoxaline instead of alkyl chains, thus the interactions between the molecules are better controlled, and this can increase the carrier mobility with V_{OC} (Zhou et al., 2012). In 2021, Zhu and colleagues observed that the blended film obtained from PBQ6 donor containing quinoxaline and Y6 acceptor was more balanced in terms of hole and electron mobility, reduced charge carrier recombination, and its morphology was improved. As a result, the organic solar cell prepared with PBQ6:Y6 polymer showed a high fill factor of 77.91% and an impressive power conversion efficiency of 17.62%. (C. Zhu et al., 2021).

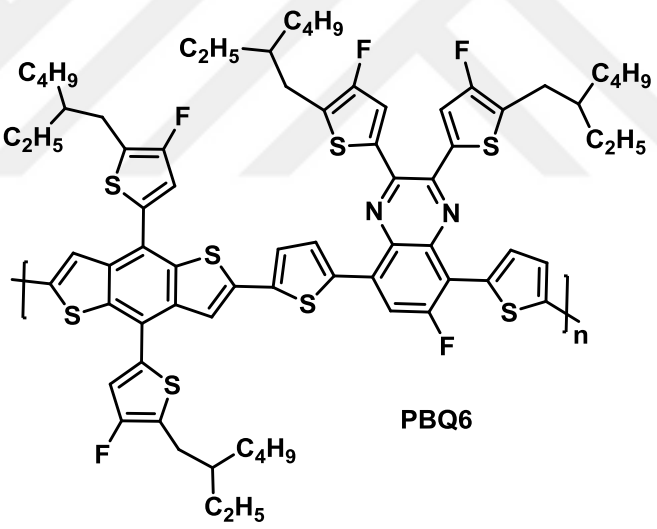


Figure 1.14. Structure of PBQ6 polymer

1.7.3.3 Thiophene π-Bridge

According to literature, insertion of different π-bridges such as thiophene, thienothiophene, dithiophene, selenophene, furan, and thiazole can greatly influence the photophysical and photovoltaic properties of electron-donating polymers, therefore, the yield of the organic solar cells. Thiophene and its derivatives act as

efficient π-conjugated bridges, linking the acceptor and donor units in a molecule. By doing so, they enhance charge transport within the donor-acceptor backbone and extend the conjugation of molecules, therefore improving their electronic properties (R. Wu et al., 2016). As stated, thiophene, oligothiophene derivatives, or fused thiophene have long conjugation bridges; therefore, they enhance the absorption coefficient by strengthening intramolecular charge transfer. This also broadens the absorption, shifting it toward the red and near-infrared regions (C. Zhu et al., 2021). Equally important, thiophene has a lower band gap and a more planar polymer backbone because they are less sterically hindered when it is homocoupled. Moreover, the high polarizability of the soft sulfur atoms in thiophene rings greatly enhances the capacity of thiophene derivatives to donate electrons and carry charges (Schroeder et al., 2014).

1.7.3.4 Thienothiophene and Thiophene Side Chain on BDT

Understanding the effects of side chains in the BDT core has gained attention due to their impact on the photovoltaic performance of organic solar cells (Taskaya Aslan et al., 2025). To investigate these effects, Kim and co-workers synthesized a new two-dimensional conjugated polymer, PSTTBDT-FTT, by adding a thieno[3,2-b]thiophene (TT) structure and an alkylthiophene group to the benzodithiophene (BDT) unit. In addition, they stated that the hole mobility could be increased by adding the thieno[3,2-b]thiophene molecule to the polymer chain because thieno[3,2-b]thiophene has a strong conjugation ability along with its rigid molecular structure. As a result, they thought that including this unit in the structure would create stronger π-π interactions between the polymer chains, which would allow for more efficient charge transport. In addition, the electron density was increased and the donor character was further strengthened by the addition of the alkylthio group to the thienothiophene unit. The researchers stated that the energy levels were adjusted and the morphological properties were improved. With these changes, it was noticed that the polymer absorbed light in a wider range, meaning that the

absorption spectrum was red-shifted. At the same time, the hole mobility increased significantly (0.053 $cm^2/V.s$), contributing to easier and more efficient transport of charges. Kim and his team increased the power conversion efficiency of the devices to 8.61% at the end of their study. They stated that this rate is quite good for this type of system (J. H. Kim et al., 2015). Moreover, Peng and his team investigated how adding thiophene side chains to the BDT core would increase the electron density of the donor material and how this would affect the photovoltaic performance of the device. As a result of the study, it was reported that the incorporation of thiophene side chains led to a lowering of the HOMO energy levels, which in turn contributed to higher open-circuit voltages. In addition, devices produced with modified copolymers called PBDT-OBT, PBDT-FBT showed power conversion efficiencies of 5.64% and 6.21%, respectively. These findings highlight the significant role of thiophene side chains in enhancing the photovoltaic performance of polymer solar cells (Q. Peng et al., 2011).

1.7.3.5 Effects of Benzene Side Chain in Quinoxaline

Benzene rings can provide advantages in terms of continuity of conjugation, as they provide more planar and rigid structures. This can broaden the absorption spectra (S. Xu et al., 2018). For example, Chen and colleagues studied the effects of modifications to quinoxaline-based structures, especially those with different side chains (including benzene-derived aromatic groups), on organic solar cells. In the article, four different QX derivatives were compared, one of which is a structure with a benzene-like side chain (ethylhexyl with aromatic effect) named QX-EH. As a result, a wider absorption spectrum was observed, and it was understood that benzene-like structures shifted the absorption to the red by increasing the conjugation length. In addition, the HOMO and LUMO levels became more compatible with commonly used donors such as PM6. It was also concluded that the surface free energy was high, which positively affected the film morphology and

stability. Equally important, it was stated that the hole mobility was higher, which would increase the FF and efficiency of the device (Chen et al., 2022).

1.7.3.6 Effects of Alkyl Chains

Alkyl chains are often introduced into conjugated polymers to enhance their solubility in organic solvents. Beyond this simple purpose, the polymer's overall molecular geometry can be shaped by its structural properties, including where they are attached, length, and whether they are linear or branched. These properties also affect how polymer chains interact with each other, which determines their alignment and stacking pattern in the solid state (C. Wang et al., 2023). For example, Yao and colleagues synthesized two different conjugated polymers with benzothiadiazole (BT). The difference between these polymers is that one contains linear alkyl chains (PBDT-T12BT) and the other contains branched alkyl chains (PBDT-TEhBT). Some of the results obtained in this study are as follows: the position, length, and structure of alkyl chains (straight or branched) significantly affect the molecular structure and intermolecular interactions of the polymer. For example, branched alkyl chains increased the adhesion of polymer chains to each other both in solution and in thin films, and also supported the formation of a more regular film by strengthening the crystal structure in blend films. Furthermore, Yao and his associates indicated that while alkyl chains do not directly influence the HOMO–LUMO band gap, they can impact charge transport by altering the π–π stacking distance. They also indicated that they will regulate hole mobility by managing the interactions among polymers. In this context, device performance was enhanced by employing various side chains in two polymers, PTB7 and PTB7-Th. The 2-ethylhexylthienyl group incorporated in PTB7-Th enhanced device efficiency by improving fill factor and short-circuit current density (J_{SC}). The thienyl (thiophene) group in PTB7-Th can be conjugated to the core structure, making the main chain more planar. A more planar structure improves π-π stacking, enabling carriers to migrate more between polymer chains. Electron mobility hence rises, resulting in higher J_{SC} and PCE. Another polymer,

which is called PBDB-T, offered high resolution and enhanced bulk heterojunction morphology due to its branched alkyl chains (H. Yao et al., 2016). Another important parameter is the length of the alkyl chain. Dai and his colleagues conducted a study on the effect of alkyl side chain length on the solubility, interchain packing, and charge transport properties of π-conjugated polymers. In this study, the polymer poly(thieno[3,4-c]pyrrole-4,6-dione-alt-3,4-difluorothiophene) named PTPD[2F]T was investigated using two different side chain lengths: one is 2-hexyldecyl (2HD) and the other is 2-decyltetradecyl (2DT). As a result, increasing the length of the alkyl side chains was found to enhance the solubility of the polymer. Specifically, the polymer bearing the longer 2DT side chain exhibited improved solubility compared to its 2HD counterpart. However, the shorter 2HD side chains contributed to greater backbone planarity, which enhanced π–π stacking interactions between polymer chains. In contrast, the extended alkyl chains of 2DT reduced the backbone planarity and introduced steric hindrance, leading to increased side-chain–backbone interactions and a more disordered, loosely packed morphology. Furthermore, shorter side chains were found to increase electron mobility. Polymers with 2HD side chains exhibited more effective charge transport properties; It was suggested that this is due to the higher interchain packing density and order. In conclusion, this study revealed that in order to obtain the best efficiency, the alkyl chain length should establish a balance between the solubility and electronic properties of the polymer. It was stated that shorter chains provide better interchain alignment and charge transport, but their solubility may be slightly lower. Although their solubility may be somewhat lower, shorter chains were said to offer better interchain alignment and charge transport. Although longer side chains increase the solubility of the polymer, they may negatively affect the charge transport ability because they can weaken the interchain interactions. Therefore, in order to obtain both good solubility and high electronic performance, the side chain length should be carefully adjusted according to the application and processing conditions to be used (Dai et al., 2024).

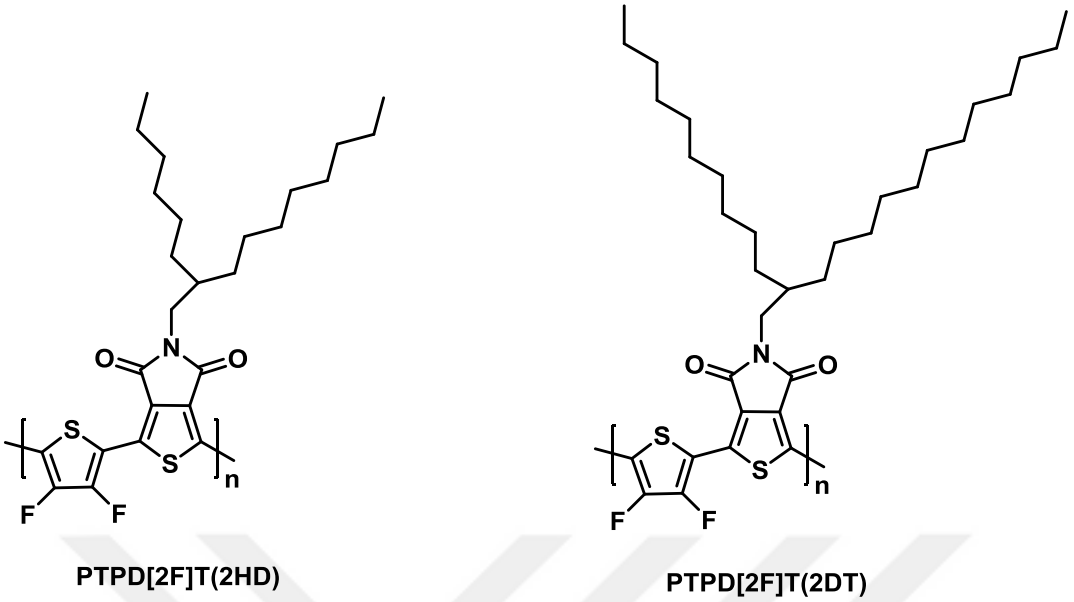


Figure 1.15. Structures of PTPD[2F]T(2HD) and PTPD[2F]T(2DT)

1.7.3.7 Effects of Halogen Substitution

Fluorine-containing organic molecules are known to have important properties such as reverse charge density distribution, resistance to degradation, and thermal and oxidative stability. The reason for these properties can be related to the general properties of the fluorine atom. For example;

1) It has a Pauling electronegativity of 4.0, which makes the fluorine atom the most electronegative element.

2) The smallest electron-withdrawing property belongs to fluorine, with a Van der Waals radius of r = 1.35 Å, so fluorine does not cause steric hindrance. In addition, fluorine atoms significantly affect intramolecular and intermolecular interactions with C-F···H, F···S, and C-F···pF interactions.

The insertion of fluorine will reduce the HOMO and LUMO in the conjugated backbone, as the fluorine atom possesses strong electron-withdrawing properties. Therefore, it causes an increase in V_{OC}. Liang and his colleagues demonstrated the electronic effects of fluorinated materials using benzodithiophene thieno[3,4-

b]thiophene copolymers. They discovered that substituting fluorine for the thieno[3,4-b]thiophene unit resulted in a lower HOMO and LUMO than its nonfluorinated counterparts, while the band gaps remained constant. In addition, they observed that the short-circuit current and fill factor increased significantly with careful selection of solvent and certain additives. They assumed that this was due to the optimized morphology by inserting fluorine atoms (Liang et al., 2009). Apart from this, for the first time, Zhou and his colleagues have made a fluorine substitution in a donor-acceptor type polymer. In this study, the polymer named PBnDT-DTffBT contains fluorinated benzothiadiazole (DTffBT) while the polymer named PBnDT-DTBT contains fluorinated benzothiadiazole (DTBT). In addition, the side chains and processing conditions of both polymers were kept the same, and only the effect of fluorine was examined. As a result of the study, it was observed that the fluorinated polymer exhibited a deeper HOMO level of –5.54 eV, compared to –5.40 eV for the non-fluorinated counterpart. In addition, the LUMO level of the fluorinated counterpart was -3.33 eV. while that of the non-fluorinated polymer was -3.13 eV. The fluorinated polymer demonstrated enhanced device performance, with a V_{OC} of 0.91 V, J_{SC} of 12.91 mA/cm^{-2}, FF of 61.2 and PCE of 7.2%. In contrast, the non-fluorinated polymer showed a V_{OC} of 0.87 V, J_{SC} of 10.03 mA/cm^{-2}, FF of 57.3, and PCE of 5.0%, respectively. As a result of this study, it was observed that fluorine optimized energy levels by reducing HOMO and LUMO levels, which meant higher open circuit voltage and more stable transport. In addition, it was observed that the fluorine polymer formed better π–π stacking in the solid state, which improved film morphology, and it was stated that it exhibited good performance even with high film thickness (~190 nm), meaning that the film morphology was stabilized by fluorine (Zhou et al., 2011).

Another important substitution is chlorine. One of the reasons for this is that chlorine is of great importance for the π–π stacking ability of substituted materials. Cl has a large atomic size. This is a matter of caution because large atomic size increases the overlap of π electrons and improves intermolecular packing and crystallinity, therefore improving charge transport. However, suppose Cl is inserted improperly

into the backbone or side chain. In that case, this will result in a more twisted π plane and greater steric hindrance, which will have adverse effects on the photovoltaic performance of the corresponding materials (H. Yao et al., 2020). Zhang and his colleagues have studied the effect of adding chlorine atoms to alkylphenyl side chains in donor-acceptor type conjugated polymers in detail at both structural and device performance and in this study, a reference polymer called Z1 that does not contain chlorine and a polymer called Z2 that contains chlorine in the meta-position of the alkylphenyl side chain were compared. As a result of this study, it was observed that when chlorine was substituted, the planarity and stacking of the polymer increased, leading to more regular crystallization of the polymer. In addition, it was determined that the HOMO-LUMO energy levels slightly decreased and contributed to V_{OC}. It was seen that the chlorinated polymer showed better phase separation and domain homogeneity, and balanced both hole and electron mobility. Since the recombination of the chlorinated polymer was less, FF and J_{SC} increased, and thus the PCE increased from 12.03% to 15.11% (M. Zhang et al., 2023). Consequently, fluorination and chlorination are two important factors to optimize the properties of organic photovoltaic materials. As mentioned before, fluorine lowers energy levels and increases crystallinity, but high levels of crystallinity may restrict flexibility. Although it offers a broad absorption spectrum and helps to lower energy levels, chlorine may cause steric hindrance, so reducing planarity and crystallinity. Consequently, the suitable halogenation technique should be chosen depending on the intended characteristics in the material design (Q. Zhao et al., 2020).

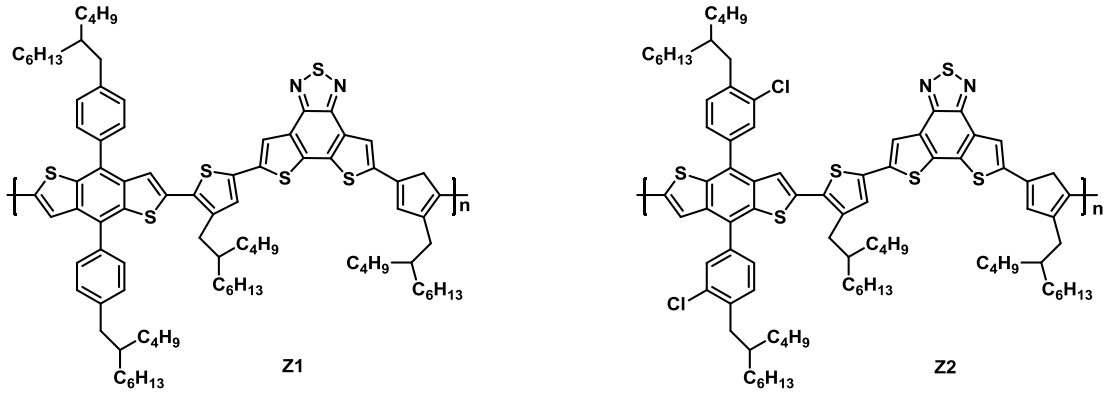


Figure 1.16. Structures of Z1 and Z2 polymers

1.8 Literature Research

In this thesis, a total of 6 polymers were synthesized. These polymers were used as donor polymeric materials in D-A type bulk heterojunction organic solar cells. Among the polymers examined in the literature, the **PBDTClT-TQxT** polymer synthesized by Lenaerts and colleagues exhibits the most structurally similar backbone to the **P2** polymer synthesized in this thesis. The only distinction lies in the alkyl side chain attached to the quinoxaline unit: while the **P2** polymer incorporates a n-octyl (-C_8H_{17}) chain, **PBDTClT-TQxT** features a n-hexyl (-C_6H_{13}) chain. This variation was expected to influence molecular packing and film morphology due to steric effects, thereby affecting the device performance. Upon reviewing the literature, several structural modifications of the quinoxaline and BDT cores such as different halogen substituents on the quinoxaline unit and varying side chains or π-bridges on the BDT corewere identified, many of which are closely related to the polymer structures synthesized in this thesis Although structurally related polymers have been reported in the literature, the polymers synthesized in this thesis are considered new due to distinct variations in the alkyl chains, π-bridges, and halogen substituents. These differences are expected to influence backbone planarity, molecular packing, and phase separation behavior, which can in turn affect the energy levels, charge transport, and overall photovoltaic performance. For comparative purposes, two previously reported polymers from the literature,

PBDTFQ-T and **PBDTFQ-TT**, synthesized by Gedefaw and his colleagues., were selected due to their structural resemblance to the polymers developed in this thesis. With these polymers, it is possible to observe how the nature of the π-bridgethiophene in **PBDTFQ-T** and thienothiophene in **PBDTFQ-TT** affects photovoltaic performance. While thienothiophene can enhance backbone planarity and extend π-conjugation, it may also introduce steric hindrance depending on the substitution pattern and surrounding groups. This can influence molecular packing and film morphology, leading to either improved or diminished charge transport and overall device efficiency. The fluorinated polymers **P0F**, **P1F**, and **P2F** from the literature are used to investigate the effect of fluorine substitution. Similarly, **PBCl-Qx** and **PBDTClT-TQxT** were employed to examine the impact of chlorine atoms on device performance. Finally, the polymers **P(BDT-Qx)** and **P(BDT-DTQx)** enable assessment of the effect of incorporating a thiophene π-bridge on the overall photovoltaic behavior. A summary of the optical properties of all these polymers is presented in the Table 1.1.

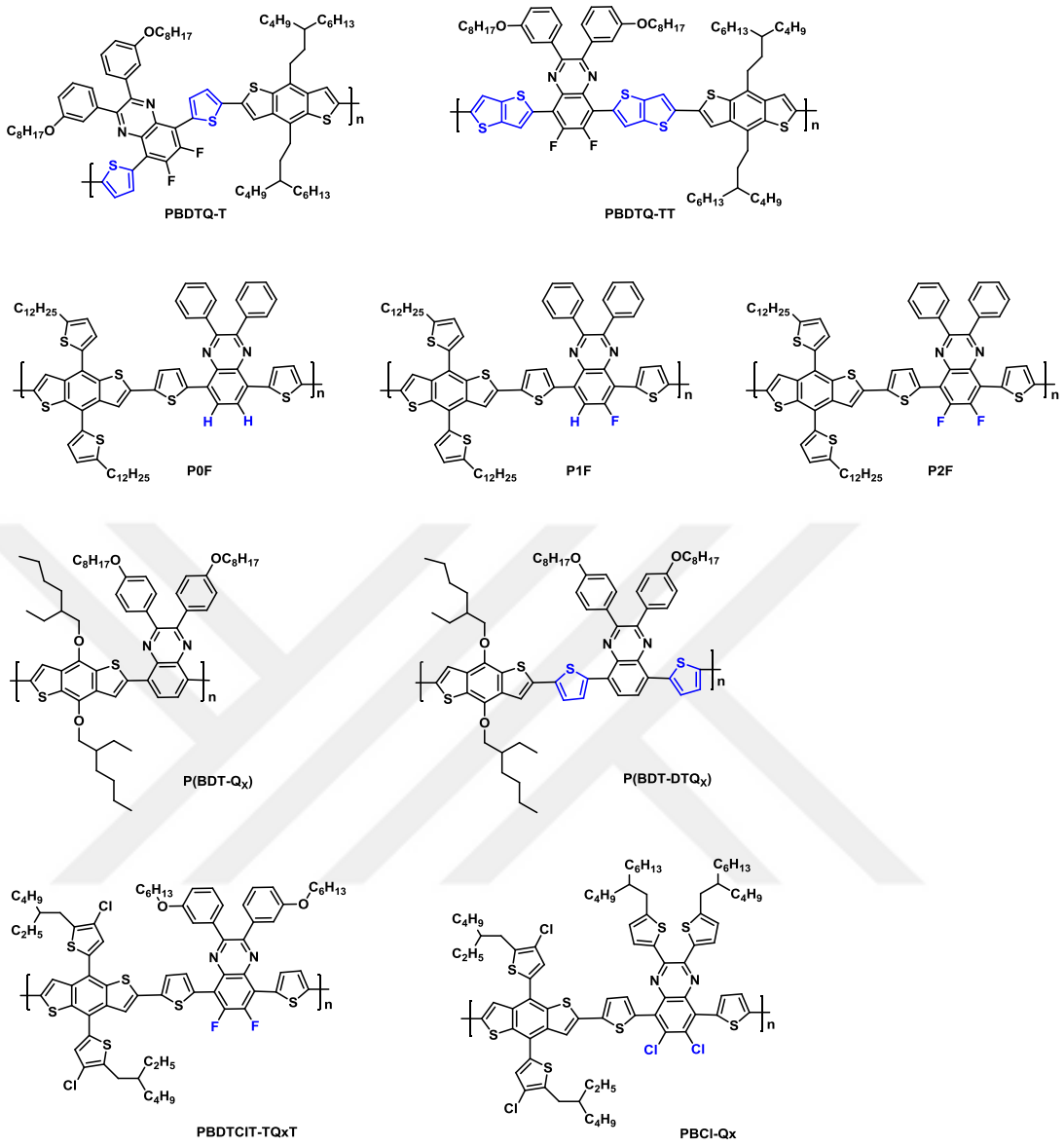


Figure 1.17. Structures of literature review polymers

Table 1.1 Photovoltaic properties of literature review polymers

Polymers Blend	Ratio D-A	J_{SC}(mA/cm^2)	V_{OC}(V)	FF(%)	PCE(%)	References
PBDTFQT: $PC_{61}PM$	1:1	9.18	0.84	67	5.30	(Gedefaw et al., 2014)
PBDTFQTT: $PC_{61}PM$	1:1	10.87	0.82	59	5.29	(Gedefaw et al., 2014)
P0F: $PC_{71}PM$	1:1.5	6.37	0.83	54	2.90	(H. Yao et al., 2016)
P1F: $PC_{71}PM$	1:1.5	6.52	0.87	55	3.10	(H. Yao et al., 2016)
P2F: $PC_{71}PM$	1:1.5	6.84	0.91	59	3.70	(H. Yao et al., 2016)
P(BDT-Qx): $PC_{71}PM$	1:5	5	0.77	50.30	1.90	(Fu et al., 2013)
P(BDT-DTQx): $PC_{71}PM$	1:5	6.30	0.65	55.20	2.30	(Fu et al., 2013)
PBDTClT-TQxT: ITIC	1:1	14.61	0.94	0.60	8.22	(Lenaerts et al., 2020)
PBCl-Qx: Y6	1:1	26.32	0.76	62.10	12.44	(Lee et al., 2022)

1.9 Aim of the Study

One of the most important ways to obtain narrow band gap polymers is to polymerize electron-deficient acceptor units with electron-rich donor units. The integration of donor and acceptor units along the polymer chain can enhance electron delocalization, which may lead to a reduction in the band gap. In this way, the absorption spectra of conjugated polymers can be improved. The primary objective

of this thesis study is to develop and characterize six novel, narrow band gap donor–acceptor type conjugated polymers designed for use as donor materials in the active layer of bulk heterojunction organic solar cells. In addition, the HOMO-LUMO level, band gap, film-making ability, solubility, and morphology of the polymers are analyzed, and these analyses aim to investigate the effect of halogen substitution and different side chains on polymer donor units. These polymers are built from BDT as a donor and quinoxaline as an acceptor unit, linked by thiophene π-bridges. Three different halogen-substituted acceptor units, monofluorinated, difluorinated, and dichlorinated, were coupled to two different donor units, thiophene and thienothiophene containing BDT, via the Stille cross-coupling reaction. According to literature, by incorporating electron-rich donor BDT and electron-deficient acceptor, which are quinoxaline units because of the electron-deficient two nitrogen atoms, into the polymer backbone, intramolecular charge transfer is expected to be enhanced, resulting in increased π-electron delocalization. In addition, since the thiophene π-bridge connecting donor and acceptor units increases planarity, it is also aimed to increase charge transfer. Thienothiophene and thiophene located in the BDT core also increase π-π interactions, thus synthesizing polymers with high J_{SC} and V_{OC} values. In addition, halogens on the quinoxaline core are expected to decrease HOMO and LUMO values and increase V_{OC}. Therefore, considering factors such as low HOMO-LUMO band gaps, high V_{OC}, and J_{SC} are important factors in terms of device efficiency. In this thesis, six polymers, namely **P1**, **P2**, **P3**, **P4**, **P5**, and **P6**, were synthesized within the scope of the TÜBİTAK project. Among the six polymers, **P1**, **P3**, and **P5** include a BDT unit with thienothiophene, while **P2**, **P4**, and **P6** contain a BDT unit modified with chlorine and thiophene. This structure was designed to explore how changes in the BDT side chain affect polymer properties, and also to study how different halogen atoms in the quinoxaline unit (F, 2F, and 2Cl) influence the overall behavior when combined with each BDT type. As a result, six distinct donor polymers were successfully synthesized, and their optical, electrical, and mechanical characteristics were thoroughly investigated. Furthermore, conventional organic solar cells were fabricated using these polymers

to explore their photovoltaic behavior and to optimize the device configuration in order to achieve the highest possible power conversion efficiency (PCE).

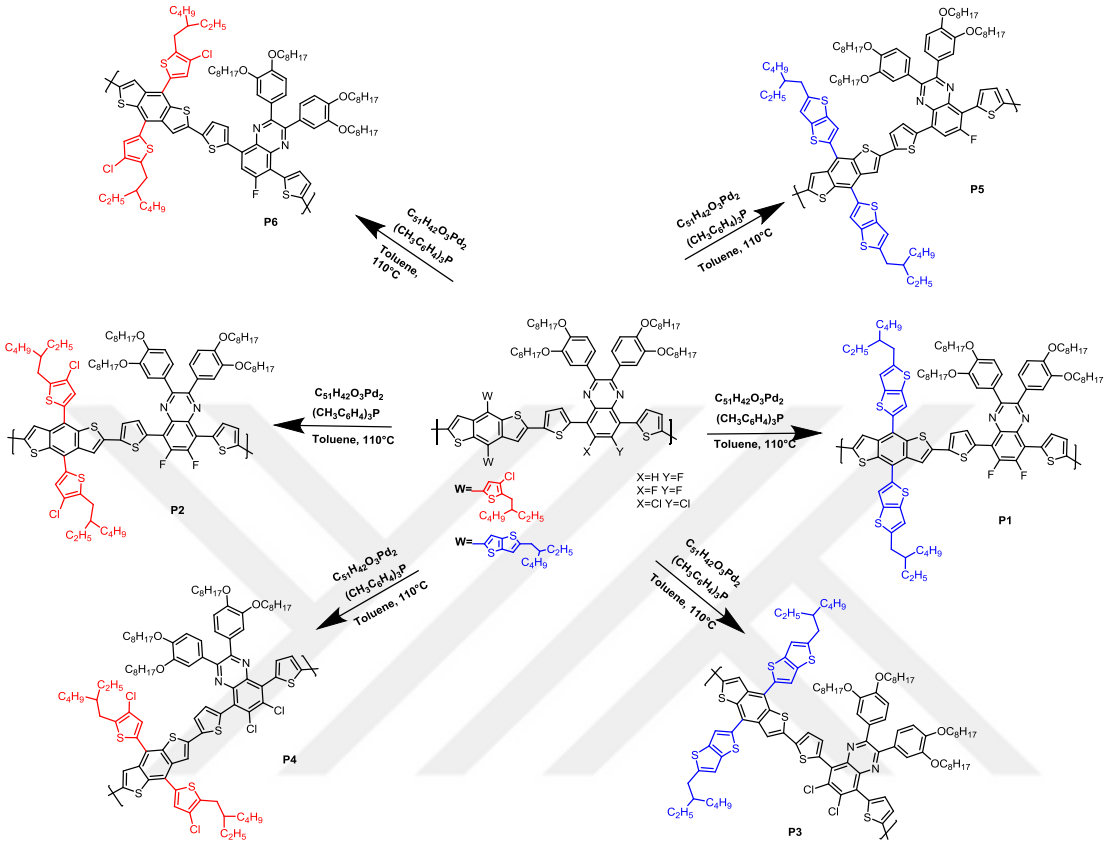


Figure 1.18. Structures of synthesized polymers fort his thesis study

CHAPTER 2

RESULTS AND DISCUSSION

2.1 Gel Permeation Chromatography

Gel permeation chromatography (GPC) is used for the analysis of polymers or oligomeric compounds. In this thesis, gel permeation chromatography is used for the mass analysis of polymers. GPC separates molecules in the mobile phase mostly according to their size, so molecular size and molecular mass are often directly proportional. When determining the weights of substances, columns are filled with polystyrene/divinylbenzene with very small pores. Since only small molecules can enter these pores, larger molecules are unable to enter and are therefore eluted. Small molecules, on the other hand, can enter the pores, allowing them to travel longer and exit later. Very large molecules exit at the same time, very small molecules exit together, and later. The molecules in between are separated by being sorted according to their sizes. As a result, GPC separates a molecule not according to its chemical properties but according to its molecular size (Wypych, 2024). In this thesis, chloroform was used as an eluent to determine the weights of polymers, and polystyrene was used as a standard. As a result, the number average molecular weight (M_n), weight average molecular weight (M_w), and PDI (polydispersity index) of six polymers were analyzed by GPC.

Table 2.1 Gel Permeation Chromatography results of six synthesized polymers

Polymer	M_n (Da)	M_w (Da)	PDI
P1	65117	166150	2.55
P2	41263	80218	1.94
P3	16731	36936	2.20
P4	37726	79780	2.11
P5	6391	13494	2.11
P6	105681	159900	1.51

The M_w and M_n values of polymers can be affected by many factors; these factors can be listed as calibration standards, solvent and temperature, and structural properties of polymers. Five of these polymers (**P1**, **P2**, **P3**, **P4**, **P6**) have M_w and M_n values that meet the polymer definition. The M_w and M_n values of the **P5** polymer with a mono-fluorinated structure are 6391 Da and 13494 Da, respectively. The M_w and M_n values of **P218**, the polymer with the closest structure to this molecule from the literature, were reported as 6520 and 13535 Da, respectively. As is evident from the structures, **P5** and **P217** have the same quinoxaline unit and are both mono-fluorinated, and the GPC results are very close to each other. One of the biggest reasons why the results come in this way may be due to the fact that the reactivity of a monofluorinated molecule is lower than a difluorinated or dichlorinated molecule. When looking at the article, the only difference between the **P219** molecule with the same BDT and quinoxaline unit and **P218** is that it is difluorinated, and the M_w and M_n values are higher than **P218**, proving that the fluorine substitution naturally affects the reactivity and the M_w and M_n values clearly (H. Yao et al., 2016).

2.2 Optical Studies

The optical characterization of the prepared polymers was determined by UV-vis spectroscopy. The characterization with thin films was performed by coating the

ITO-coated glass with a 0.5 mg/ml polymer/chloroform solution using a spray coating method. The optical band gap of the synthesized polymers was calculated according to the thin film λ_{onset} values. This is because the polymers were coated as thin films on the active layer.

Table 2.2 Optical properties of six synthesized polymers

Polymers	**λ_{max} (nm) Solution**	**λ_{max} (nm) Thin Film**	**λ_{onset} (nm) Thin Film**	**E_g^{op} (eV)**
P1	360	381	709	1.75
P2	536	596	687	1.81
P3	356	428	633	1.96
P4	410	440	624	1.98
P5	371	577	708	1.74
P6	554	598	720	1.72

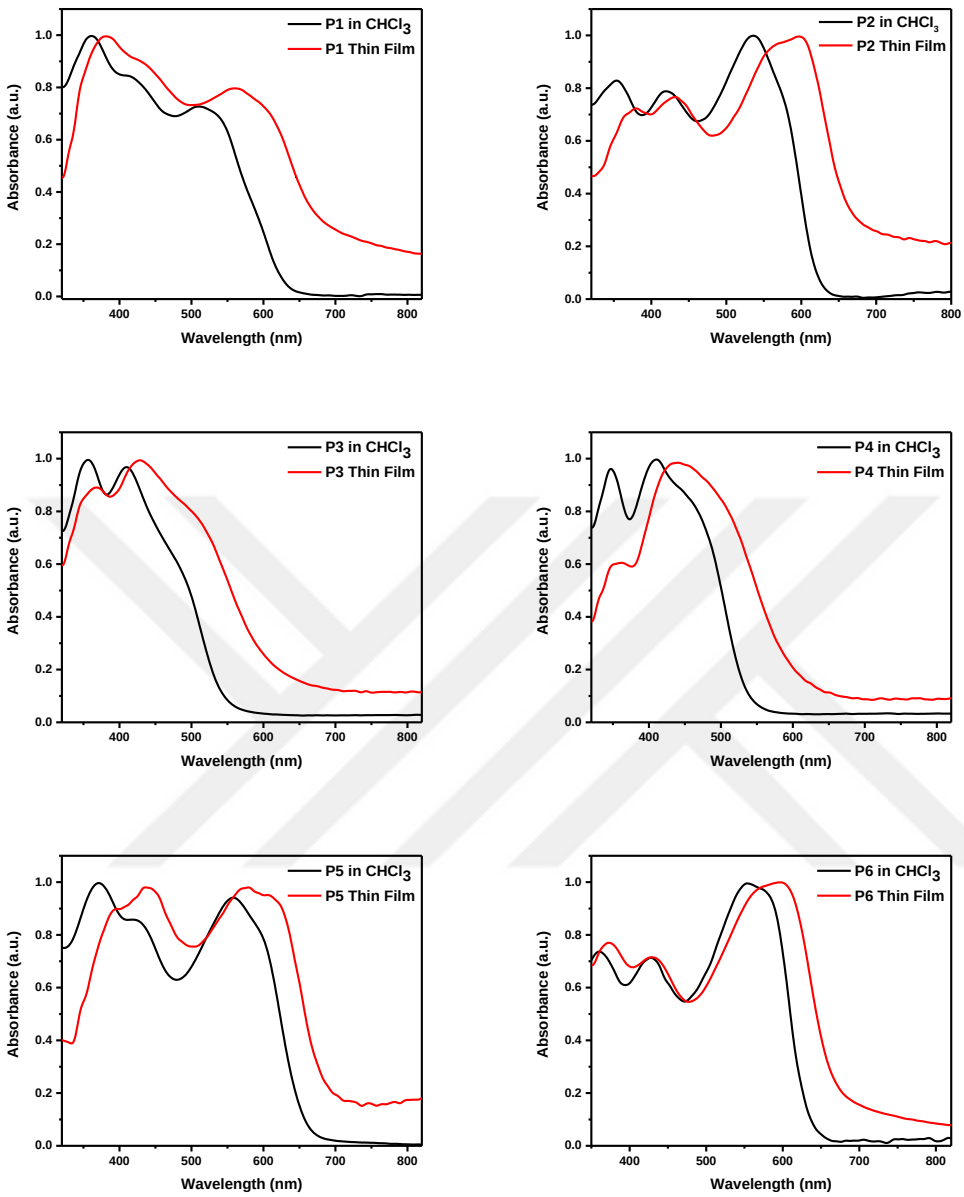


Figure 2.1. Normalized absorption spectra of polymers in solution and thin film

In all UV-vis spectra, the band between 300-500 nm corresponds to π-π* transitions, while the band between 500-800 nm corresponds to intermolecular charge transfer. The optical band gaps of monofluorinated, difluorinated, and dichlorinated quinoxaline-based polymers show an increasing trend in direct proportion to the

studies of Yang et al (P. Yang et al., 2014). The reason for such a trend is that the electron-withdrawing character is systematically increasing.

In the absorption spectra of the **P1** polymer in solution, the π-π* band is wider than the ICT band. This indicates that the molecule interacts with itself, but there is little interaction between molecules. In the thin film spectrum, the π-π* region is a little more spread out, which indicates that conjugation has increased. There is a clear red shift, meaning that the π-π stacking between them has increased. In the thin film spectrum, the π-π* region is slightly more spread out, indicating increased conjugation (Klauk, 2006). The apparent red shift and the increasing bandwidth indicate increased π-π stacking between them and thus increased aggregation and charge transfer. As a result, this width and shift indicate that the molecules in the thin film are more regular and closer together, and the optical properties change. In **P2** polymer, there are distinct π-π* transitions in solution, and there is a redshift in the ICT band in the thin film, and it is wider than π-π*. There is a strong π-π stacking and extended conjugation between molecules. The reason why **P2** polymer has a stronger ICT than **P1** polymer and the redshift is higher is due to the effect of the Cl atom in the donor core of **P2** polymer. Since Cl is an electron-withdrawing group, it facilitated the electron flow together with the quinoxaline core (Helgesen et al., 2010).

The most similar form of **P1** polymer in the literature is the **P2F** polymer. The main differences between these two polymers are the alkyl chains attached to the quinoxaline unit of **P1** polymer and the thienothiophene substitution on **P1** in the BDT core, while there is a thiophene substitution on **P2F**. The E_g value of **P2F** polymer is 1.81 eV, while the Eg value of **P1** polymer is 1.75 eV. Although both polymers have two fluorine atom substitutions on the quinoxaline unit, the reason why the E_g values are different from each other may be due to the different thiophene and thienothiophene groups on the BDT core and the different side chains. **P1** polymer contains an alkoxy side chain, which can cause the HOMO level to increase and decrease the E_g value, and since thienothiophene has a high conjugation capacity, it provides the same effect (Lu et al., 2015). However, the ICT band of the **P2F**

polymer is wider than that of the **P1** polymer, which is due to the slightly more asymmetric structure of the **P2F** polymer due to the thiophene substitution. Wang and his colleagues stated that the ICT intensity increases as the asymmetry increase (D. Wang et al., 2014).

The most similar form of **P2** polymer in the literature is **PBDTClT-TQxT** polymer, and the only difference is the alkyl chain length on the quinoxaline unit. While **PBDTClT-TQxT** has a shorter alkyl chain, **P2** polymer has a longer alkyl chain. This structural difference may affect the optical properties of the two polymers. When the spectra of the two polymers are examined, it is noticed that there are minor differences, for example, the ICT band observed in the film form in **PBDTClT-TQxT** polymer shows a more pronounced red shift and broadening compared to **P2** polymer. This shows that **PBDTClT-TQxT** has stronger intermolecular interactions and more effective conjugation in the film form. The reason for this is that **PBDTClT-TQxT** has stronger intermolecular interactions and more effective conjugation due to its shorter alkyl chain, which is reflected as a more pronounced red shift and band broadening in the UV-Vis spectrum (Z. Li et al., 2014).

Table 2.3 Optical properties of literature review polymer and synthesized polymer P2

Polymers	**λ_{max} (nm) Solution**	**λ_{max} (nm) Thin Film**	**λ_{onset} (nm) Thin Film**	**E_g^{op} (eV)**
PBDTClT-TQxT	585	630	700	1.77
P2	536	596	687	1.81

P3 and **P4** polymers have the same quinoxaline unit but different BDT side chains. **P3** polymer is slightly broader in thin film form compared to solution. There is a visible red shift, indicating that π-π stacking and aggregation have occurred. In **P4**, the red shift is less pronounced, indicating that the structure may be more bent, more

sterically hindered, and has more limited planarity because there is an additional chlorine substituent on **P4** that may cause steric hindrance compared to **P3**. The E_g values of these two polymers are 1.96 and 1.98, respectively, and a lower E_g in the film form is generally indicative of stronger stacking and planarity. In this case, **P3** has better planarity and more efficient conjugation than **P4**. In addition, there is a more pronounced shoulder in the spectrum of **P3** compared to **P4**. This shoulder is usually formed as a result of π-π stacking or intramolecular interactions. Finally, the only condition that has these properties is that the PDI value of **P3** (2.20) is higher than the PDI value of **P4** (2.11), but although the lower PDI value supports the formation of a more homogeneous film, stacking is always dependent on side chain barriers, that is, even if the disorder in the film of **P3** increases, stacking is more efficient in some regions than **P4** (Xie et al., 2021). The polymer most similar to **P4** in the literature is the **PBCl-Qx** polymer. The BDT units are the same in both polymers, the difference is that the **P4** polymer contains benzene and alkoxy sidechains in the quinoxaline unit, while the **PBCl-Qx** polymer contains a thiophene sidechain in the quinoxaline unit. Differences in the side chains of **P4** and **PBCl-Qx** polymers may affect the planarity and π-π stacking interactions of the polymers. In addition, the thiophene groups attached to the quinoxaline unit provided **PBCl-Qx** with a more red-shifted (longer wavelength) ICT band in the UV spectrum and a narrower E_g (1.77) value. Benzene groups in **P4** may not have increased this conjugation as much as thiophene. Because benzene is a more stable aromatic system, it does not support the formation of ICT much, but the structure with thiophene provides more delocalized, low-energy transitions, i.e., absorption occurs at longer wavelengths (Würthner et al., 2016).

P5 and **P6** polymers contain the same quinoxaline unit and different BDT side chains. Both spectra have a red shift, which means increased π-π stacking. However, there is a greater red shift in **P6** compared to **P5**. One of the reasons for this may be that polar groups, such as chlorine atoms in the BDT chain, can affect the intermolecular order and provide more effective conjugation. In addition, **P6** has a lower E_g value and a larger M_n value than **P5**. These results are important evidence

that **P6** absorbs at longer wavelengths and increases aggregation. In addition, there are more peaks in the UV spectrum of **P5** compared to **P6**. This is because the side chains of **P5** are more flexible and symmetric, causing weaker interactions between chains in solution. Thus, molecules behave more isolated and more independently, and each electronic transition can be observed more clearly (Z. Xu et al., 2022).

2.3 Electrochemical Studies

Electrochemical studies of polymers were performed using Differential Pulse Voltammetry (DPV) in 0.1 M $TBAPF_6$/ACN (tetra-butylammonium hexafluorophosphate/acetonitrile). $TBAPF_6$ was used as a supporting electrolyte. $TBAPF_6$ exhibits high ionic conductivity in solvents such as ACN. Especially in ACN-DMSO mixtures, the conductivity of $TBAPF_6$ was found to be higher compared to $LiPF_6$. This reduces the resistance losses in electrochemical cells and provides clearer voltammograms (Mozhzhukhina et al., 2015). Thin films were prepared by spray coating with 0.5 mg/mL polymer/chloroform solution. The reason for this study to be done with DPV is that DPV takes more sensitive measurements. DPV generally uses alternating voltage waves instead of constant voltage sweeps. This involves stepping back after a short interval after a voltage step. This minimizes the background current, especially from the electrode surface, and makes the signal much clearer (Venton & Discenza, 2020).

To calculate the HOMO and LUMO and E_g^{el} ;

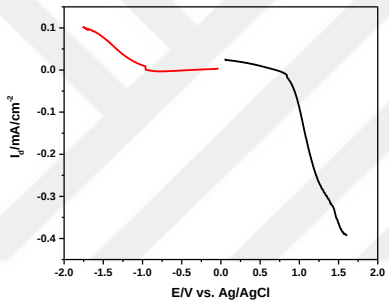
HOMO = $-(4.75+E_{ox}^{onset})$

LUMO = $-(4.75+E_{red}^{onset})$

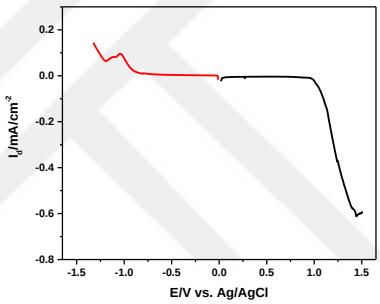
$\mathbf{E_g^{el}}$ = HOMO-LUMO

Table 2.4 Electrochemical properties of six synthesized polymers

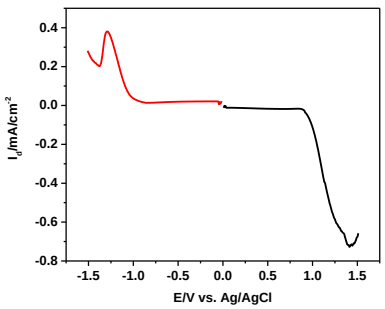
Polymers	E_{ox} onset (V)	E_{red} onset (V)	HOMO (eV)	LUMO (eV)	Eg^{el} (V)
P1	0.873	-0.890	-5.623	-3.860	-1.763
P2	1.032	-0.875	-5.782	-3.875	-1.907
P3	0.968	-0.875	-5.718	-3.875	-1.843
P4	1.514	-0.906	-6.264	-3.844	-2.420
P5	0.920	-0.908	-5.670	-3.842	-1.828
P6	0.940	-0.936	-5.690	-3.814	-1.876



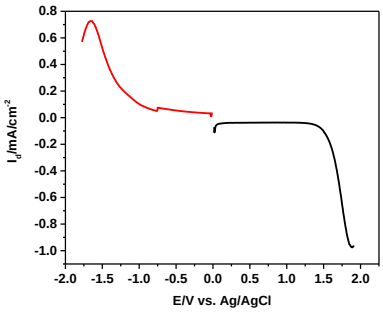
P1



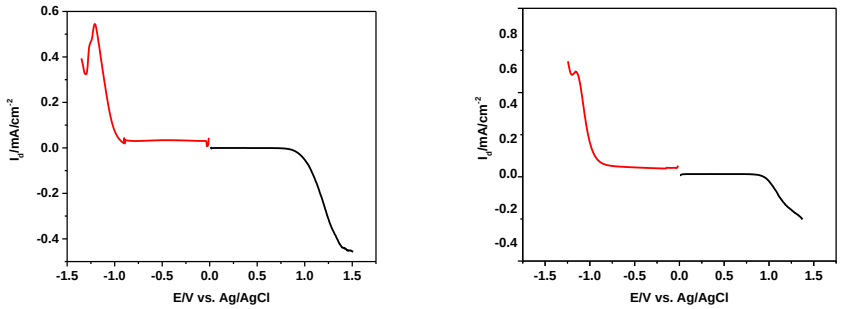
P2



P3



P4



P5 **P6**

Figure 2.2. Differential pulse voltammogram of the polymers in 0.1 M $TBAPF_6$/ACN

The electronic band gaps and optical band gaps of the 6 synthesized polymers are consistent with each other. In addition, the electronic band gaps are higher than the optical band gaps. The difference between these two band gaps is that free ions (i.e. charge carriers) are formed instead of neutral excitons in electrochemical measurements. This requires a higher energy, because in electrochemical redox processes, electron/hole pairs are separated and become real charge carriers. In contrast, in optical excitation, the electron and hole remain bound in the exciton state; therefore, the energy requirement is lower (Baran et al., 2010).

P1, **P3**, and **P5** are three polymers with different halogens on the quinoxaline core, having the same BDT structure. **P1** has a difluorinated **P3**, a dichlorinated **P5**, and a monofluorinated quinoxaline core. Looking at the electrochemical trend, we see that polymer **P3** has the lowest HOMO level while polymer **P1** has the highest HOMO level. This is attributed to the greater electron density capacity of the chlorine atom even though fluorine is a more electronegative atom than chlorine (Andrea et al., 2022). There is no visible change in the LUMO level of the polymers, but there are small differences. The lowest LUMO level was observed in the polymer **P3**, while the highest was observed in the polymer **P1**. Chlorine is more effective than fluorine in reducing the LUMO level, but its effect on the LUMO is not as great as its effect on the HOMO (Hasegawa et al., 2019).

P2, **P4**, and **P6** polymers have the same BDT core but different halogen groups on the quinoxaline unit. **P2** has difluorinated, **P4** has dichlorinated, and **P6** has monofluorinated quinoxaline structures. **P4** has the lowest HOMO level among these three polymers, as mentioned before, chlorine is more effective than fluorine in lowering the HOMO level, and this is consistent with the literature. In addition, the steric hindrance tendency of chlorine atoms plays an important role in the higher band gap of the dichlorinated polymer **P4**. Chlorine atoms have bigger steric hindrance than fluorine atoms, which disrupts planarity and reduces conjugation in the polymer backbone. These effects can lead to further separation of the HOMO and LUMO energy levels, thus widening the band gap (Y. Zhang et al., 2015). In addition, the monofluorinated **P6** polymer has a narrower band gap than the difluorinated **P2** polymer, and the HOMO level is lower than **P6**. While **P2** has a symmetric structure, **P6** has an asymmetric structure. Therefore, **P6** brings less steric hindrance to the π-conjugation plane, which results in a more planar structure and stronger conjugation, resulting in higher HOMO and lower E_g values (Leclerc et al., 2016).

P1, **P3**, and **P5** contain thienothiophene in the BDT unit, while **P2**, **P4**, and **P6** contain chlorine-substituted thiophene in the BDT core. The band gaps of **P2**, **P4**, and **P6** polymers containing chlorine-substituted thiophene are wider than those of **P1**, **P3**, and **P5** polymers containing thienothiophene. This is because the chlorine substitution in the BDT unit reduces the donating ability in the BDT core due to its electron-withdrawing nature (Lenaerts et al., 2020). Another reason is that the planarity of the BDT unit containing thienothiophene is better than the BDT unit containing chlorine-substituted thiophene. Thieno[3,2-b]thiophene is a condensed aromatic structure. This structure provides high planarity in the backbone of the molecule and allows more efficient delocalization of π-electrons. This affects the energy levels of the HOMO and LUMO orbitals, leading to a narrower band gap. For example, polymers containing thieno[3,2-b]thiophene exhibit lower E_g values than their thiophene-containing analogues (Y. Li et al., 2013).

The steric hindrances of chlorine-containing benzodithiophene derivatives reduce the planarity of the polymer backbone, disrupting π-conjugation, which widens the band gap. This effect occurs especially due to the large van der Waals radius (~1.76 Å) of the chlorine atoms and causes twists in the molecular structure. Also, when chlorine atoms are added to the polymer backbone, they cause an increase in dihedral angles, especially in the bonding regions between the BDT core and the π-bridge units. This increase reduces molecular planarity and limits π-electron delocalization. As a result, the difference between the HOMO and LUMO energy levels increases, i.e. the band gap widens (Chao et al., 2021).

2.4 Photovoltaic Characterizations

The photovoltaic characterizations in this thesis were made by optimizing **P1** polymer. Other polymers were optimized according to the optimization results of **P1** polymer. The red-marked part in the tables shows the best performance of the devices.

2.4.1 P1-Based Device

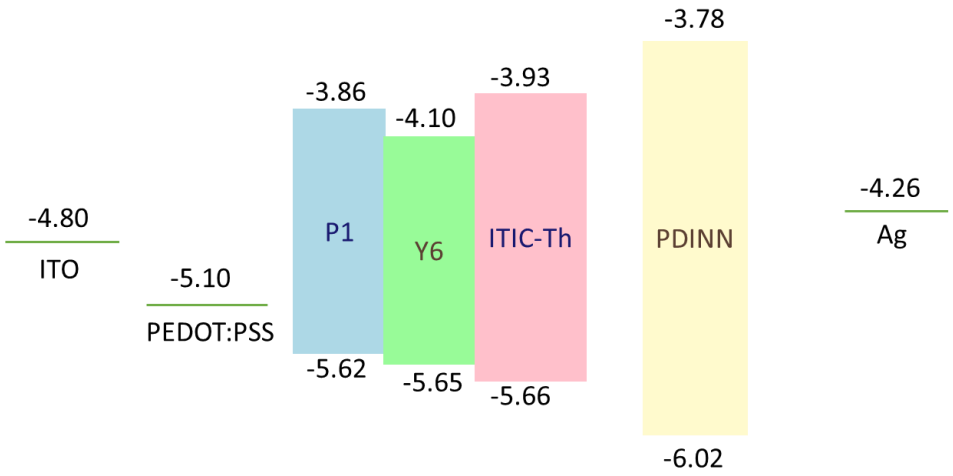


Figure 2.3. Energy level diagram of P1-based device

Table 2.5 Device performance of P1-based device

Polymer Blend	Solvent	D:A Ratio	Coating Rate	Additive	Ag Thickness (nm)	PCE (%)	FF (%)	V_{oc} (V)	J_{sc} (mA.cm^{-2})
P1:Y6	$CHCl_3$	1:1.2	3000	-	100 nm	4.43	37.87	0.80	14.63
P1:Y6	$CHCl_3$	1:1.2	2500	-	100 nm	2.93	34.19	0.74	11.59
P1:Y6	$CHCl_3$	1:1.2	3000	0.6% CN	100 nm	5.99	41.53	0.80	18.04
P1:Y6	$CHCl_3$	1:1.2	3000	1%DIO	100 nm	4.34	43.23	0.68	14.77
P1:Y6	$CHCl_3$	1:1.2	2500	1%DIO	100 nm	5.54	41.32	0.70	19.16
P1:ITIC-Th	$CHCl_3$	1:1.2	3000	0.6% CN	100 nm	1.33	29.05	0.99	4.61
P1:ITIC-Th	$CHCl_3$	1:1.2	2500	0.6% CN	100 nm	1.34	28.61	0.98	4.78
P1:ITIC-Th	$CHCl_3$	1:1.2	3000	1% DIO	100 nm	1.15	45.19	0.79	3.23

In this thesis study, **P1** polymer was used as a donor; Y6 with wide absorption range and ITIC-Th which can provide high V_{OC} were compared as acceptors. In addition, the effects of parameters such as additive usage (0.6% CN and 1% DIO) and coating rate on device efficiency were systematically investigated. Y6 is a non-fullerene acceptor with an absorption spectrum extending up to 900 nm and high electron mobility. P1:Y6 systems generally provide high J_{SC} and therefore high power conversion efficiency (PCE). In the device without additive and coated at 3000 rpm, J_{SC} value was obtained as 14.63 mA/cm^{-2}, the FF value as 37.87% and PCE value as 4.43%. These values indicate that phase separation in the film without additives is not optimized enough. Addition of 0.6% CN as an additive improved phase separation and donor-acceptor structure, increased charge generation and transport, and significantly increased device performance (Imran et al., 2017). In the device produced under these conditions, J_{SC} increased to 18.04 mA/cm^{-2}, FF was measured as 41.53%, and PCE reached the highest value of 5.99%. When the same device was produced with a lower coating rate (2500 rpm), carrier transport weakened due to the increase in film thickness, and Jsc decreased to 11.59 mA/cm^{-2}(Yenel, 2022). In

contrast, 1% DIO additive caused different effects. FF reached the highest level with 43.23% in the DIO doped device produced at a 3000 rpm coating rate, indicating the formation of interpenetrating donor-acceptor networks (L. Peng, 2018). However, the V_{OC} value decreased to 0.68 V. This decrease can be explained by the excessive separation of phases in the film morphology due to the slow evaporation structure of DIO and the increase in recombination losses at the interface. When the same doped and formulation were applied at a rate of 2500 rpm, a thicker film was obtained, light absorption increased and J_{SC} increased to 19.16 mA/cm^{-2}. In this case, PCE remained at a high value of 5.54%. However, in this device, V_{OC} remained low (0.70 V) due to 1% DIO. As a result, although higher FF and J_{SC} values were obtained with DIO doped, a balanced performance as much as CN doped was not achieved due to its negative effects on V_{OC} (W. Kim et al., 2015). ITIC-Th has a higher V_{OC} generation potential compared to Y6 due to its higher LUMO level (approximately –3.93 eV). Therefore, V_{OC} values in P1:ITIC-Th devices obtained in this study were in the range of 0.98–0.99 V and were superior to Y6-based devices (Lin et al., 2016). However, despite this, J_{SC} values are quite low (3.23–4.78 mA/cm^{-2}). The first reason for this decrease may be that the absorption spectrum of ITIC-Th is limited to 700–800 nm, and the second reason may be the low charge carrier mobility (F. Zhao et al., 2017). Especially in devices produced with 0.6% CN, FF values remained at the levels of 28–29%, and device efficiencies were limited to 1.33–1.34%. In the P1:ITIC-Th device using 1% DIO, FF reached the highest value of 45.19% among all devices; this shows that the phase separation regulating effect of DIO is more pronounced in the ITIC-Th system. However, in this device, J_{SC} remained only at 3.23 mA/cm^{-2} and PCE was as low as 1.15%. Although the improvement of charge transport paths by DIO increased FF, limited absorption and low charge generation restricted J_{SC}, which limited the overall efficiency.

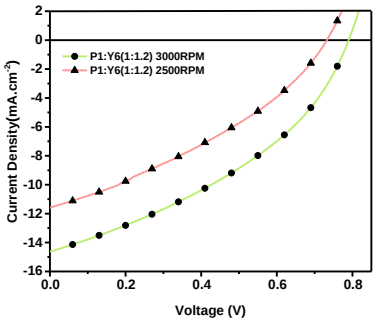


Figure 2.4. J-V characteristics of P1:Y6 with 2500 and 3000 rpm coating rates

a) b)

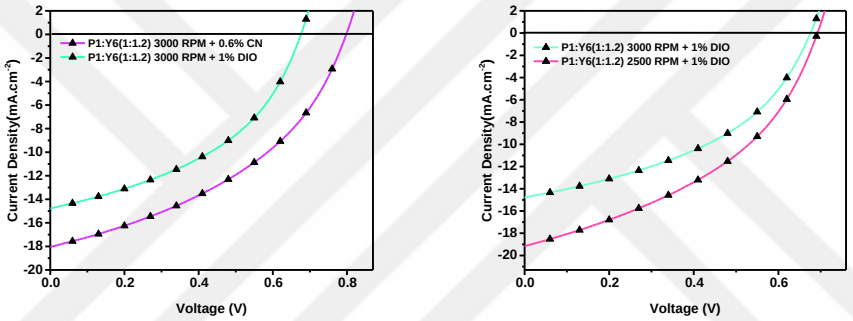


Figure 2.5. J-V characteristics of a) P1:Y6 with 0.6% CN and 1% DIO and b) P1:Y6 with 1%DIO with 2500 and 300 rpm

a) b)

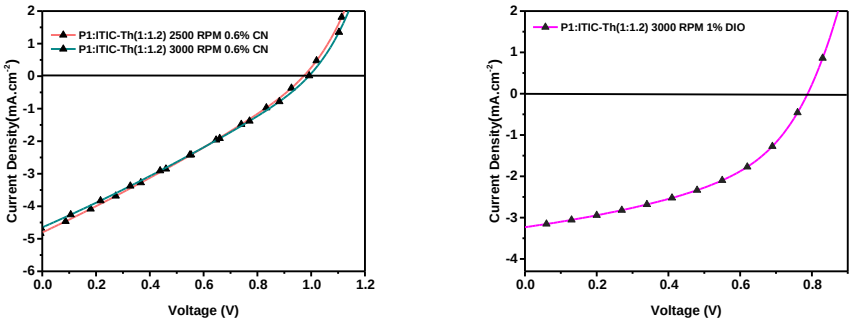


Figure 2.6. J-V characteristics of a) P1:ITIC-Th with 0.6% CN and b) P1:ITIC-Th with 1% DIO

2.4.2 P2-Based Device

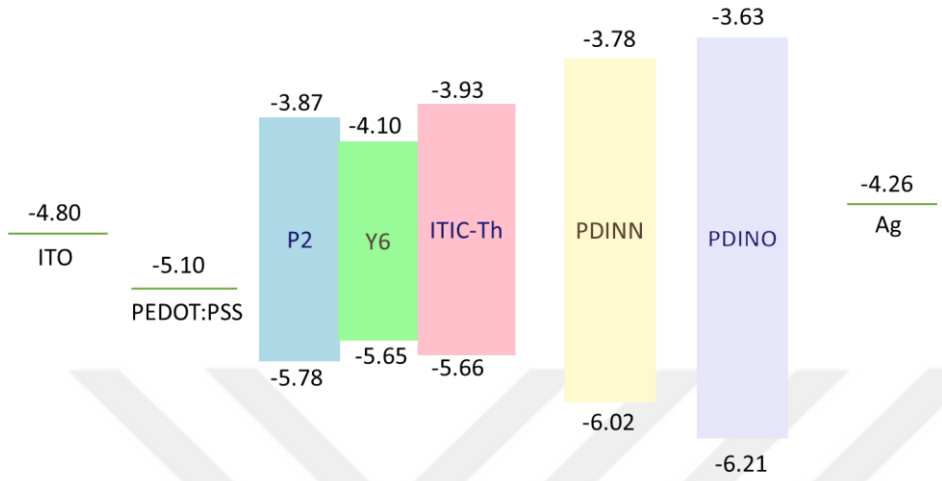


Figure 2.7. Energy level diagram of P2-based device

Table 2.6 Device performance of P2-based device

Polymer Blend	Solvent	D:A Ratio	Coating Rate	Ag Thickness (nm)	PCE (%)	FF (%)	V_{oc} (V)	J_{sc} (mA.cm^{-2})	Cathode Interlayer
P2:Y6	$CHCl_3$	1:1.2	2500	100	4.72	41.49	0.85	13.32	PDINN
P2:Y6	$CHCl_3$	1:1.2	3000	100	5.71	39.54	0.76	18.97	PDINN
P2:Y6	$CHCl_3$	1:1.2	3000	100	8.16	50.33	0.87	18.60	PDINO

The photovoltaic performances of the devices prepared using different spin coating rates and cathode interlayers (PDINN and PDINO) in systems where **P2** donor polymer (HOMO: –5.78 eV, LUMO: –3.87 eV) and Y6 acceptor were blended at a ratio of 1:1.2 and without additives were compared. The deep HOMO level of the donor increases the potential to obtain high V_{OC} in particular, and is also decisive in terms of charge transport and energy level alignment (X. Liu et al., 2025). In the

device produced using PDINN and at a coating rate of 2500 rpm, light absorption increased due to the increase in film thickness, but carrier transport was limited. Therefore, the J_{SC} remained at 13.32 mA/cm^{-2}, and FF was measured as 41.49%. Despite this, the V_{OC} value was maintained at a relatively high level of 0.85 V. This is due to the sufficient energy difference between the deep HOMO level of **P2** and the LUMO level of Y6 (about –4.10 eV) (W. Zhao et al., 2017). When the coating rate was increased to 3000 rpm, the film thickness decreased and charge transport became more efficient. As a result, the J_{SC} value increased to 18.97 mA/cm^{-2}. However, the V_{OC} value decreased to 0.76 V in this device. This decrease may be a result of morphological deterioration that may occur in thinner films or increased charge recombination at the interface (Wilken et al., 2021).

The most remarkable results were obtained in the device where PDINO interlayer was used instead of PDINN and again coated at 3000 rpm. In this device, J_{SC} remained at 18.60 mA/cm^{-2}, FF value increased to 50.33% and V_{OC} was measured as 0.87 V. With the combination of all these values, PCE reached 8.16%. PDINO offers more effective energy level alignment with the cathode due to its lower work function, which contributes to both increasing V_{OC} and improving electron transport paths (Moustafa et al., 2022). In addition, it is thought that charges are transported more symmetrically due to the more favorable surface energy and interfacial interactions of PDINO (J. Yao et al., 2020). These results clearly show that not only the active layer conditions but also the cathode interlayers are decisive on OPV device performance.

a) b)

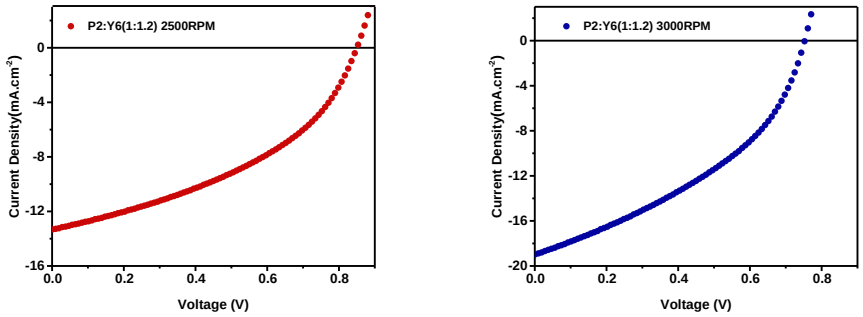


Figure 2.8. J-V characteristics of P2:Y6 with a) 2500 rpm and b) 3000 rpm

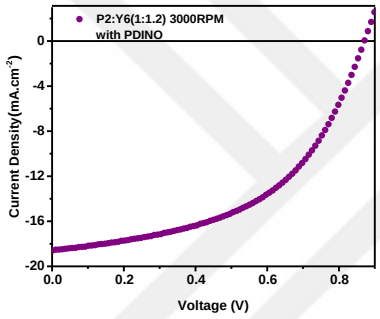


Figure 2.9. J-V characteristics of P2:Y6 with PDINO

2.4.3 P3-Based Device

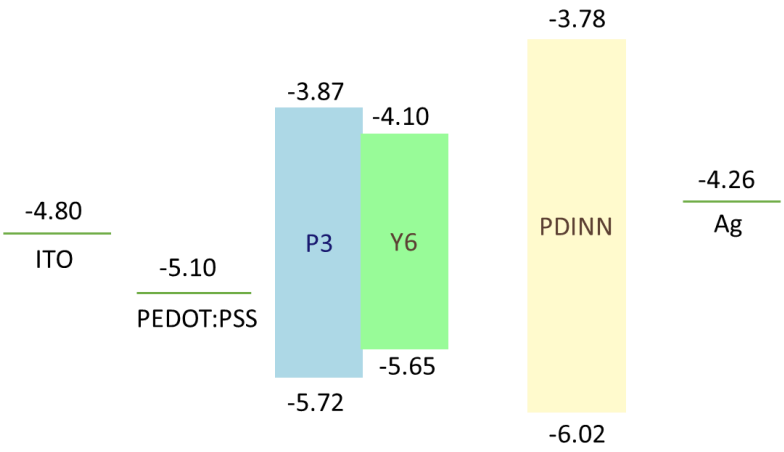


Figure 2.10. Energy level diagram of P3-based device

Table 2.7 Device performance of P3-based device

Polymer Blend	Solvent	D:A Ratio	Coating Rate	Ag Thickness (nm)	PCE (%)	FF (%)	V_{oc} (V)	J_{sc} (mA.cm^{-2})
P3:Y6	$CHCl_3$	1:1.2	2500	100	1.37	37.54	0.73	4.98
P3:Y6	$CHCl_3$	1:1.2	3000	100	1.48	37.53	0.72	5.50

Devices produced using **P3** polymer and Y6 acceptor exhibited the lowest performance values. At 2500 and 3000 rpm coating rates, the power conversion efficiencies obtained in these devices without additives remained at the level of 1.37% and 1.48%, respectively. J_{SC} was obtained as 5.50 mA/cm^{-2} at most, which is significantly lower than other polymer systems. Although FF values (~37.5%) were within reasonable limits, the device efficiency was limited due to inadequate V_{OC} (0.72–0.73 V) and J_{SC} values. The main reason for this low performance is based on the structural properties of the **P3** polymer. In the **P3** structure, there is a chlorinated quinoxaline acceptor segment attached to the BDT donor unit. The two chlorine atoms in the molecule create a strong electron-withdrawing effect on the quinoxaline, lowering the LUMO level of the polymer and deepening the HOMO level. As a result, although the HOMO-LUMO gap (E_g) becomes smaller, the electron-donating property is weakened because the HOMO level is very deep (Hasegawa et al., 2019). Additionally, steric hindrance due to chlorine atoms can disrupt the conjugation plane and deplanarity of the polymer chains (Lee et al., 2023).

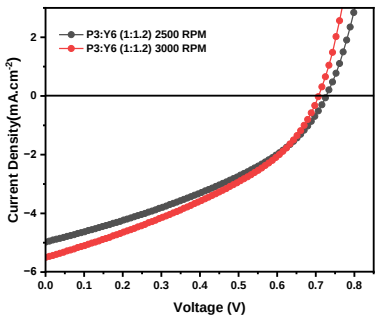


Figure 2.11. J-V characteristics of P3:Y6 with 2500 rpm coating rate and P3:Y6 with 3000 rpm coating rate

2.4.4 P4-Based Device

According to the data obtained from electrochemical characterization, **P4** has a very deep HOMO level (–6.264 eV) and a LUMO value of –3.844 eV. This structure provides a relatively wide electrochemical band gap (E_g) of –2.420 eV. Therefore, no photovoltaic response was obtained in OPV devices produced with this polymer. In donor polymers, the HOMO level should generally be between -5.2 and -5.8 eV so that both hole transport after photon absorption is possible and sufficient energy difference with the acceptor is formed. However, in **P4**, the HOMO level is quite deep at -6.264 eV. Such a deep HOMO cannot deliver the hole left by the photon-excited electron to the hole transport layer (Hasegawa et al., 2019). At the same time, since the HOMO-LUMO energy difference is high, the energy of the absorbed light photon may not be sufficient for effective charge separation (Aderne et al., 2022). According to the structural analysis of the polymer, the two chlorine units in the main chain of **P4** are quite bulky. Both chlorine atoms create steric hindrance that disrupts the conjugation plane and also distribute the electron density by having an attractive effect on the electron-rich π-system (Lee et al., 2023). This reduces the conjugation length and reduces the absorption and carrier production capacity of the polymer. Also, the LUMO level of **P4** was measured as –3.844 eV. The LUMO level of Y6 is around –4.10 eV according to the literature. In this case, although electron transfer

in the donor **P4** to acceptor Y6 direction seems possible, the difference is only ~0.26 eV. It has been shown that this difference should be at least 0.3 eV for effective charge separation in OPV systems (Nakano et al., 2019).

2.4.5 P5-Based Device

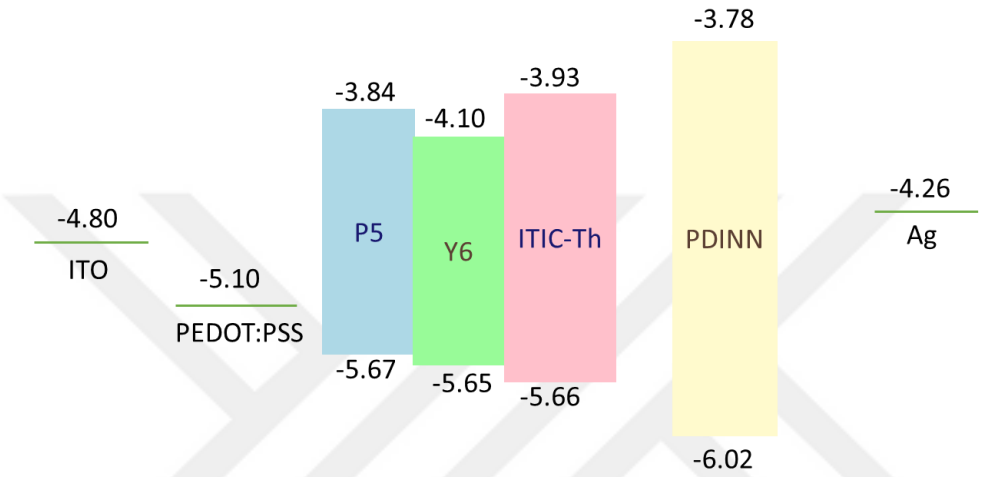


Figure 2.12. Energy level diagram of P5-based device

Table 2.8 Device performance of P5-based device

Polymer Blend	Solvent	D:A Ratio	Coating Rate	Anneal (min)	PCE (%)	FF (%)	V_{oc} (V)	J_{sc} (mA.cm^{-2})
P5:Y6	$CHCl_3$	1:1.2	2500	10	4.21	40.97	0.77	13.33
P5:Y6	$CHCl_3$	1:1.2	3000	10	3.57	40.90	0.79	11.05
P5:Y6	$CHCl_3$	1:1.2	3000	5	4.84	37.99	0.79	16.13

At a 2500 rpm coating rate, the device operated with 4.21% PCE, 40.97% FF, 0.77 V $V_{OC,}$ and 13.33 mA/cm^{-2} J_{SC}. When the higher raate of 3000 rpm was used, PCE decreased to 3.57% and J_{SC} decreased to 11.05 mA/cm^{-2}. FF remained at a similar level. These results show that lower coating speeds result in thicker film production, thus increasing light absorption. Thick films can limit charge transport while providing optical gain. However, the higher J_{SC} value obtained at 2500 rpm shows

that the absorption advantage outweighs charge losses. In thinner films produced at higher speeds, charge production and absorption were insufficient, which reduced J_{SC} and reduced overall device efficiency (Zakaria & Malik, 2023). The device performance increased significantly when the annealing time was reduced from 10 to 5 minutes while the coating rate was constant at 3000 rpm. In particular, J_{SC} increased from 11.05 to 16.13 mA/cm^{-2}, PCE from 3.57% to 4.84%. FF slightly decreased from 40.9% to 37.99%. V_{OC} remained constant. These findings indicate that prolonged annealing for 10 minutes may cause morphological deterioration. Prolonged heat treatment may disrupt the carrier paths by causing excessive crystallinity or domain growth instead of optimizing the separation of donor-acceptor phases (Verploegen et al., 2010). On the other hand, shorter annealing for 5 minutes allowed J_{SC} to increase by 46% by providing proper microphase separation. Despite the slight decrease in FF, PCE reached the highest level of 4.84%. **P5** provides good π-π stacking and planar chain conformation. This structure increased charge mobility and allowed FF to remain at reasonable levels of 37–41%. However, the lack of additives and the effect of annealing times may have prevented FF from reaching higher values.

a) b)

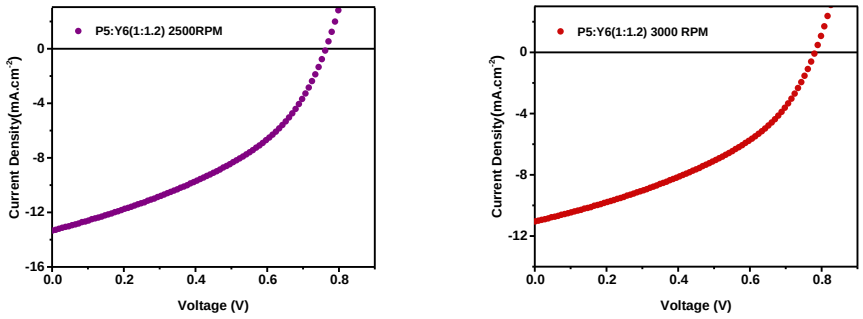


Figure 2.13. J-V characteristics of a) P5:Y6 with 2500 rpm coating rate and 10 minutes anneal and b) P5:Y6 with 3000 rpm coating rate and 10 minutes anneal

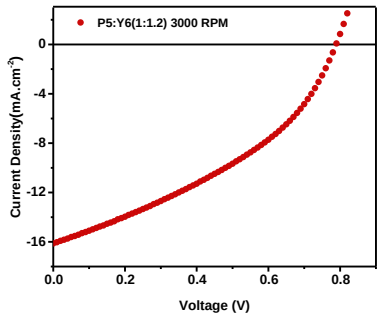


Figure 2.14. J-V characteristics of P5:Y6 with 5 minutes anneal

2.4.6 P6-Based Device

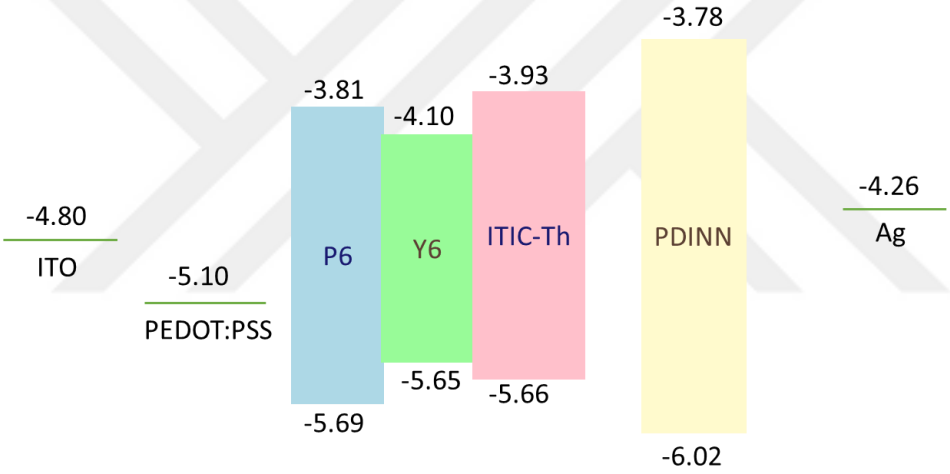


Figure 2.15. Energy level diagram of P6-based device

Table 2.9 Device performance of P6-based device

Polymer Blend	Solvent	D:A Ratio	Coating Rate	PCE (%)	FF (%)	V_{oc} (V)	J_{sc} (mA.cm^{-2})
P6:Y6	$CHCl_3$	1:1.2	2500	7.02	45.18	0.84	18.40
P6:Y6	$CHCl_3$	1:1.2	3000	6.77	45.24	0.84	17.92
P6:Y6	$CHCl_3$	1:1.2	2500	6.43	46.70	0.82	16.85

The HOMO level of P6 is measured as -5.690 eV and the LUMO level is measured as -3.814 eV. This energy level arrangement aligns well with the LUMO level of Y6. The HOMO-LUMO gap is calculated as 1.876 eV. The HOMO level is relatively shallow, which is advantageous for hole transport and contributes to the high level of V_{OC} of 0.82–0.84 V (Yuan et al., 2019). In addition, devices fabricated at 2500 rpm (7.02%, 6.43%) have higher J_{SC} values (18.40, 16.85 mA cm^{-2}), while the J_{SC} decreased to 17.92 mA cm^{-2} and PCE was 6.77% in the device fabricated at 3000 rpm. Lower coating rate allowed thicker film to be obtained, which resulted in increased absorption. Increased light absorption increased charge generation, thus increasing J_{SC}. On the other hand, thinner film produced at 3000 rpm did not cause a significant decrease in FF (45.24%) because carriers traveled shorter distances (Zakaria & Malik, 2023). FF value was around 45% in all devices. This value is considered quite good for additive-free systems. This shows that the chain planarity of P6 is sufficient and micro-phase separation occurs in a controlled manner even without additives (Garcia Romero et al., 2021). However, better FF and J_{SC} values could have been obtained if additives (e.g. CN) were used.

a) b)

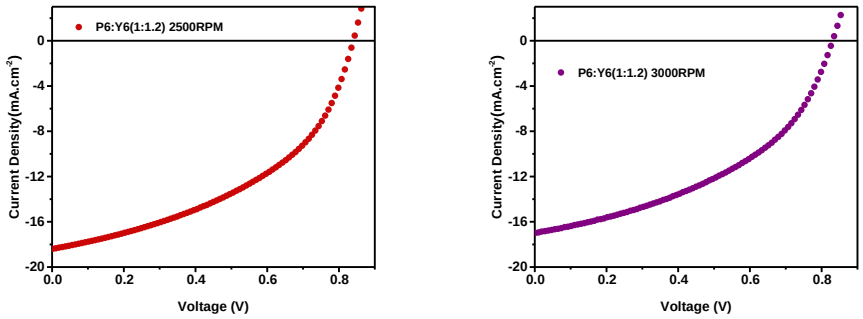


Figure 2.16. J-V characteristic of a) P6:Y6 with 2500 rpm coating rate and b) P6:Y6 with 3000 rpm coating rate

2.4.7 External Quantum Efficiency (EQE) Spectrum of Polymers

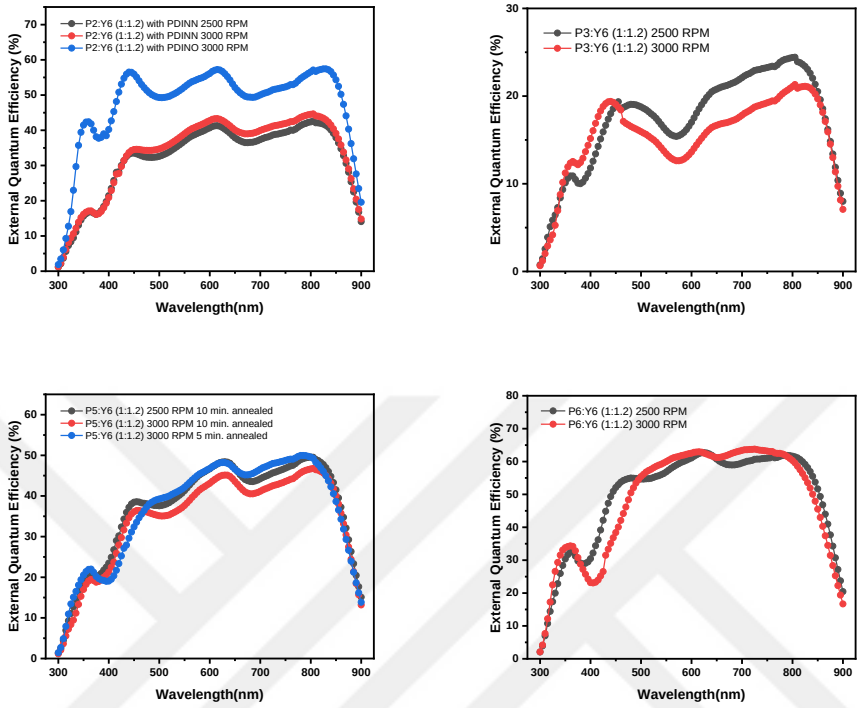


Figure 2.17. EQE spectrum of the polymers

The P2:Y6 device using the PDINO interlayer exhibits higher EQE at all wavelengths compared to the PDINN samples, producing a larger area and Jsc around 23–24 mA cm^{-2}, while films coated at 3000 rpm provide additional efficiency gains due to the reduction of the electron exit barrier and the shortening of the carrier collection path. In the P3:Y6 set, both the absolute EQE remains low and a significant decrease is observed in the 550–650 nm range, resulting in limited Jsc due to insufficient phase separation and carrier losses originating from the deep HOMO level. Optimum performance for the **P5** polymer is achieved in thin films prepared at short annealing (5 min) and high speed (3000 rpm); long annealing time or thick films lead to phase growth, reducing EQE. Offering high mobility thanks to its planar and halogenated core, P6:Y6 is more tolerant to film thickness and reaches higher Jsc values at both speeds; The extra absorption at 330–450 nm comes from the chlorinated-BDT band of the donor. In general, energy level alignment (PDINO

> PDINN), optimum film thickness, short annealing and planarity/delocalization are the main factors that increase the EQE curves in order, while the integrated Jsc order is P2/PDINO > P6 > P5(opt) > P2/PDINN > P3 for all polymers which closely matches the J-V readings.

2.4.8 Comparison of the Polymers

When the photovoltaic device performances of the polymers were compared, it was observed that small changes in the structure had significant effects on the device efficiencies. The first of the polymer pairs with similar core structures, **P1** and **P2**, both contain difluorinated quinoxaline units, but P1 has a thienothiophene BDT core, while **P2** has a chlorine-substituted BDT core. When these two polymers were compared, **P2** devices presented higher V_{OC} (0.87 V), FF (50.33%) and PCE (8.16%) values, while P1 showed a more limited performance (5.99% PCE). This difference can be attributed to the increase in V_{OC} due to the stabilization of the HOMO level by the chlorinated structure of BDT and the increase in FF due to the improvement in phase separation.

The second pair, **P3** and **P4**, are polymers containing dichlorinated quinoxaline. While **P3** devices operated with very low efficiency (1.48% PCE), devices produced with **P4** did not operate at all. The HOMO levels of both polymers are quite deep, but in **P4** this level is the lowest in the system at –6.264 eV. This extremely deep HOMO level made hole transport difficult and charge separation impossible, resulting in the device being completely passive. In addition, steric hindrances in both dichlorinated BDT and dichlorinated quinoxaline structures disrupted planarity, restricted the conjugation length, and prevented the formation of carrier paths.

The last pair, **P5** and **P6**, are monofluorinated quinoxaline derivatives. **P6** (containing dichlorinated BDT) showed a significantly better performance than **P5** (7.02% PCE vs 4.84% PCE). FF (45.18%) and J_{SC} (18.40 mA/cm^{-2}) values were high in P6 devices, which can be attributed to the positive effects of the chlorine-

substituted BDT core on phase separation and electron mobility. In P5 devices, despite the more planar structure, morphological integrity was not sufficiently achieved, causing FF to remain lower.

In general, when all polymers were compared, the highest performing devices were obtained with **P2** and **P6** polymers containing 2F and 1F quinoxaline and carrying the dichlorinated BDT core. The success in these polymers is due to the ideal balance between the HOMO level and V_{OC} and the ability to provide sufficient phase separation even in additive free conditions. In systems such as **P3** and especially **P4** containing dichlorinated quinoxaline, both energy level alignment and morphology deterioration rendered the devices dysfunctional.

CHAPTER 3

EXPERIMENTAL PART

3.1 Materials

Chemicals used in the experiments were provided by Solarmer, Merck, and Tokyo Chemical Industry (TCI). Unless otherwise stated, all reactions were performed in an inert nitrogen atmosphere. The Mbraun MBSPS5 solvent drying system was used to obtain dry solvents. Calcium hydride, a drying agent, was used to distill triethylamine. Additionally, four-inch molecular sieves were added to the liquid phase to remove moisture from the liquids. For column chromatography, Merck Silica Gel 60 with a particle size range of 230–400 mesh served as the stationary phase. Thin layer chromatography was carried out using commercially available 0.25 mm Merck Silica Gel 60 plates.

3.2 Instrumentation and Methods

Bruker Spectrospin Avance DPX-400MHz spectrometer was used to determine ^{1}H-NMR and ^{13}C-NMR spectra of molecules. Parts per million (ppm) was used to indicate chemical shifts, and trimethylsilane (TMS) was used as an internal standard. Deuterated $CDCl_3$ was preferred as a solvent in obtaining ^{13}C-NMR and ^{1}H-NMR spectra. In order to determine the exact molecular masses of monomers, analyses were performed with high-resolution mass spectrometry (Waters Synapt MS system). Molecular weight distributions of the obtained polymers were analyzed using polystyrene as an external standard by gel permeation chromatography (Shimadzu-20A) method. Chloroform was used as a solvent in the solutions prepared for this device. Differential Pulse Voltammetry in the Gamry 600 Potentiostat device was used to perform electrochemical characterizations. UV-Visible region

spectroscopy was applied by Varian Cary 5000 model spectrometer to examine optical properties. Photovoltaic performance measurements were performed using Keithley 2400 device under a 1.5 G sun simulation and 100 mW/cm² light intensity.

3.3 Synthesis Pathway of Acceptor Monomers

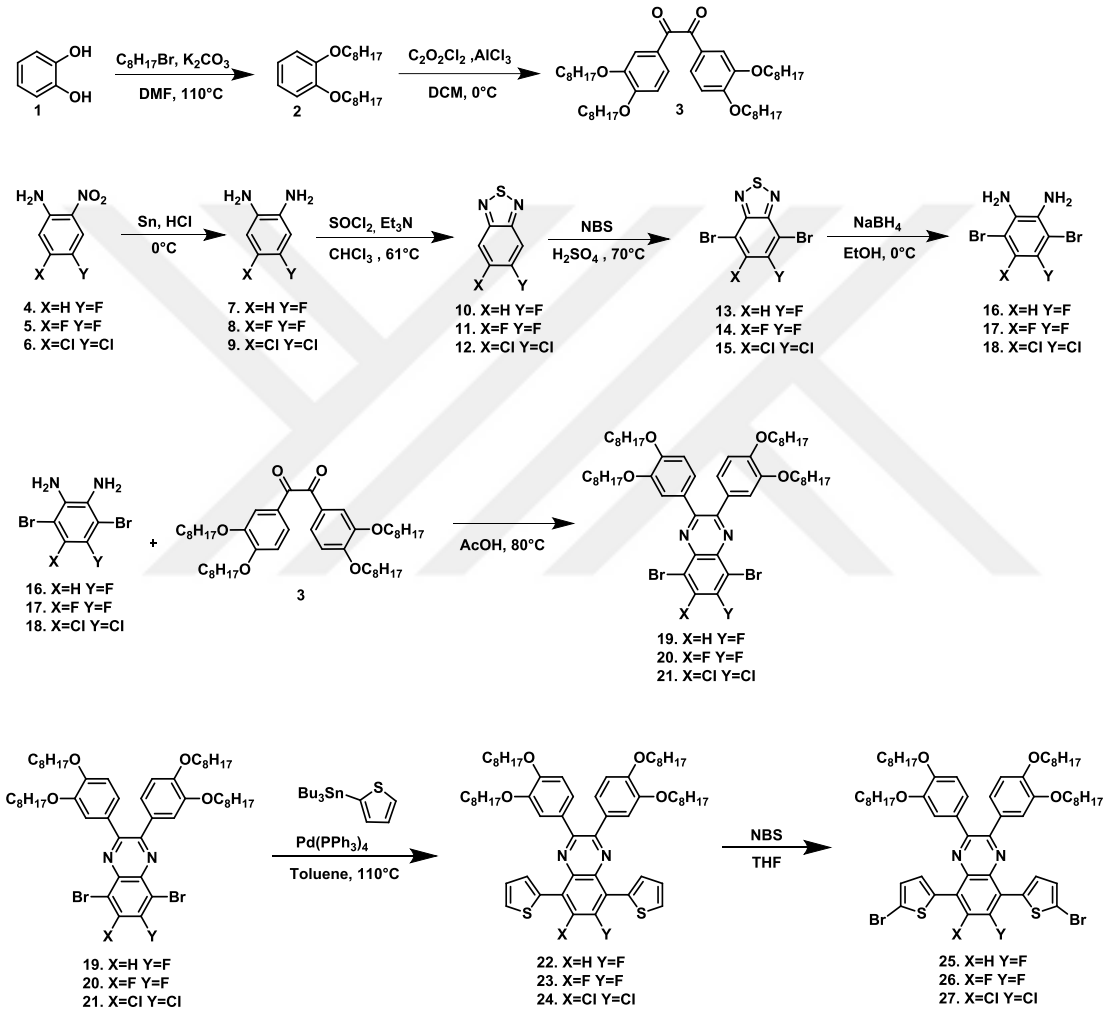


Figure 3.1. Synthesis pathway of acceptor monomers

3.3.1 Synthesis Pathway of Molecule 2

The monomer synthesis forming the acceptor polymer was initiated with catechol (**molecule 1**). First, 2 grams of catechol (18.16 mmol), 10.04 g of potassium carbonate (K_2CO_3) (72.65 mmol), and 60 mL of anhydrous dimethylformamide (DMF) were added to a two-necked reaction flask with a volume of 250 ml. The temperature of the mixture was increased to 60°C and stirred at this temperature for half an hour. Then, 12.28 grams (63.57 mmol) of $C_8H_{17}Br$ was added, and the temperature was increased to 110°C, and the reaction was continued under a nitrogen atmosphere. The reaction, which lasted for three days, was terminated by monitoring with thin layer chromatography (TLC). The solids formed in the reaction mixture were separated with the help of filter paper. The DMF solvent in the obtained filtrate was evaporated under vacuum. The remaining compounds were extracted three times with dichloromethane (DCM) and brine. The organic phase was then dried with magnesium sulfate ($MgSO_4$) and filtered, and then the solvent was removed under reduced pressure to obtain the crude product. This crude material was purified by column chromatography using silica gel and hexane. As a result, "**Molecule 2**" was isolated as a pale white liquid (5,50 grams, 90,6% yield). ^{1}H NMR (400 MHz, Chloroform-*d*) δ 6.89 (s, 4H), 3.99 (t, *J* = 6.7 Hz, 4H), 1.82 (p, 4H), 1.47 (p, 4H), 1.39 – 1.26 (m, 16H), 0.89 (t, 6H). ^{13}C NMR (100 MHz, $CDCl_3$) δ 148.2, 120.0, 113.1, 68.2, 30.8, 28.4, 28.3, 28.3, 25.0, 21.7, 13.1.

3.3.2 Synthesis Pathway of Molecule 3

5.5 grams (16.98 mmol) of **molecule 2** was added to a 250 mL two-necked reaction flask. The system was kept under vacuum for 10 minutes to remove air and moisture from the medium. Then, 1.26 grams (9.68 mmol) of $AlCl_3$ and 10 mL of DCM were combined in the reaction vessel under nitrogen atmosphere and the mixture was placed in an ice bath and the temperature was reduced to 0°C. After mixing 10 mL of DCM and 0.86 mL (9.46 mmol) of oxalyl chloride ($C_2\ O_2\ Cl_2$) until it became

homogeneous, this mixture was slowly added to the reaction medium by dripping with a stopper. Approximately one hour after the process, the mixture was brought to room temperature and the reaction was continued for 18 hours. At the end of 18 hours, the completion of the reaction was confirmed by thin layer chromatography (TLC) and the process was stopped. The resulting mixture was poured into 1 M hydrochloric acid solution containing 37% HCl and stirred for approximately 1 hour. Then, the mixture was extracted three times using DCM and distilled water. The resulting organic layer was dried with $Na_2\ SO_4$ and filtered. After this filtering process, the solvent was evaporated under reduced pressure. In the last step, crystallization with ethanol was carried out and **Molecule 3** was obtained in white and pure form (3.05 grams, 47.6% yield). ^{1}H NMR (400 MHz, Chloroform-*d*) δ 7.56 (d, *J* = 2.0 Hz, 2H), 7.42 (dd, *J* = 8.4, 2.0 Hz, 2H), 6.84 (d, *J* = 8.5 Hz, 2H), 4.05 (t, *J* = 6.7, 8H), 1.84 (p, 8H), 1.51 – 1.42 (m, 8H), 1.33 – 1.24 (m, 32H), 0.88 (t, *J* = 7.1 Hz, 12H). ^{13}C NMR (100 MHz, $CDCl_3$) δ 192.8, 154.0, 148.3, 125.2, 125.1, 111.3, 110.6, 68.2, 68.1, 30.8, 30.8, 28.3, 28.3, 28.6, 28.2, 28.1, 27.9, 25.0, 24.9, 21.7, 21.6, 13.1, 13.1.

3.3.3 Synthesis Pathway of Molecules 7, 8, 9

2.00 grams of 4-fluoro-2-nitroaniline (**molecule 4**) (12.81 mmol) and 60 mL of 37% hydrochloric acid were transferred to a 250 mL two-necked reaction flask under a nitrogen atmosphere. After waiting for the compound to completely dissolve in HCl, the mixture was placed in an ice bath, and the temperature was lowered to 0°C with the help of an ice bath. A total of 7.36 grams (62.01 mmol) of tin was added to the reaction mixture in three portions over a 20-minute period. After the mixture was stirred at 0°C for 3 hours, the air inside was evacuated with a syringe and kept in the freezer overnight. The next day, 8 M NaOH solution was added to adjust the pH to 10. The mixture was then extracted three times with water and ethyl acetate. The organic phase was dried with $Na_2\ SO_4$, filtered, separated from the salt, and removed from the solvent under reduced pressure. As a result of these operations,

1.60 grams of **Molecule 7** was obtained as a white solid (73.0% yield). Since the amine groups are very sensitive to oxygen and moisture, the substance was taken directly to the next reaction without purification. **Molecule 8** and **Molecule 9** have the same procedure as **Molecule 7** and were synthesized by the synthesis route explained above. The yields obtained as a result of the added reactants and reaction for **Molecule 8** and **Molecule 9** are given in the table below.

Table 3.1 Reactants and yields of Molecule 8 and Molecule 9

Reactants	**Sn (g)**	**Synthesized Molecule**	**Yield**
Molecule 5 (4,5-difluoro-2-nitroaniline) (2 g) (11.49 mmol)	6.60 (55.60 mmol)	**Molecule 8**	1.55 g 90% yield
Molecule 6 (4,5-dichloro-2-nitroaniline) (1 g) (11.49 mmol)	2.78 (23.38 mmol)	**Molecule 9**	850 mg 90% yield

3.3.4 Synthesis Pathway of Molecules 10, 11, 12

1.04 grams of **molecule 7** (8.25 mmol) was taken into a 100 mL Schlenk tube. After waiting under vacuum for five minutes, 25 mL of anhydrous chloroform was added under N_2 atmosphere. Then, 4.60 mL of dry triethylamine (32.98 mmol) was added to the mixture. After molecule 7 was completely dissolved, the tube was placed in an ice bath and the temperature was lowered to 0°C. At this stage, 1.20 mL of thionyl chloride (16.49 mmol) was slowly added dropwise. Then, the temperature of the mixture was increased to 61°C, and the reaction was continued for 24 hours. The next day, after confirming the completion of the reaction by TLC, the mixture was extracted with chloroform. The organic phase was washed three times with water, dried with $Na_2 SO_4$ and filtered. The solvents were removed under reduced pressure

to give an orange solid. This solid was purified by column chromatography (silica,1 Hexane: 3 DCM) to give **Molecule 10** (665 mg, 67.3% yield). Since the substance sublimes readily at room temperature, it was used in the next step without delay. **Molecule 11** and **Molecule 12** have the same procedure as **Molecule 10** and were synthesized by the synthesis route explained above. The yields obtained as a result of the added reactants and reaction for **Molecule 11** and **Molecule 12** are given in the table below.

Table 3.2 Reactants and yields of Molecule 11 and Molecule 12

Reactants	**Et_3N(mL)**	**$SOCl_2$**	**Synthesized Molecule**	**Yield**
Molecule 8 (1.56 g) 10.80 mmol)	4.92 (35.33 mmol)	1.29 (17.61 mmol)	**Molecule 11**	1.40 g 80% yield
Molecule 9 (850 mg) (4.85 mmol)	2.20 ;8,15.70 mmol)	0.570 (7.80 mmol)	**Molecule 12**	670 mg 69.7% yield

3.3.5 Synthesis Pathway of Molecules 13, 14, 15

1 gram of **molecule 10** (6.49 mmol), 4.62 grams of n-bromosuccinimide (NBS) (25.95 mmol) and 30 mL of sulfuric acid (H_2SO_4) were taken into a two-necked reaction flask with a volume of 250 mL and the system was connected to a reflux condenser. The reaction temperature was adjusted to 70 °C and the mixture was kept at this temperature overnight. After 24 hours, it was determined by TLC that the reaction was complete and the process was terminated. The reaction mixture was transferred to a 600 mL beaker containing ice and stirred at room temperature until the ice melted completely. Then, the mixture was washed with cold water and filtered to separate the solid product. Finally, this solid was crystallized with methanol to obtain **Molecule 13** in pure white form. **Molecule 14** and **Molecule 15** have the same procedure as **Molecule 13** and were synthesized by the synthesis route explained

above. The yields obtained as a result of the added reactants and reaction for **Molecules 14** and **Molecule 15** are given in the table below **Molecule 13** ^{1}H NMR (400 MHz, Chloroform-*d*) δ 7.79 (d, *J* = 8.3, 1H). ^{13}C NMR (100 MHz, CDCl3) δ 161.5, 159.0, 150.4, 128.6, 124.2, 114.2. (99.2 signal of fluorine). **Molecule 14** ^{1}H NMR (400 MHz, $CDCl_3$). ^{13}C NMR (100 MHz, $CDCl_3$) δ 153.4, 150.8, 149.0, 99.4. **Molecule 15** ^{1}H NMR (400 MHz, $CDCl_3$) ^{13}C NMR (100 MHz, $CDCl_3$) δ 150.2, 135.3, 113.9.

Table 3.3 Reactants and yields of Molecule 14 and Molecule 15

Reactants	**NBS (g)**	**Synthesized Molecule**	**Yield**
Molecule 11 (9 mmol)	6.41 (36.01 mmol)	**Molecule 14**	1.80 g 61.3% yield
Molecule 12 3.30 mmol)	2.40 (13.10 mmol)	**Molecule 15**	1.2 g 85% yield

3.3.6 Synthesis Pathway of Molecules 16, 17, 18

567 mg of **Molecule 13** (1.82 mmol) was placed in a 250 mL two-necked reaction flask and vacuumed for 15 min. Then, 50 mL of ethanol was added under nitrogen gas. The mixture's temperature was lowered to 0 °C, and 2.63 g of $NaBH_4$ (69.49 mmol) was added to the reaction flask and continued for one day. The next day, after TLC control, the reaction was terminated, and extraction was performed with diethyl ether. The organic phase was washed three times with water, dried with Na_2SO_4, and then separated by filtration. The solvents were evaporated under vacuum, and a white solid, **molecule 16** (500 mg, 88% yield), was obtained. Since amine groups are very sensitive to moisture and oxygen, this material was taken directly to the next reaction without further purification. **Molecule 17** and **Molecule 18** have the same procedure as **Molecule 16** and were synthesized by the synthesis route explained above. The

yields obtained as a result of the added reactants and reaction for **Molecule 17** and **Molecule 18** are given in the table below.

Table 3.4 Reactants and yields of Molecule 17 and Molecule 18

Reactants	**$NaBH_4$**	**Synthesized Molecule**	**Yield**
Molecule 14 (300 mg) 9.1 mmol)	1.32 (34.76 mmol)	**Molecule 17**	270 mg 81% yield
Molecule 15 (500 mg) (1.38 mmol)	1.99 (52.69 mmol)	**Molecule 18**	464 mg 85% yield

3.3.7 Synthesis Pathway of Molecules 19, 20, 21

675 mg of **molecule 16** and 1.79 g of **molecule 3** (2.48 mmol) were put into a 250 mL schlenk tube and dissolved in 25 mL of acetic acid under a nitrogen atmosphere. The reaction proceeded for one day at 80 °C. The reaction was terminated after being controlled by TLC, and extraction was performed with chloroform. The organic phase was washed three times with water and then dried with Na_2SO_4. Na_2SO_4 was then filtered and removed from the organic phase. The solvents in the organic phase filtered under reduced pressure were evaporated and a yellow solid was obtained. The yellow solid, which was purified by column chromatography (silica, 25 Hexane:1 EtOAc) and 5 Hexane:1 DCM, contained **molecule 19** (1.60 g, 69,86% yield). **Molecule 20** and **Molecule 21** have the same procedure as **Molecule 19** and were synthesized by the synthesis route explained above. The yields obtained as a result of the added reactants and reaction for **Molecule 20** and **Molecule 21** are given in the table below. **Molecule 19** ^{1}H NMR (400 MHz, Chloroform-*d*) δ 7.87 (d, *J* = 8.0 Hz, 1H), 7.28 (d, *J* = 8.8 Hz, 2H), 7.23 (s, 2H), 6.84 (d, *J* = 8.9 Hz, 2H), 4.01 (t, *J* = 6.7 Hz, 4H), 3.86 (t, *J* = 6.7 Hz, 4H), 1.83 (p, *J* = 6.8 Hz, 4H), 1.74 (p, *J* = 6.8 Hz, 4H), 1.36 – 1.16 (m, 40H), 0.94 – 0.75 (m, 12H). ^{13}C NMR (100 MHz, CDCl3)

δ 157.6, 155.1, 154.2, 153.7, 151.0, 150.7, 148.8, 138.2, 136.6, 130.5, 130.2, 127.8, 124.0, 123.5, 122.5, 117.0, 115.5, 112.9, 108.5, 107.9, 69.3, 32.0, 29.5, 29.4, 29.3, 26.2, 22.8, 14.3. **Molecule 20** ^{1}H NMR (400 MHz, Chloroform-*d*) δ 7.19 (d, *J* = 8.1 Hz, 2H), 7.17 (s, 2H), 6.77 (d, *J* = 8.2 Hz, 2H), 3.95 (t, *J* = 6.7 Hz, 4H), 3.79 (t, *J* = 6.7 Hz, 4H), 1.77 (p, *J* = 6.8 Hz, 4H), 1.67 (p, *J* = 6.8 Hz, 4H), 1.43 – 1.16 (m, 30H), 0.84 – 0.81 (m, 12H). ^{13}C NMR (100 MHz, $CDCl_3$) δ 152.58, 150.56, 149.73, 147.67, 134.57, 129.14, 122.34, 114.37, 111.81, 108.22, 68.17, 68.08, 30.83, 28.37, 28.32, 28.26, 28.15, 28.06, 25.00, 21.66, 13.09. **Molecule 21** ^{1}H NMR (400 MHz, Chloroform-*d*) δ 7.28 (d, *J* = 8.8 Hz, 2H), 7.26 (s, 2H), 6.84 (d, *J* = 8.9 Hz, 2H), 4.02 (t, *J* = 6.7 Hz, 4H), 3.87 (t, *J* = 6.7 Hz, 4H), 1.83 (p, *J* = 6.8 Hz, 4H), 1.74 (p, *J* = 6.8 Hz, 4H), 1.50 – 1.23 (m, 40H), 0.92 – 0.85 (m, 12H). ^{13}C NMR (100 MHz, CDCl3) δ 154.1, 151.1, 148.9, 137.8, 135.1, 130.1, 125.0, 123.6, 115.6, 113.0, 69.4, 32.0, 29.5, 29.5, 29.3, 26.2, 22.8, 14.3.

Table 3.5 Reactants and yields of Molecule 20 and Molecule 21

Reactants	**Molecule 3**	**Synthesized Molecule**	**Yield**
Molecule 17 (280 mg) (9.21 mmol)	699.50 mg (967.32 μmol)	**Molecule 20**	560 mg 61% yield
Molecule 18 (464 mg) (1.38 mmol)	1.05 g 81.45 mmol)	**Molecule 21**	1.30 g 92% yield

3.3.8 Synthesis Pathway of Molecule 29

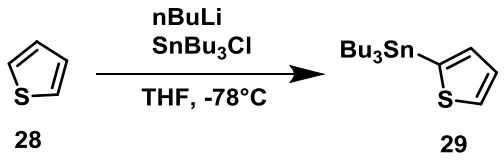


Figure 3.2. Synthesis Pathway of Molecule 29

1 g of thiophene (**Molecule 28**) (11.89 mmol) was placed in a 100 mL schlenk tube under nitrogen gas, and 30 mL of anhydrous THF was added. The reaction temperature was reduced to -78 °C, and 5.23 mL of n-BuLi (19.61 mmol in 2.5 M hexane) was slowly added over 40 minutes. The mixture was stirred at -78 °C for 1 hour, then brought to room temperature and stirred for another 1 hour. Then, the mixture's temperature was reduced to -78 °C again, and 5.80 mL of $SnBu_3Cl$ (21.39 mmol) was slowly added, and the reaction started. The reaction was stirred at room temperature for 1 day. The next day, excess n-BuLi was neutralized with distilled water, and extraction was done with chloroform. The organic phase was washed three times with distilled water, dried with Na_2SO_4, and filtered. The solvents in the filtrate were evaporated under reduced pressure to obtain a light yellow liquid (**Molecule 29**) (3.80 g, 80.1% yield). The obtained substance was used in the following reactions without additional purification. ^{1}H NMR (400 MHz, Chloroform-*d*) δ 7.58 (d, *J* = 4.7 Hz, 1H), 7.19 (dd, *J* = 4.9, 2.5 Hz, 1H), 7.13 (d, *J* = 2.8 Hz, 1H), 1.52 – 1.47 (m, 6H), 1.31 – 1.23 (m, 6H), 1.06 – 1.00 (m, 6H), 0.82 (t, *J* = 7.3 Hz, 9H). ^{13}C NMR (100 MHz, $CDCl_3$) δ 135.2, 130.6, 127.9, 29.0, 27.3, 13.7, 10.8.

3.3.9 Synthesis Pathway of Molecules 22, 23, 24

382 mg **Molecule 19** (393.1 μmol) and 323 mg **Molecule 29** (865.51 μmol) were placed in a 100 mL Schlenk tube. After 10 minutes of vacuum, 20 mL of dry toluene was added under nitrogen gas and mixed. After degassing the reaction for 10 min, 19.33 mg of Bis(triphenylphosphine)palladium (II) dichloride $PdCl_2(PPh_3)_2$ (27.54 μmol) was finally added to the mixture. The reaction was heated at 100°C for 24 hours. After the reaction, the control was made by TLC, the mixture was evaporated under reduced pressure and purified by silica column chromatography (2 Hexane: 1 Chloroform). As a result, a red solid (**molecule 22**) was obtained (250 mg, 65.1% yield). **Molecule 23** and **Molecule 24** have the same procedure as **Molecule 22** and were synthesized by the synthesis route explained above. The yields obtained as a result of the added reactants and reaction for **Molecule 23** and **Molecule 24** are given in the table below. **Molecule 22** ^{1}H NMR (400 MHz, Chloroform-*d*) δ 7.94 (d, *J* = 2.9 Hz, 1H), 7.89 (d, *J* = 13.3 Hz, 1H), 7.79 (d, *J* = 3.8 Hz, 1H), 7.48 (d, *J* = 5.2 Hz, 1H), 7.47 (d, *J* = 1.1 Hz, 1H), 7.39 (d, *J* = 14.1 Hz, 2H), 7.16 – 7.11 (m, 2H), 6.77 (t, *J* = 8.1 Hz, 2H), 3.97 – 3.94 (m, 4H), 3.87 (t, *J* = 6.7 Hz, 4H), 1.80 – 1.72 (m, 8H), 1.46 – 1.17 (m, 40H), 0.82 (t, *J* = 3.5 Hz, 12H). ^{13}C NMR (100 MHz, $CDCl_3$) δ 158.9, 156.4, 150.6, 149.3, 149.1, 147.6, 137.2, 136.4, 132.9, 130.9, 130.0, 129.1, 128.6, 127.7, 125.8, 125.4, 122.6, 115.6, 115.3, 114.6, 111.6, 68.0, 30.8, 28.4, 28.3, 28.2, 25.1, 21.7, 13.1. **Molecule 23** ^{1}H NMR (400 MHz, Chloroform-*d*) δ 7.97 (d, *J* = 3.8 Hz, 2H), 7.53 (d, *J* = 3.9 Hz, 2H), 7.38 (s, 2H), 7.19 (d, *J* = 8.2 Hz, 2H), 7.17 (t, *J* = 3.8 Hz, 2H), 6.77 (d, *J* = 8.3 Hz, 2H), 3.95 (t, *J* = 6.7 Hz, 4H), 3.87 (t, *J* = 6.7 Hz, 4H), 1.81 – 1.69 (m, 8H), 1.44 – 1.14 (m, 40H), 0.85 – 0.78 (m, 12H). ^{13}C NMR (100 MHz, $CDCl_3$) δ 150.00, 149.15, 147.65, 133.24, 129.92, 129.70, 129.58, 128.59, 125.56, 122.47, 116.63, 114.63, 111.59, 98.96, 68.14, 68.04, 30.83, 30.81, 28.38, 28.37, 28.34, 28.27, 28.20, 28.14, 25.07, 25.01, 21.68, 21.66, 13.10. **Molecule 24** ^{1}H NMR (400 MHz, Chloroform-d) δ 7.59 (d, J = 5.0 Hz, 2H), 7.47 (d, J = 5.0 Hz, 2H), 7.28 (s, 2H), 7.23 (t, J = 5.1 Hz, 2H), 7.09 (d, J = 8.4 Hz, 2H), 6.72 (d, J = 8.5 Hz, 2H), 3.97 (t, J = 6.7 Hz, 4H), 3.82 (t, J = 6.7 Hz, 4H), 1.84-1.59 (m, 8H),

1.47 – 1.25 (m, 40H), 0.91-0.86 (m, 12H). ^{13}C NMR (100 MHz, $CDCl_3$) δ 150.54, 149.33, 147.63, 136.86, 134.22, 132.99, 131.69, 129.74, 129.68, 126.64, 125.19, 122.21, 114.25, 111.52, 68.07, 67.96, 30.85, 30.80, 29.89, 28.36, 28.34, 28.25, 28.18, 28.13, 25.06, 24.99, 21.69, 21.65, 13.09, 13.07.

Table 3.6 Reactants and yields of Molecule 23 and Molecule 24

Reactants	**Molecule 29**	**$PdCl_2(PPh_3)_2$**	**Synthesized Molecule**	**Yield**
Molecule 20 (400 mg) (404 μmol)	332.06 mg (889.81 μmol)	19.87 mg	**Molecule 23**	350 mg 87.10% yield
Molecule 21 (500 mg) (489.29 μmol)	401.71 mg (1.08 μmol)	24.04 mg	**Molecule 24**	490 mg 97.42% yield

3.3.10 Synthesis Pathway of Acceptor Monomers (Molecules 25, 26, 27)

200 mg of **Molecule 22** (190.16 μmol) was added to a 250 mL two-necked reaction flask. Then, vacuum was applied for 10 minutes, and 50 mL of chloroform and 135.11 mg (740.62 μmol) of N-bromosuccinimide (NBS) were added under a nitrogen atmosphere. The mixture was stirred at room temperature for 1 day, and the reaction was terminated by checking with TLC. The product was extracted with chloroform. The organic phase was washed three times with water, dried with Na_2SO_4, then Na_2SO_4 was filtered and removed from the organic phase. The solvents in the organic phase were evaporated under reduced pressure and purified by silica column chromatography (3 Hexane: 1 Chloroform). As a result, a red solid (**molecule 25**) was obtained (205 mg, 76.2% yield). **Molecule 26** and **Molecule 27** have the same procedure as **Molecule 25** and were synthesized by the synthesis route

explained above. The yields obtained as a result of the added reactants and reaction for **Molecule 26** and **Molecule 27** are given in the table below. **Molecule 25** ^{1}H NMR (400 MHz, Chloroform-d) δ 7.80 (d, J = 13.7 Hz, 1H), 7.69 (d, J = 4.2 Hz, 1H), 7.56 (d, J = 14.0 Hz, 2H), 7.45 (d, J = 4.0 Hz, 1H), 7.07 (dd, J = 7.9, 4.1 Hz, 2H), 7.02 (dd, J = 8.4, 2.1 Hz, 2H), 6.72 (dd, J = 8.4, 4.2 Hz, 2H), 4.05 (t, J = 5.8 Hz, 4H), 3.96 (t, J = 6.7 Hz, 4H), 1.89 – 1.75 (m, 8H), 1.47 – 1.17 (m, 32H), 0.82 (t, J = 4.0 Hz, 12H). ^{13}C NMR (100 MHz, $CDCl_3$) δ 159.2, 156.5, 151.2, 149.3, 149.1, 148.1, 148.1, 137.2, 132.3, 129.6, 129.4, 129.3, 128.1, 128.0, 124.8, 124.6, 124.4, 122.7, 122.5, 117.2, 115.1, 114.2, 111.3, 98.9, 68.2, 68.0, 30.8, 28.4, 28.3, 25.0, 21.7, 13.1. **Molecule 26** ^{1}H NMR (400 MHz, Chloroform-*d*) δ 7.77 (d, *J* = 4.1 Hz, 2H), 7.62 (s, 2H), 7.16 (d, *J* = 4.2 Hz, 2H), 7.06 (d, *J* = 8.3 Hz, 2H), 6.77 (d, *J* = 8.4 Hz, 2H), 4.10 (t, *J* = 6.4 Hz, 4H), 4.03 (t, *J* = 6.6 Hz, 4H), 1.90 – 1.82 (m, 8H), 1.55 – 1.24 (m, 40H), 0.92 – 0.86 (m, 12H). ^{13}C NMR (100 MHz, $CDCl_3$) δ 176.52, 150.39, 149.25, 148.09, 132.38, 131.54, 129.63, 129.20, 128.26, 122.66, 117.60, 115.84, 114.17, 111.29, 68.24, 68.03, 30.84, 30.82, 28.55, 28.45, 28.41, 28.28, 28.23, 25.20, 25.04, 21.69, 21.67, 13.10. **Molecule 27** ^{1}H NMR (400 MHz, Chloroform-*d*) δ 7.35 (s, 2H), 7.24 (d, *J* = 3.9 Hz, 2H), 7.10 (d, *J* = 3.9 Hz, 2H), 6.97 (d, *J* = 8.4 Hz, 2H), 6.65 (d, *J* = 8.4 Hz, 2H), 3.95 – 3.85 (m, 8H), 1.75 (p, *J* = 6.9 Hz, 8H), 1.47 – 1.31 (m, 8H), 1.30 – 1.13 (m, 32H), 0.84 – 0.79 (m, 12H). ^{13}C NMR (100 MHz, $CDCl_3$) δ 150.88, 149.42, 147.86, 136.17, 135.28, 132.73, 130.56, 130.32, 129.31, 128.02, 122.26, 114.32, 113.70, 111.25, 68.01, 67.91, 30.84, 30.80, 28.40, 28.36, 28.33, 28.26, 28.20, 28.15, 25.14, 24.98, 21.69, 21.65, 13.12, 13.09.

Table 3.7 Reactants and yields of Molecule 25 and Molecule 26

Reactants	**NBS**	**Synthesized Molecule**	**Yield**
Molecule 23 (214 mg) (214.98 μmol)	153 mg (859.93 μmol)	**Molecule 26**	230 mg 93% yield
Molecule 24 (323 mg) (314.10 μmol)	223.62 mg (1.26 mmol)	**Molecule 27**	360 mg 96.50% yield

3.4 Synthesis Pathway of Donor Monomers

3.4.1 Synthesis Pathway of Donor Monomer 1

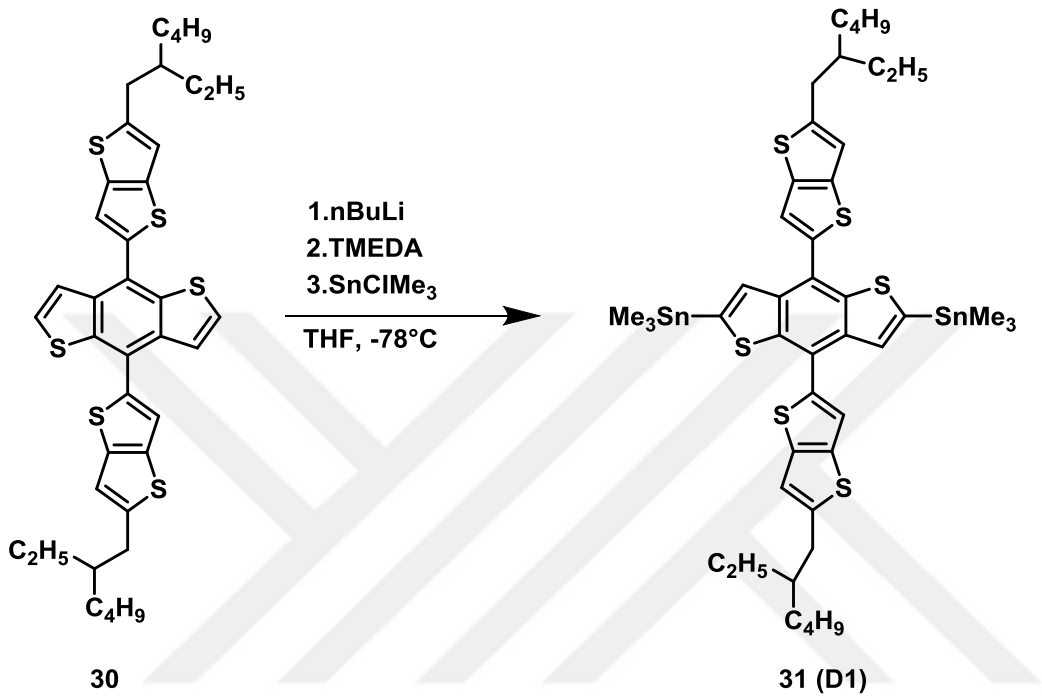


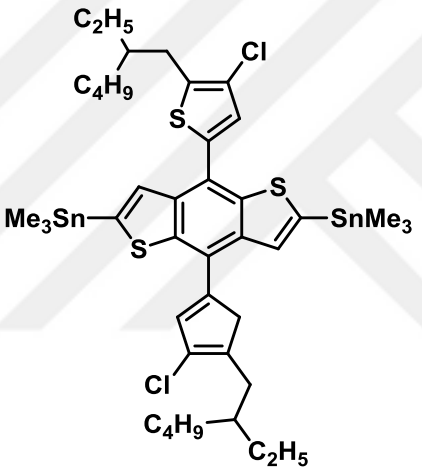
Figure 3.3. Synthesis Pathway of Donor Monomer 1

Molecule 30 is supplied commercially. To synthesize **molecule 31 (D1)**, 1 g of molecule 30 (1.45 mmol) and 0.7 mL of TMEDA (4.34 mmol) were dissolved in a 100-mL schlenk tube with 25 mL of anhydrous THF under nitrogen gas. The reaction temperature was lowered to -78 °C, and 1.45 ml of 2.5 M n-BuLi (3.62 mmol) was slowly added to the schlenk tube. The reaction was stirred at -78 °C for 1 hour and then at room temperature for 1 hour. Then, 4.34 ml of 1.0 M trimethyltin chloride (C_3H_9ClSn) (4.34 mmol) was slowly added to the reaction medium at -78 °C. The reaction was then returned to room temperature and continued for 1 day. The next day, excess n-BuLi was quenched with distilled water, and extraction was performed with diethyl ether and brine. The organic phase was washed with water three times, then dried using sodium sulfate ($Na_2 SO_4$) and separated by filtration. The resulting organic solution was converted into a yellow solid by removing the solvent under

reduced pressure. This yellow solid was purified by crystallization in dry acetone, and finally, a pure yellow solid product **Molecule 31 (D1)** was obtained (1.20 g, 80.30 % yield). ^{1}H NMR (400 MHz, Chloroform-*d*) δ 7.67 (s, 2H), 7.52 (s, 2H), 6.97 (s, 2H), 2.86 – 2.80 (m, 4H), 1.67 – 1.59 (m, 2H), 1.34 – 1.26 (m, 16H), 0.88 (t, *J* = 7.2 Hz, 12H).

3.4.2 Synthesis Pathway of Donor Monomer 2

Donor monomer 2 (**Molecule 32**) was supplied commercially and used in the synthesis of 3 polymers.



35 (D2)

Figure 3.4. Structure of donor monomer 2

3.5 Synthesis Pathway of Polymers

3.5.1 Synthesis Pathway of P1

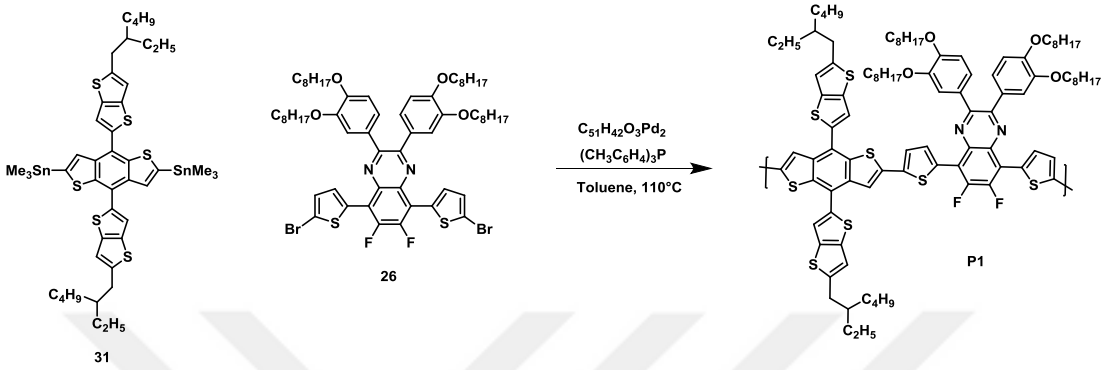


Figure 3.5. Synthesis pathway of P1

150 mg of **Molecule 26** (130.07 μmol) and 165.09 mg of **Molecule 31** (113.42 μmol) were taken into a 20 mL Schlenk tube and kept under vacuum for half an hour. Then, the tube was filled with nitrogen atmosphere, and 8 mL of anhydrous toluene was added. Immediately afterwards, 4.75 mg (15.61 μmol) $(CH_3C_6H_4)_3P$ and 5.96 mg (6.50 μmol) $C_{51}H_{42}O_3Pd_2$ were rapidly added. The mixture was heated in an oil bath at 110 °C. When it was observed that insoluble substances were formed during the reaction, the process was stopped after 9 hours. The mixture was cooled to room temperature and transferred into 50 mL cold methanol, to which 5 mg of palladium scavenger was added and stirred for 1 hour. The obtained product was collected by filtration and dried with an air flow. Then, using a Soxhlet apparatus, the polymer was purified with solvents such as methanol, acetone, hexane, and chloroform. The chloroform fraction was collected under reduced pressure, and then the solid was isolated by precipitation with methanol (220 mg, 90% yield).

3.5.2 Synthesis Pathway of P3

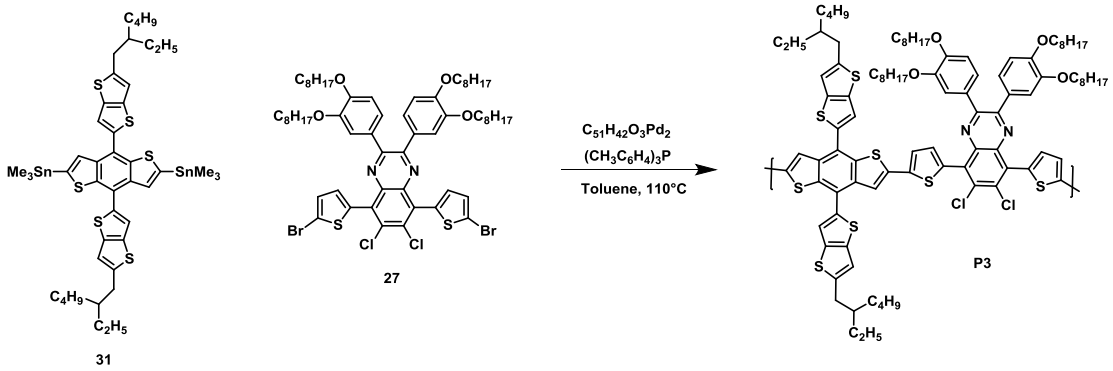


Figure 3.6. Synthesis pathway of P3

150 mg of **Molecule 27** (126.46 μmol) and 160.51 mg of **Molecule 31** (126.46 μmol) were taken into a 20 mL Schlenk tube and kept under vacuum for half an hour. Then, the tube was filled with nitrogen atmosphere, and 8 mL of anhydrous toluene was added. Immediately afterwards, 5.79 mg (6.32 μmol) $(CH_3C_6H_4)_3P$ and 4.62 mg (15.18 μmol) $C_{51}H_{42}O_3Pd_2$ were rapidly added. The mixture was heated in an oil bath at 110 °C. When it was observed that insoluble substances were formed during the reaction, the process was stopped after 16 hours. The mixture was cooled to room temperature and transferred into 50 mL cold methanol, to which 5 mg of palladium scavenger was added and stirred for 1 hour. The obtained product was collected by filtration and dried with an air flow. Then, using a Soxhlet apparatus, the polymer was purified with solvents such as methanol, acetone, hexane, and chloroform. The chloroform fraction was collected under reduced pressure, and then the solid was isolated by precipitation with methanol (180 mg, 81.81% yield).

3.5.3 Synthesis Pathway of P5

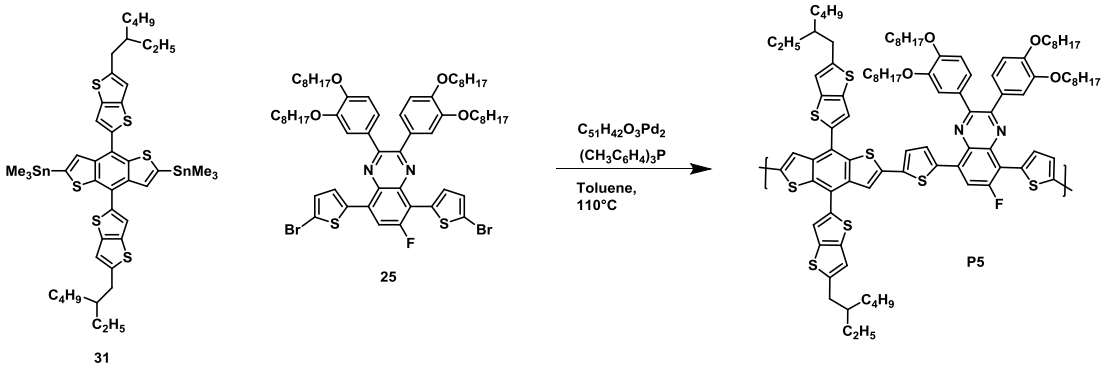


Figure 3.7. Synthesis Pathway of P5

100 mg of **Molecule 25** (88.09 μmol) and 89.56 mg of **Molecule 31** (88.09 μmol) were taken into a 20 mL Schlenk tube and kept under vacuum for half an hour. Then, the tube was filled with nitrogen atmosphere, and 8 mL of anhydrous toluene was added. Immediately afterwards, 3.22 mg (10.57 μmol) $(CH_3C_6H_4)_3P$ and 4.03 mg (4.40 μmol) $C_{51}H_{42}O_3Pd_2$ were rapidly added. The mixture was heated in an oil bath at 110 °C. When it was observed that insoluble substances were formed during the reaction, the process was stopped after 3 hours. The mixture was cooled to room temperature and transferred into 50 mL cold methanol, to which 5 mg of palladium scavenger was added and stirred for 1 hour. The obtained product was collected by filtration and dried with an air flow. Then, using a Soxhlet apparatus, the polymer was purified with solvents such as methanol, acetone, hexane, and chloroform. The chloroform fraction was collected under reduced pressure, and then the solid was isolated by precipitation with methanol (120 mg, 80% yield).

3.5.4 Synthesis Pathway of P2

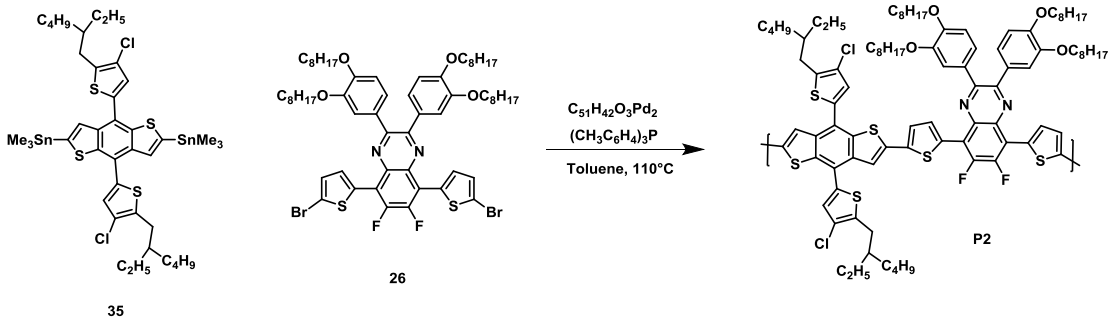


Figure 3.8. Synthesis pathway of P2

95.50 mg of **Molecule 26** (82.81 μmol) and 80.61 mg of **Molecule 35** (82.81 μmol) were taken into a 20 mL Schlenk tube and kept under vacuum for half an hour. Then, the tube was filled with nitrogen atmosphere, and 8 mL of anhydrous toluene was added. Immediately afterwards, 3.02 mg (9.94 μmol) $(CH_3C_6H_4)_3P$ and 3.79 mg (4.14 μmol) $C_{51}H_{42}O_3Pd_2$ were rapidly added. The mixture was heated in an oil bath at 110 °C. When it was observed that insoluble substances were formed during the reaction, the process was stopped after 9 hours. The mixture was cooled to room temperature and transferred into 50 mL cold methanol, to which 5 mg of palladium scavenger was added and stirred for 1 hour. The obtained product was collected by filtration and dried with an air flow. Then, using a Soxhlet apparatus, the polymer was purified with solvents such as methanol, acetone, hexane, and chloroform. The chloroform fraction was collected under reduced pressure, and then the solid was isolated by precipitation with methanol (90 mg, 64.28% yield).

3.5.5 Synthesis Pathway of P4

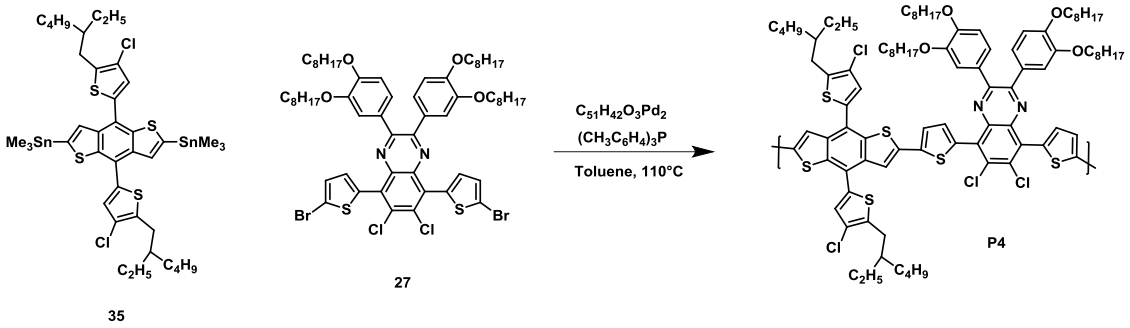


Figure 3.9. Synthesis Pathway of P4

97.50 mg of **Molecule 27** (82.20 μmol) and 80.02 mg of **Molecule 35** (82.20 μmol) were taken into a 20 mL Schlenk tube and kept under vacuum for half an hour. Then, the tube was filled with nitrogen atmosphere, and 8 mL of anhydrous toluene was added. Immediately afterwards, 3.0 mg (9.86 μmol) $(CH_3C_6H_4)_3P$ and 3.76 mg (4.11 μmol) $C_{51}H_{42}O_3Pd_2$ were rapidly added. The mixture was heated in an oil bath at 110 °C. When it was observed that insoluble substances were formed during the reaction, the process was stopped after 6 hours. The mixture was cooled to room temperature and transferred into 50 mL cold methanol, to which 5 mg of palladium scavenger was added and stirred for 1 hour. The obtained product was collected by filtration and dried with an air flow. Then, using a Soxhlet apparatus, the polymer was purified with solvents such as methanol, acetone, hexane, and chloroform. The chloroform fraction was collected under reduced pressure, and then the solid was isolated by precipitation with methanol (70 mg, 50% yield).

3.5.6 Synthesis Pathway of P6

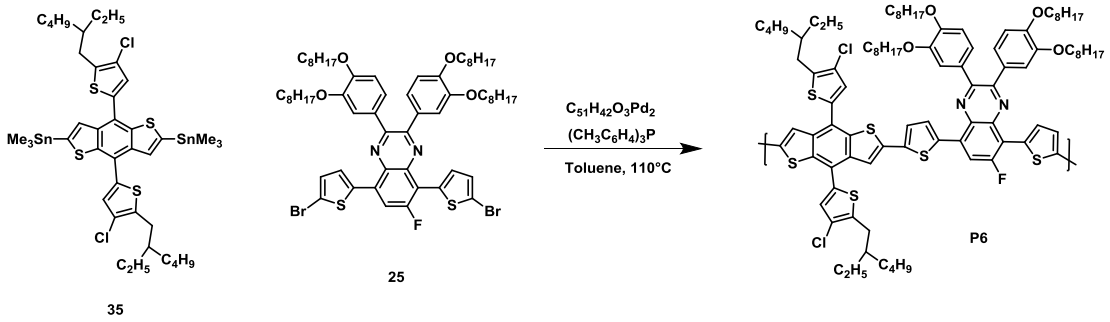


Figure 3.10. Synthesis pathway of P6

97.50 mg of **Molecule 25** (85.89 μmol) and 83.61 mg of **Molecule 35** (85.89 μmol) were taken into a 20 mL Schlenk tube and kept under vacuum for half an hour. Then, the tube was filled with nitrogen atmosphere, and 8 mL of anhydrous toluene was added. Immediately afterwards, 3.14 mg (10.31 μmol) $(CH_3C_6H_4)_3P$ and 3.93 mg (4.29 μmol) $C_{51}H_{42}O_3Pd_2$ were rapidly added. The mixture was heated in an oil bath at 110 °C. When it was observed that insoluble substances were formed during the reaction, the process was stopped after 1.5 hours. The mixture was cooled to room temperature and transferred into 50 mL cold methanol, to which 5 mg of palladium scavenger was added and stirred for 1 hour. The obtained product was collected by filtration and dried with an air flow. Then, using a Soxhlet apparatus, the polymer was purified with solvents such as methanol, acetone, hexane, and chloroform. The chloroform fraction was collected under reduced pressure, and then the solid was isolated by precipitation with methanol (120 mg, 85.50% yield).

CHAPTER 4

CONCLUSIONS

In conclusion a total of six novel conjugated polymers were synthesized by the Stille cross-coupling reaction aiming to investigate their potential in organic solar cell applications. These polymers were named **P1**, **P2**, **P3**, **P4**, **P5** and **P6** and were developed for use in organic solar cell applications. Polymerization was performed using two different donor structures, one of which was commercially available and the other synthesized, and three types of acceptor monomers. The average molecular weights (Mn) of the polymers were determined as 6.5 kDa for **P1**, 4.1 kDa for **P2**, 16.7 kDa for **P3**, 137.7 kDa for **P4**, 6.4 kDa for **P5**, and 105.6 kDa for **P6**, respectively. These reasults indicating variability in polymer chain length depending on the monomer combination and synthetic conditions. All synthesized polymers showed high light absorption ability in the visible spectrum region confirming their potential as active layer materials in OSCs, and the optical band gap values calculated based on UV-Vis thin film data were determined as 1.75, 1.81, 1.96, 1.98, 1.74, 1.72 eV for **P1**, **P2**, **P3**, **P4**, **P5**, **P6**, respectively.

Electrochemical characterizations were carried out by differential pulse voltammetry (DPV) technique and the HOMO and LUMO energy levels were determined as -5.623/-3.860, -5.782/-3.875, -5.718/-3.875, -6.264/-3.844, -5.670/-3.842, -5.690/-3.814 for **P1**, **P2**, **P3**, **P4**, **P5**, **P6**, respectively. These results revealed that HOMO/LUMO levels well aligned with typical non-fullerene acceptors such as Y6. Within the scope of this study, the main target of lowering the HOMO and LUMO levels was successfully achieved and the energy levels of the polymers showed suitability for OSC applications. Organic solar cells were fabricated using these polymers as donor materials, blended with Y6 and ITIC-Th as the acceptors. Among them, the **P2**-based device exhibited the highest power conversion efficiency of 8.16% at a 1:1.2 donor-to-acceptor ratio, demonstrating the strong potential of

difluorinated quinoxaline paired with a chlorine-substituted BDT. The performance order of other devices followed as: P1:Y6 (5.99%), P3:Y6 (1.48%), P5:Y6 (4.84%), and P6:Y6 (7.02%). These variations in PCE can be attributed to differences in energy level alignment, absorption properties, and molecular weight, all of which influence morphology and charge dynamics in the active layer.

Further improvement of the performance of such devices is possible with advanced optimization studies. Especially for more efficient charge separation and transfer processes, the use of ternary systems where $PC_{7\ 1}$ BM and Y6 are used together to form a cascade-like structure at energy levels or fullerene-free new generation acceptors with HOMO levels lower than Y6 are recommended.

REFERENCES

Aderne, R. E., Borges, B. G. A. L., Ávila, H. C., Von Kieseritzky, F., Hellberg, J., Koehler, M., Cremona, M., Roman, L. S., Araujo, C. M., Rocco, M. L. M., & Marchiori, C. F. N. (2022). On the energy gap determination of organic optoelectronic materials: The case of porphyrin derivatives. *Materials Advances*, *3*(3), 1791–1803. https://doi.org/10.1039/d1ma00652e

Alfano, A. I., Barone, S., & Brindisi, M. (2025). Flow Chemistry for Flowing Cross-Couplings: A Concise Overview. *Organic Process Research and Development*. https://doi.org/10.1021/acs.oprd.4c00457

An, C., & Hou, J. (2022). Benzo[1,2-b:4,5-b′]dithiophene-Based Conjugated Polymers for Highly Efficient Organic Photovoltaics. *Accounts of Materials Research*, *3*(5), 540–551. https://doi.org/10.1021/accountsmr.2c00020

Andrea, M., Kordos, K., Lidorikis, E., & Papageorgiou, D. (2022). Fluorination and chlorination effects on the charge transport properties of the IDIC non-fullerene acceptor: an ab-initio investigation. *EPJ Photovoltaics*, *13*. https://doi.org/10.1051/epjpv/2022012

Bao, Z., Chan, W., & Yu, L. (1993). Synthesis of Conjugated Polymer by the Stille Coupling Reaction. *Chemistry of Materials*, *5*(1), 2–3. https://doi.org/10.1021/cm00025a001

Baran, D., Balan, A., Celebi, S., Meana Esteban, B., Neugebauer, H., Sariciftci, N. S., & Toppare, L. (2010). Processable multipurpose conjugated polymer for electrochromic and photovoltaic applications. *Chemistry of Materials*, *22*(9), 2978–2987. https://doi.org/10.1021/cm100372t

Benanti, T. L., & Venkataraman, D. (2006). Organic solar cells: An overview focusing on active layer morphology. *Photosynthesis Research*, *87*(1), 73–81. https://doi.org/10.1007/s11120-005-6397-9

Braga, A. A. C., Ujaque, G., & Maseras, F. (2013). *Computational Perspective on*

Pd-Catalyzed. *46*(11). https://doi.org/10.1021/ar400080r

Bruno, A., Reynolds, L. X., Dyer-Smith, C., Nelson, J., & Haque, S. A. (2013). Determining the exciton diffusion length in a polyfluorene from ultrafast fluorescence measurements of polymer/fullerene blend films. *Journal of Physical Chemistry C*, *117*(39), 19832–19838. https://doi.org/10.1021/jp404985q

Centre, O. (2012). Encyclopedia of Sustainability Science and Technology. In *Encyclopedia of Sustainability Science and Technology*. https://doi.org/10.1007/978-1-4419-0851-3

Chao, P., Chen, H., Pu, M., Zhu, Y., Han, L., Zheng, N., Zhou, J., Chang, X., Mo, D., Xie, Z., Meng, H., & He, F. (2021). Chlorinated Benzo[1,2-b:4,5-c′]dithiophene-4,8-dione Polymer Donor: A Small Atom Makes a Big Difference. *Advanced Science*, *8*(4), 1–10. https://doi.org/10.1002/advs.202003641

Chemical, A. (1979). *Aryl Utility*. *eq 1*, 4992–4998.

Chen, Z., Ge, J., Guo, Y., Zhao, M., Shi, J., Qiu, Y., Zhou, E., & Ge, Z. (2022). Modification on the Quinoxaline Unit to Achieve High Open-Circuit Voltage and Morphology Optimization for Organic Solar Cells. *ACS Energy Letters*, *7*(10), 3432–3438. https://doi.org/10.1021/acsenergylett.2c01589

Cheng, Y. J., Yang, S. H., & Hsu, C. S. (2009). Synthesis of conjugated polymers for organic solar cell applications. *Chemical Reviews*, *109*(11), 5868–5923. https://doi.org/10.1021/cr900182s

Chi, D., Qu, S., Wang, Z., & Wang, J. (2014). High efficiency P3HT:PCBM solar cells with an inserted PCBM layer. *Journal of Materials Chemistry C*, *2*(22), 4383–4387. https://doi.org/10.1039/c4tc00003j

Clarke, T. M., & Durrant, J. R. (2010). Charge photogeneration in organic solar cells. *Chemical Reviews*, *110*(11), 6736–6767. https://doi.org/10.1021/cr900271s

Collins, S. D., Ran, N. A., Heiber, M. C., & Nguyen, T. Q. (2017). Small is Powerful: Recent Progress in Solution-Processed Small Molecule Solar Cells. *Advanced Energy Materials*, *7*(10). https://doi.org/10.1002/aenm.201602242

Dai, Q., Lang, X., Brédas, J.-L., Wang, T., & Jiang, Q. (2024). Impact of the alkyl side-chain length on solubility, interchain packing, and charge-transport properties of amorphous π-conjugated polymers. *Moore and More*, *1*(1), 1–10. https://doi.org/10.1007/s44275-024-00008-x

Dongaonkar, S., Servaites, J. D., Ford, G. M., Loser, S., Moore, J., Gelfand, R. M., Mohseni, H., Hillhouse, H. W., Agrawal, R., Ratner, M. A., Marks, T. J., Lundstrom, M. S., & Alam, M. A. (2010). Universality of non-Ohmic shunt leakage in thin-film solar cells. *Journal of Applied Physics*, *108*(12). https://doi.org/10.1063/1.3518509

Espinet, P., & Echavarren, A. M. (2004). The mechanisms of the Stille reaction. *Angewandte Chemie - International Edition*, *43*(36), 4704–4734. https://doi.org/10.1002/anie.200300638

Feldman, D. (2008). Polymer history. *Designed Monomers and Polymers*, *11*(1), 1–15. https://doi.org/10.1163/156855508X292383

Fu, Y., Cha, H., Song, S., Lee, G. Y., Eon Park, C., & Park, T. (2013). Low-bandgap quinoxaline-based D - A-type copolymers: Synthesis, characterization, and photovoltaic properties. *Journal of Polymer Science, Part A: Polymer Chemistry*, *51*(2), 372–382. https://doi.org/10.1002/pola.26395

G. Yu,* J. Gao, J. C. Hummelen, F. Wudi, A. J. H. (1995). Internal Donor-Acceptor. *Science*, *270*, 1–3. http://science.sciencemag.org/

Garcia Romero, D., Di Mario, L., Portale, G., & Loi, M. A. (2021). Crystallization driven boost in fill factor and stability in additive-free organic solar cells. *Journal of Materials Chemistry A*, *9*(42), 23783–23792. https://doi.org/10.1039/d1ta08232a

Gedefaw, D., Tessarolo, M., Bolognesi, M., Prosa, M., Kroon, R., Zhuang, W., Henriksson, P., Bini, K., Wang, E., Muccini, M., Seri, M., & Andersson, M. R. (2016). Synthesis and characterization of benzodithiophene and benzotriazole-based polymers for photovoltaic applications. *Beilstein Journal of Organic Chemistry*, *12*, 1629–1637. https://doi.org/10.3762/bjoc.12.160

Gedefaw, D., Tessarolo, M., Zhuang, W., Kroon, R., Wang, E., Bolognesi, M., Seri, M., Muccini, M., & Andersson, M. R. (2014). Conjugated polymers based on benzodithiophene and fluorinated quinoxaline for bulk heterojunction solar cells: Thiophene versus thieno[3,2-b]thiophene as π-conjugated spacers. *Polymer Chemistry*, *5*(6), 2083–2093. https://doi.org/10.1039/c3py01519j

Guo, S., Hu, Y., Qin, M., Li, J., Wang, Y., Qin, J., & Cheng, P. (2022). Toward high-performance organic photovoltaics: the new cooperation of sequential solution-processing and promising non-fullerene acceptors. *Materials Horizons*, *9*(8), 2097–2108. https://doi.org/10.1039/d2mh00376g

Harun, M. H., Saion, E., Kassim, A., Yahya, N., & Mahmud, E. (2007). Conjugated Conducting Polymers : A Brief Overview. *Sensors Peterborough NH*, *2*(May 2016), 63–68. http://sedaya.edu.my/jasa/2/papers/08I.pdf

Hasegawa, T., Ashizawa, M., Kawauchi, S., Masunaga, H., Ohta, N., & Matsumoto, H. (2019). Fluorination and chlorination effects on quinoxalineimides as an electron-deficient building block for n-channel organic semiconductors. *RSC Advances*, *9*(19), 10807–10813. https://doi.org/10.1039/c9ra02413a

Helgesen, M., Søndergaard, R., & Krebs, F. C. (2010). Advanced materials and processes for polymer solar cell devices. *Journal of Materials Chemistry*, *20*(1), 36–60. https://doi.org/10.1039/b913168j

Hoppe, H., & Sariciftci, N. S. (2004). Organic solar cells: An overview. *Journal of Materials Research*, *19*(7), 1924–1945. https://doi.org/10.1557/JMR.2004.0252

Hou, J., & Guo, X. (2013). Active Layer Materials for Organic Solar Cells. *Green Energy and Technology*, *128*(June), 17–42. https://doi.org/10.1007/978-1-4471-4823-4_2

Huo, L., Hou, J., Zhang, S., Chen, H. Y., & Yang, Y. (2010). A Poh benzo[1,2-6:4,5-b′]dithiophene derivative with deep HOMO level and its application in high-performance polymer solar cells. *Angewandte Chemie - International Edition*, *49*(8), 1500–1503. https://doi.org/10.1002/anie.200906934

Imran, M., Ikram, M., Dilpazir, S., Nafees, M., Ali, S., & Geng, J. (2017). Towards efficient and cost-effective inverted hybrid organic solar cells using inorganic semiconductor in the active layer. *Applied Nanoscience (Switzerland)*, *7*(8), 747–752. https://doi.org/10.1007/s13204-017-0618-3

Johansson Seechurn, C. C. C., Kitching, M. O., Colacot, T. J., & Snieckus, V. (2012). Palladium-catalyzed cross-coupling: A historical contextual perspective to the 2010 nobel prize. *Angewandte Chemie - International Edition*, *51*(21), 5062–5085. https://doi.org/10.1002/anie.201107017

Kesinro, R. O., Boyo, A. O., Akinyemi, M. L., Emetere, M. E., & Aizebeokhai, A. P. (2021). Progress on Organic Solar Cells: A Short Review. *IOP Conference Series: Earth and Environmental Science*, *665*(1). https://doi.org/10.1088/1755-1315/665/1/012036

Khandelwal, K., Shankar S, S., Malhotra, P., Biswas, S., Panghal, A., Roy, S. S., & Sharma, G. D. (2023). Unraveling the Impact of Thickness on Active Layer Morphology and Device Performance of Semitransparent Organic Solar Cells: A Comprehensive Study. *ACS Applied Energy Materials*, *6*(19), 10078–10087. https://doi.org/10.1021/acsaem.3c01685

Kim, J. H., Park, J. B., Jung, I. H., Yoon, S. C., Kwak, J., & Hwang, D. H. (2015). New alkylthio-thieno[3,2-b]thiophene-substituted benzodithiophene-based highly efficient photovoltaic polymer. *Journal of Materials Chemistry C*, *3*(17), 4250–4253. https://doi.org/10.1039/c5tc00627a

Kim, J. S., Granström, M., Friend, R. H., Johansson, N., Salaneck, W. R., Daik, R.,

Feast, W. J., & Cacialli, F. (1998). Indium-tin oxide treatments for single- and double-layer polymeric light-emitting diodes: The relation between the anode physical, chemical, and morphological properties and the device performance. *Journal of Applied Physics*, *84*(12), 6859–6870. https://doi.org/10.1063/1.368981

Kim, J. Y., Lee, K., Coates, N. E., Moses, D., Nguyen, T. Q., Dante, M., & Heeger, A. J. (2007). Efficient tandem polymer solar cells fabricated by all-solution processing. *Science*, *317*(5835), 222–225. https://doi.org/10.1126/science.1141711

Kim, M. S., Kim, B. G., & Kim, J. (2009). Effective variables to control the fill factor of organic photovoltaic cells. *ACS Applied Materials and Interfaces*, *1*(6), 1264–1269. https://doi.org/10.1021/am900155y

Kim, W., Kim, J. K., Kim, E., Ahn, T. K., Wang, D. H., & Park, J. H. (2015). Conflicted effects of a solvent additive on PTB7:PC71BM bulk heterojunction solar cells. *Journal of Physical Chemistry C*, *119*(11), 5954–5961. https://doi.org/10.1021/jp510996w

Kim, Y., Choulis, S. A., Nelson, J., Bradley, D. D. C., Cook, S., & Durrant, J. R. (2005). Device annealing effect in organic solar cells with blends of regioregular poly(3-hexylthiophene) and soluble fullerene. *Applied Physics Letters*, *86*(6), 1–3. https://doi.org/10.1063/1.1861123

Klauk, H. (2006). Edited by Organic Light Emitting Devices One-Dimensional Metals Enabling Technologies for MEMS and Nanodevices Handbook of Machine Olfaction Nanotechnology. In *Organic Electronics*.

Lattante, S. (2014). Electron and hole transport layers: Their use in inverted bulk heterojunction polymer solar cells. *Electronics (Switzerland)*, *3*(1), 132–164. https://doi.org/10.3390/electronics3010132

Leclerc, N., Chávez, P., Ibraikulov, O. A., Heiser, T., & Lévêque, P. (2016). Impact of backbone fluorination on π-conjugated polymers in organic photovoltaic devices: A review. *Polymers*, *8*(1).

https://doi.org/10.3390/polym8010011

Lee, S. W., Hussain, M. W., Lee, J., Whang, D. R., Jeong, W. H., Choi, H., & Chang, D. W. (2023). Effect of Chlorine Substituents on the Photovoltaic Properties of Monocyanated Quinoxaline-Based D-A-Type Polymers. *ACS Applied Materials and Interfaces*, *15*(4), 5547–5555. https://doi.org/10.1021/acsami.2c19702

Lee, S. W., Shin, H. J., Park, B., Shome, S., Whang, D. R., Bae, H., Chung, S., Cho, K., Ko, S. J., Choi, H., & Chang, D. W. (2022). Effect of Electron-Withdrawing Chlorine Substituent on Morphological and Photovoltaic Properties of All Chlorinated D-A-Type Quinoxaline-Based Polymers. *ACS Applied Materials and Interfaces*, *14*(17), 19785–19794. https://doi.org/10.1021/acsami.2c00764

Lenaerts, R., Devisscher, D., Pirotte, G., Gielen, S., Mertens, S., Cardeynaels, T., Champagne, B., Lutsen, L., Vanderzande, D., Adriaensens, P., Verstappen, P., Vandewal, K., & Maes, W. (2020). The effect of halogenation on PBDTT-TQxT based non-fullerene polymer solar cells – Chlorination vs fluorination. *Dyes and Pigments*, *181*(March). https://doi.org/10.1016/j.dyepig.2020.108577

Li, H., Johansson Seechurn, C. C. C., & Colacot, T. J. (2012). Development of preformed Pd catalysts for cross-coupling reactions, beyond the 2010 nobel prize. *ACS Catalysis*, *2*(6), 1147–1164. https://doi.org/10.1021/cs300082f

Li, Y. (2012). Molecular design of photovoltaic materials for polymer solar cells: Toward suitable electronic energy levels and broad absorption. *Accounts of Chemical Research*, *45*(5), 723–733. https://doi.org/10.1021/ar2002446

Li, Y., Chang, C. Y., Chen, Y., Song, Y., Li, C. Z., Yip, H. L., Jen, A. K. Y., & Li, C. (2013). The effect of thieno[3,2-b]thiophene on the absorption, charge mobility and photovoltaic performance of diketopyrrolopyrrole-based low bandgap conjugated polymers. *Journal of Materials Chemistry C*, *1*(45), 7526–7533. https://doi.org/10.1039/c3tc31600a

Li, Z., Bian, J., Wang, Y., Jiang, F., Liang, G., He, P., Hou, Q., Tong, J., Liang, Y., Zhong, Z., Zhou, Y., & Tian, W. (2014). Effect of alkyl chain length on the photovoltaic performance of oligothiophene-based small molecules. *Solar Energy Materials and Solar Cells*, *130*, 336–346. https://doi.org/10.1016/j.solmat.2014.07.031

Li, Z., Song, D., Xu, Z., Qiao, B., Zhao, S., Wageh, S., Al-Ghamdi, A. A., & Huo, X. (2021). Synergetic effect of different carrier dynamics in Pm6: Y6: ITIC-M ternary cascade energy level system. *Polymers*, *13*(15), 1–13. https://doi.org/10.3390/polym13152398

Liang, Y., Feng, D., Wu, Y., Tsai, S. T., Li, G., Ray, C., & Yu, L. (2009). Highly efficient solar cell polymers developed via fine-tuning of structural and electronic properties. *Journal of the American Chemical Society*, *131*(22), 7792–7799. https://doi.org/10.1021/ja901545q

Lin, Y., Zhao, F., He, Q., Huo, L., Wu, Y., Parker, T. C., Ma, W., Sun, Y., Wang, C., Zhu, D., Heeger, A. J., Marder, S. R., & Zhan, X. (2016). High-Performance Electron Acceptor with Thienyl Side Chains for Organic Photovoltaics. *Journal of the American Chemical Society*, *138*(14), 4955–4961. https://doi.org/10.1021/jacs.6b02004

Liu, B., Wang, S., Bazan, G. C., & Mikhailovsky, A. (2003). *Shape-Adaptable Water-Soluble Conjugated Polymers*. 13306–13307.

Liu, M., Gao, Y., Zhang, Y., Liu, Z., & Zhao, L. (2017). Quinoxaline-based conjugated polymers for polymer solar cells. *Polymer Chemistry*, *8*(32), 4613–4636. https://doi.org/10.1039/c7py00850c

Liu, X., Zhang, X., Sheng, Y., Zhang, Z., Xiong, P., Ju, X., Zhu, J., & Ye, C. (2025). Advancing organic photovoltaic materials by machine learning-driven design with polymer-unit fingerprints. *Npj Computational Materials*, *11*(1), 1–14. https://doi.org/10.1038/s41524-025-01608-3

Lu, L., Zheng, T., Wu, Q., Schneider, A. M., Zhao, D., & Yu, L. (2015). Recent Advances in Bulk Heterojunction Polymer Solar Cells. *Chemical Reviews*,

115(23), 12666–12731. https://doi.org/10.1021/acs.chemrev.5b00098

Luo, J., Wang, L., Ye, L., & Tan, S. (2025). Synthesis and photovoltaic properties of the efficient polymer donor based on benzo[1,2-b:4,5-b']difuran unit. *European Polymer Journal*, *226*(December 2024), 113766. https://doi.org/10.1016/j.eurpolymj.2025.113766

Moore, J. S. (2008). Molecular design of thin film optoelectronic materials for solar cells. *Journal of the American Chemical Society*, *130*(37), 12201–12203. https://doi.org/10.1021/ja806392t

Moustafa, E., Méndez, M., Pallarès, J., & Marsal, L. F. (2022). Low temperature based PDINO cathode interlayer for high operational photostable inverted non-fullerene organic solar cells. *Solar Energy Materials and Solar Cells*, *248*(January). https://doi.org/10.1016/j.solmat.2022.111985

Mozhzhukhina, N., Longinotti, M. P., Corti, H. R., & Calvo, E. J. (2015). A conductivity study of preferential solvation of lithium ion in acetonitrile-dimethyl sulfoxide mixtures. *Electrochimica Acta*, *154*, 456–461. https://doi.org/10.1016/j.electacta.2014.12.022

Nakano, K., Chen, Y., Xiao, B., Han, W., Huang, J., Yoshida, H., Zhou, E., & Tajima, K. (2019). Anatomy of the energetic driving force for charge generation in organic solar cells. *Nature Communications*, *10*(1), 1–10. https://doi.org/10.1038/s41467-019-10434-3

Nguyen, T. P. (2022). Graphene-based polymer composites for photocatalytic applications. In *Innovations in Graphene-Based Polymer Composites*. Elsevier Ltd. https://doi.org/10.1016/B978-0-12-823789-2.00008-X

Nicolaou, K. C., Bulger, P. G., & Sarlah, D. (2005). Palladium-catalyzed cross-coupling reactions in total synthesis. *Angewandte Chemie - International Edition*, *44*(29), 4442–4489. https://doi.org/10.1002/anie.200500368

Nithya, K. S., & Sudheer, K. S. (2020). Device modelling of non-fullerene organic solar cell with inorganic CuI hole transport layer using SCAPS 1-D. *Optik*,

217(February), 164790. https://doi.org/10.1016/j.ijleo.2020.164790

Nova, A., Ujaque, G., Maseras, F., Lledós, A., & Espinet, P. (2006). A critical analysis of the cyclic and open alternatives of the transmetalation step in the stille cross-coupling reaction. *Journal of the American Chemical Society*, *128*(45), 14571–14578. https://doi.org/10.1021/ja0635736

Page, Z. A., Liu, Y., Duzhko, V. V., Russell, T. P., & Emrick, T. (2014). Fulleropyrrolidine interlayers: Tailoring electrodes to raise organic solar cell efficiency. *Science*, *346*(6208), 441–444. https://doi.org/10.1126/science.1255826

Pagliaro, M., Pandarus, V., Ciriminna, R., Béland, F., & DemmaCarà, P. (2012). Heterogeneous versus Homogeneous Palladium Catalysts for Cross-Coupling Reactions. *ChemCatChem*, *4*(4), 432–445. https://doi.org/10.1002/cctc.201100422

Patil, S. V., Shelake, S. S., & Patil, S. S. (2018). Polymeric materials for targeted delivery of bioactive agents and drugs. In *Fundamental Biomaterials: Polymers*. Elsevier Ltd. https://doi.org/10.1016/B978-0-08-102194-1.00011-6

Peng, L. (2018). *Study of the effect of DIO additive on charge extraction and recombination in organic–inorganic hybrid MAPbI3 xClx perovskite solar cell*. 40298–40307. https://doi.org/10.1039/c8ra08563c

Peng, Q., Liu, X., Su, D., Fu, G., Xu, J., & Dai, L. (2011). Novel benzo[1,2-b:4,5-b′]dithiophene-benzothiadiazole derivatives with variable side chains for high-performance solar cells. *Advanced Materials*, *23*(39), 4554–4558. https://doi.org/10.1002/adma.201101933

Petrus, M. L. (2014). *Azomethine-based Donor Materials for Organic Solar Cells*. 175.

Qi, B., & Wang, J. (2013). Fill factor in organic solar cells. *Physical Chemistry Chemical Physics*, *15*(23), 8972–8982. https://doi.org/10.1039/c3cp51383a

Revoju, S. (2018). *Molecular Design , Synthesis and Performance Evaluation of*

Phenothiazine-based Small Molecules for Organic Solar Cells (Issue February). https://doi.org/10.13140/RG.2.2.27203.50728

Riede, M., Spoltore, D., & Leo, K. (2021). Organic Solar Cells—The Path to Commercial Success. *Advanced Energy Materials*, *11*(1), 1–10. https://doi.org/10.1002/aenm.202002653

Sajjad, M. T., Ruseckas, A., & Samuel, I. D. W. (2020). Enhancing Exciton Diffusion Length Provides New Opportunities for Organic Photovoltaics. *Matter*, *3*(2), 341–354. https://doi.org/10.1016/j.matt.2020.06.028

Salih, K. S. M., & Baqi, Y. (2020). Microwave-assisted palladium-catalyzed cross-coupling reactions: Generation of carbon–carbon bond. *Catalysts*, *10*(1), 1–35. https://doi.org/10.3390/catal10010004

Scharber, M. C., & Sariciftci, N. S. (2013). Efficiency of bulk-heterojunction organic solar cells. *Progress in Polymer Science*, *38*(12), 1929–1940. https://doi.org/10.1016/j.progpolymsci.2013.05.001

Schroeder, B. C., Ashraf, R. S., & Mcculloch, I. (2014). Thiophene-Based High-Performance Donor Polymers for Organic Solar Cells. *Wiley Blackwell 6*, *9783527332*, 27–60. https://doi.org/10.1002/9783527656912.ch02

Shirakawa, H., Louis, E. J., MacDiarmid, A. G., Chiang, C. K., & Heeger, A. J. (1977). Synthesis of electrically conducting organic polymers: Halogen derivatives of polyacetylene, (CH)x. *Journal of the Chemical Society, Chemical Communications*, *16*, 578–580. https://doi.org/10.1039/C39770000578

Suzuki, A., & Miyaura, N. (1995). Palladium-Catalyzed Cross-Coupling Reactions of Organoboron Compounds. *Chemical Reviews*, *95*(7), 2457–2483.

Tang, C. W. (1986). Two-layer organic photovoltaic cell. *Applied Physics Letters*, *48*(2), 183–185. https://doi.org/10.1063/1.96937

Taskaya Aslan, S., Demir Arabacı, E., Karakurt, O., Cevher, D., Alemdar Yılmaz, E., Yalvac, D., Yıldız, D. E., & Cirpan, A. (2025). Impact of different

aromatic side units on benzodithiophene on the optical, electronic, and photovoltaic properties for organic solar cell applications. *Synthetic Metals*, *313*(March), 117890. https://doi.org/10.1016/j.synthmet.2025.117890

Tvrdy, K., & Kamat, P. V. (2011). Quantum Dot Solar Cells. *Comprehensive Nanoscience and Technology*, *1–5*, 257–275. https://doi.org/10.1016/B978-0-12-374396-1.00129-X

Venton, B. J., & Discenza, D. J. (2020). Electrochemistry for Bioanalysis. *Electrochemistry for Bioanalysis*. https://doi.org/10.1016/c2019-0-03108-1

Verploegen, E., Mondal, R., Bettinger, C. J., Sok, S., Toney, M. F., & Bao, Z. (2010). Effects of thermal annealing upon the morphology of polymer-fullerene blends. *Advanced Functional Materials*, *20*(20), 3519–3529. https://doi.org/10.1002/adfm.201000975

Wang, C., Fang, J., Guan, C., Hu, Z., Wu, T., Xiao, C., & Li, W. (2023). *Polymer Chemistry conjugated polymers on the photovoltaic*. 616–622. https://doi.org/10.1039/d2py01473d

Wang, D., Ding, W., Geng, Z., Wang, L., Geng, Y., Su, Z., & Yu, H. (2014). Rational design and characterization of high-efficiency planar A-π-D-π-A type electron donors in small molecule organic solar cells: A quantum chemical approach. *Materials Chemistry and Physics*, *145*(3), 387–396. https://doi.org/10.1016/j.matchemphys.2014.02.027

Wilken, S., Scheunemann, D., Dahlström, S., Nyman, M., Parisi, J., & Österbacka, R. (2021). How to Reduce Charge Recombination in Organic Solar Cells: There are Still Lessons to Learn from P3HT:PCBM. *Advanced Electronic Materials*, *7*(5). https://doi.org/10.1002/aelm.202001056

Wohrle, B. D., & Meissner, D. (1991). *Organic Solar Cells **. 3*, 129–138.

Wu, J., Gao, M., Chai, Y., Liu, P., Zhang, B., Liu, J., & Ye, L. (2021). Towards a bright future: The versatile applications of organic solar cells. *Materials Reports: Energy*, *1*(4), 100062. https://doi.org/10.1016/j.matre.2021.100062

Wu, Q., Ding, S., Sun, A., & Xia, Y. (2024). Recent progress on non-fullerene acceptor materials for organic solar cells. *Materials Today Chemistry*, *41*(August), 102290. https://doi.org/10.1016/j.mtchem.2024.102290

Wu, R., Yin, L., & Li, Y. (2016). π-Linkage effect of push-pull-structure organic small molecules for photovoltaic application. *Science China Materials*, *59*(5), 371–388. https://doi.org/10.1007/s40843-016-5050-7

Würthner, F., Saha-Möller, C. R., Fimmel, B., Ogi, S., Leowanawat, P., & Schmidt, D. (2016). Perylene Bisimide Dye Assemblies as Archetype Functional Supramolecular Materials. *Chemical Reviews*, *116*(3), 962–1052. https://doi.org/10.1021/acs.chemrev.5b00188

Wypych, G. (2024). Adhesives And Sealants. *Handbook of Solvents, Volume 2: Use, Health, and Environment*, 987–1257. https://doi.org/10.1016/B978-1-77467-042-2.50004-0

Xie, D. X., Liu, T. C., Xiao, J., Fang, J. K., Pan, C. J., & Shao, G. (2021). Effect of side chain substituent volume on thermoelectric properties of IDT-Based conjugated polymers. *Molecules*, *26*(4). https://doi.org/10.3390/molecules26040963

Xu, S., Wang, X., Feng, L., He, Z., Peng, H., Cimrová, V., Yuan, J., Zhang, Z. G., Li, Y., & Zou, Y. (2018). Optimizing the conjugated side chains of quinoxaline based polymers for nonfullerene solar cells with 10.5% efficiency. *Journal of Materials Chemistry A*, *6*(7), 3074–3083. https://doi.org/10.1039/c7ta10262c

Xu, Y., Wang, J., Yao, H., Bi, P., Zhang, T., Xu, J., & Hou, J. (2023). An Asymmetric Non-fullerene Acceptor with Low Energy Loss and High Photovoltaic Efficiency. *Chinese Journal of Chemistry*, *41*(9), 1045–1050. https://doi.org/10.1002/cjoc.202200662

Xu, Z., Park, K. S., Kwok, J. J., Lin, O., Patel, B. B., Kafle, P., Davies, D. W., Chen, Q., & Diao, Y. (2022). Not All Aggregates Are Made the Same: Distinct Structures of Solution Aggregates Drastically Modulate Assembly

Pathways, Morphology, and Electronic Properties of Conjugated Polymers. *Advanced Materials*, *34*(32). https://doi.org/10.1002/adma.202203055

Yadav, P. K., Kumar, S., & Maiti, P. (2022). Conjugated polymers for solar cell applications. In *Conjugated Polymers for Next-Generation Applications, Volume 2: Energy Storage Devices* (Vol. 2). LTD. https://doi.org/10.1016/B978-0-12-824094-6.00004-2

Yan, J., & Saunders, B. R. (2014). Third-generation solar cells: A review and comparison of polymer:fullerene, hybrid polymer and perovskite solar cells. *RSC Advances*, *4*(82), 43286–43314. https://doi.org/10.1039/c4ra07064j

Yang, D., Yang, R., Priya, S., & Liu, S. (Frank). (2019). Recent Advances in Flexible Perovskite Solar Cells: Fabrication and Applications. *Angewandte Chemie - International Edition*, *58*(14), 4466–4483. https://doi.org/10.1002/anie.201809781

Yang, P., Yuan, M., Zeigler, D. F., Watkins, S. E., Lee, J. A., & Luscombe, C. K. (2014). Influence of fluorine substituents on the film dielectric constant and open-circuit voltage in organic photovoltaics. *Journal of Materials Chemistry C*, *2*(17), 3278–3284. https://doi.org/10.1039/c3tc32087a

Yao, H., Wang, J., Xu, Y., Zhang, S., & Hou, J. (2020). *Recent Progress in Chlorinated Organic Photovoltaic Materials*. https://doi.org/10.1021/acs.accounts.0c00009

Yao, H., Ye, L., Zhang, H., Li, S., Zhang, S., & Hou, J. (2016). Molecular design of benzodithiophene-based organic photovoltaic materials. *Chemical Reviews*, *116*(12), 7397–7457. https://doi.org/10.1021/acs.chemrev.6b00176

Yao, J., Qiu, B., Zhang, Z. G., Xue, L., Wang, R., Zhang, C., Chen, S., Zhou, Q., Sun, C., Yang, C., Xiao, M., Meng, L., & Li, Y. (2020). Cathode engineering with perylene-diimide interlayer enabling over 17% efficiency single-junction organic solar cells. *Nature Communications*, *11*(1), 1–10. https://doi.org/10.1038/s41467-020-16509-w

Ye, Q., & Chi, C. (2011). Conjugated Polymers for Organic Solar Cells. *Solar Cells - New Aspects and Solutions*. https://doi.org/10.5772/23275

Yeh, N., & Yeh, P. (2013). Organic solar cells: Their developments and potentials. *Renewable and Sustainable Energy Reviews*, *21*, 421–431. https://doi.org/10.1016/j.rser.2012.12.046

Yenel, E. (2022). The Effect of Coating Parameter of Active Layer on Performance of Polymer Solar Cells. *Celal Bayar Üniversitesi Fen Bilimleri Dergisi*, *18*(1), 85–89. https://doi.org/10.18466/cbayarfbe.992952

Yuan, J., Zhang, Y., Zhou, L., Zhang, G., Yip, H. L., Lau, T. K., Lu, X., Zhu, C., Peng, H., Johnson, P. A., Leclerc, M., Cao, Y., Ulanski, J., Li, Y., & Zou, Y. (2019). Single-Junction Organic Solar Cell with over 15% Efficiency Using Fused-Ring Acceptor with Electron-Deficient Core. *Joule*, *3*(4), 1140–1151. https://doi.org/10.1016/j.joule.2019.01.004

Zakaria, N. A., & Malik, S. A. (2023). The Influence of Spin Coating Speed on the Optical Properties of P3HT Thin Film. *Journal of Physics: Conference Series, 2582*(1). https://doi.org/10.1088/1742-6596/2582/1/012027

Zhang, M., Liu, Y., Zeng, M., Zhao, B., & Tan, S. (2023). Enhanced Photovoltaic Performances via Chlorine Substitution on Alkylphenyl Side Chains of a Conjugated Polymer. *Energy and Fuels*, *37*(3), 2387–2393. https://doi.org/10.1021/acs.energyfuels.2c03692

Zhang, Y., Gao, X., Li, J., & Tu, G. (2015). Highly selective palladium-catalyzed Stille coupling reaction toward chlorine-containing NIR electroluminescent polymers. *Journal of Materials Chemistry C*, *3*(28), 7463–7468. https://doi.org/10.1039/c5tc01013f

Zhang, Y., Yao, H., Zhang, S., Qin, Y., Zhang, J., Yang, L., Li, W., Wei, Z., Gao, F., & Hou, J. (2018). Fluorination vs. chlorination: a case study on high performance organic photovoltaic materials. *Science China Chemistry*, *61*(10), 1328–1337. https://doi.org/10.1007/s11426-018-9260-2

Zhao, F., Dai, S., Wu, Y., Zhang, Q., Wang, J., Jiang, L., Ling, Q., Wei, Z., Ma, W., You, W., Wang, C., & Zhan, X. (2017). Single-Junction Binary-Blend Nonfullerene Polymer Solar Cells with 12.1% Efficiency. *Advanced Materials*, *29*(18). https://doi.org/10.1002/adma.201700144

Zhao, Q., Qu, J., & He, F. (2020). Chlorination: An Effective Strategy for High-Performance Organic Solar Cells. *Advanced Science*, *7*(14), 1–25. https://doi.org/10.1002/advs.202000509

Zhao, W., Li, S., Yao, H., Zhang, S., Zhang, Y., Yang, B., & Hou, J. (2017). Molecular Optimization Enables over 13% Efficiency in Organic Solar Cells. *Journal of the American Chemical Society*, *139*(21), 7148–7151. https://doi.org/10.1021/jacs.7b02677

Zhao, W., Qian, D., Zhang, S., Li, S., Inganäs, O., Gao, F., & Hou, J. (2016). Fullerene-Free Polymer Solar Cells with over 11% Efficiency and Excellent Thermal Stability. *Advanced Materials*, *28*(23), 4734–4739. https://doi.org/10.1002/adma.201600281

Zhao, X., Cai, H., Deng, Y., Jiang, Y., Wang, Z., Shi, Y., Han, Y., & Geng, Y. (2021). Low-Band gap Conjugated Polymers with Strong Absorption in the Second Near-Infrared Region Based on Diketopyrrolopyrrole-Containing Quinoidal Units. *Macromolecules*, *54*(7), 3498–3506. https://doi.org/10.1021/acs.macromol.1c00124

Zhou, H., Yang, L., Stuart, A. C., Price, S. C., Liu, S., & You, W. (2011). Development of fluorinated benzothiadiazole as a structural unit for a polymer solar cell of 7% efficiency. *Angewandte Chemie - International Edition*, *50*(13), 2995–2998. https://doi.org/10.1002/anie.201005451

Zhou, H., Yang, L., & You, W. (2012). Rational design of high performance conjugated polymers for organic solar cells. *Macromolecules*, *45*(2), 607–632. https://doi.org/10.1021/ma201648t

Zhu, C., Meng, L., Zhang, J., Qin, S., Lai, W., Qiu, B., Yuan, J., Wan, Y., Huang, W., & Li, Y. (2021). A Quinoxaline-Based D–A Copolymer Donor Achieving

17.62% Efficiency of Organic Solar Cells. *Advanced Materials*, *33*(23), 1–9. https://doi.org/10.1002/adma.202100474

Zhu, L., Zhang, M., Zhou, G., Hao, T., Xu, J., Wang, J., Qiu, C., Prine, N., Ali, J., Feng, W., Gu, X., Ma, Z., Tang, Z., Zhu, H., Ying, L., Zhang, Y., & Liu, F. (2020). Efficient Organic Solar Cell with 16.88% Efficiency Enabled by Refined Acceptor Crystallization and Morphology with Improved Charge Transfer and Transport Properties. *Advanced Energy Materials*, *10*(18), 1–9. https://doi.org/10.1002/aenm.201904234

Zhu, Y., Zhao, F., Wang, W., Li, Y., Zhang, S., & Lin, Y. (2022). Exciton Binding Energy of Non-Fullerene Electron Acceptors. *Advanced Energy and Sustainability Research*, *3*(4). https://doi.org/10.1002/aesr.202100184

APPENDICES

A. Nuclear Magnetic Resonance

Each compound was analyzed using a Bruker Spectrospin Avance DPX-400 spectrometer.TMS and deuterated chloroform ($CDCl_3$) served as internal references during the measurements.

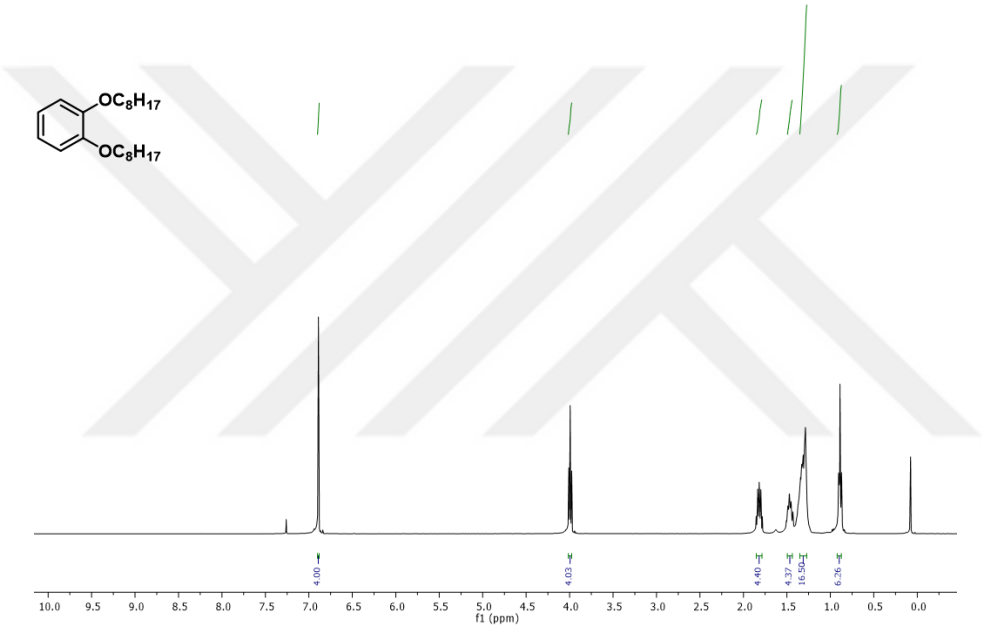


Figure A.1. ^1H NMR spectrum of **Molecule 2** in $CDCl_3$

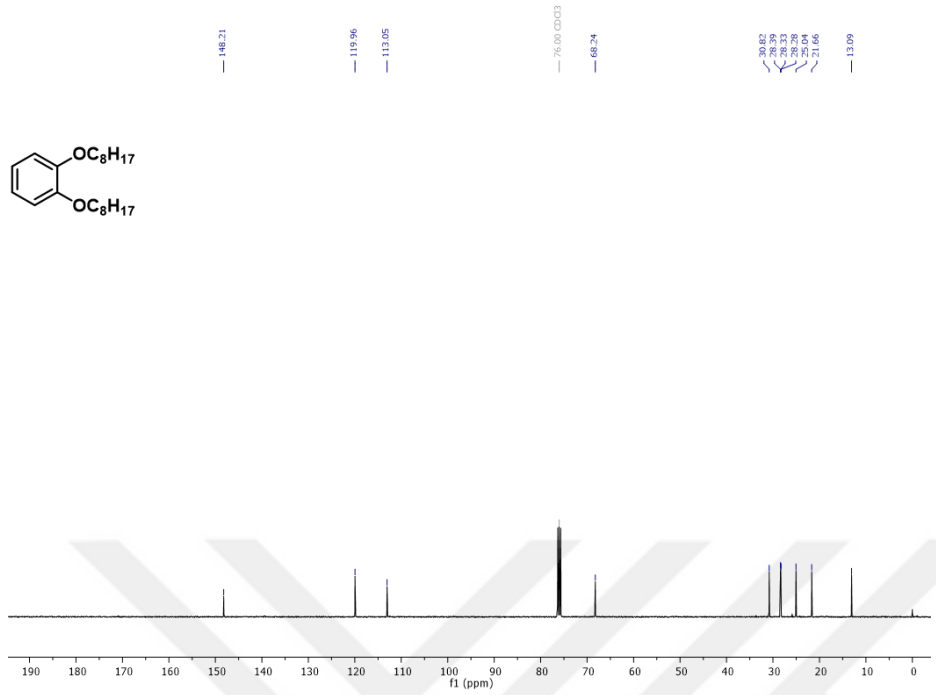


Figure A.2. ^{13}C NMR spectrum of **Molecule 2** in $CDCl_3$

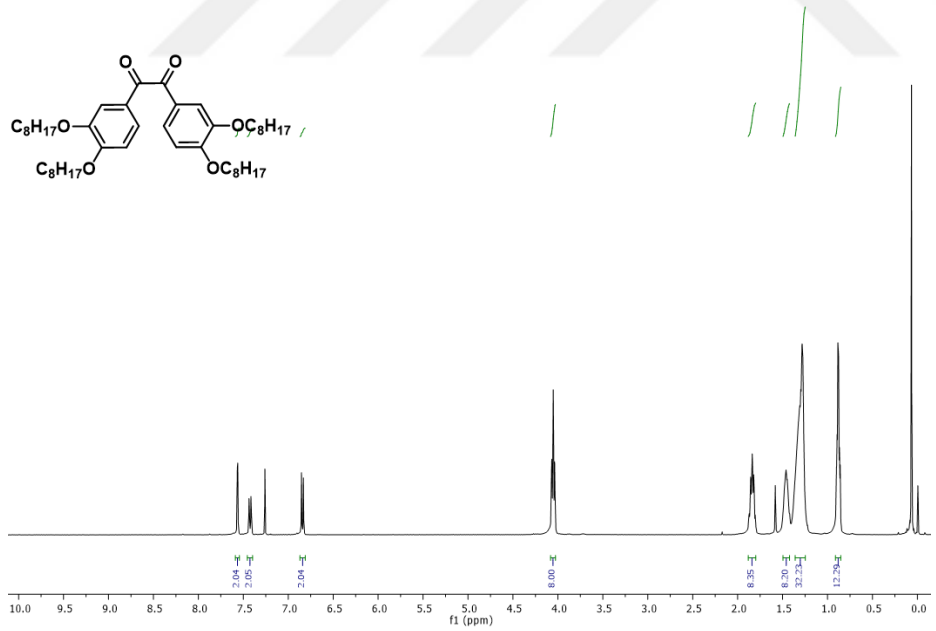


Figure A.3. ^{1}H NMR spectrum of **Molecule 3** in $CDCl_3$

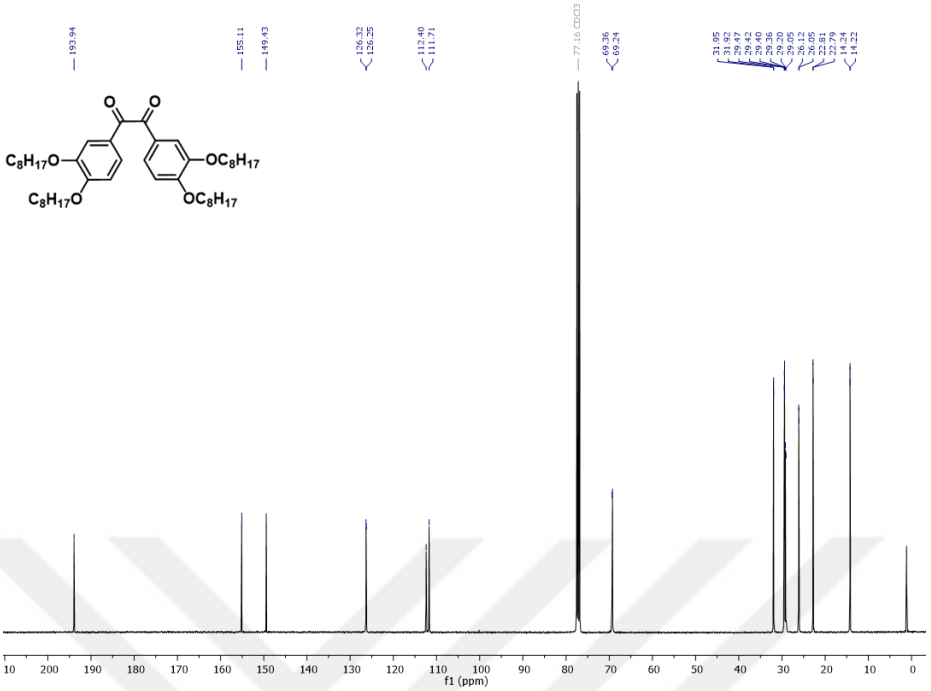


Figure A.4. ^{13}C NMR spectrum of **Molecule 3** in $CDCl_3$

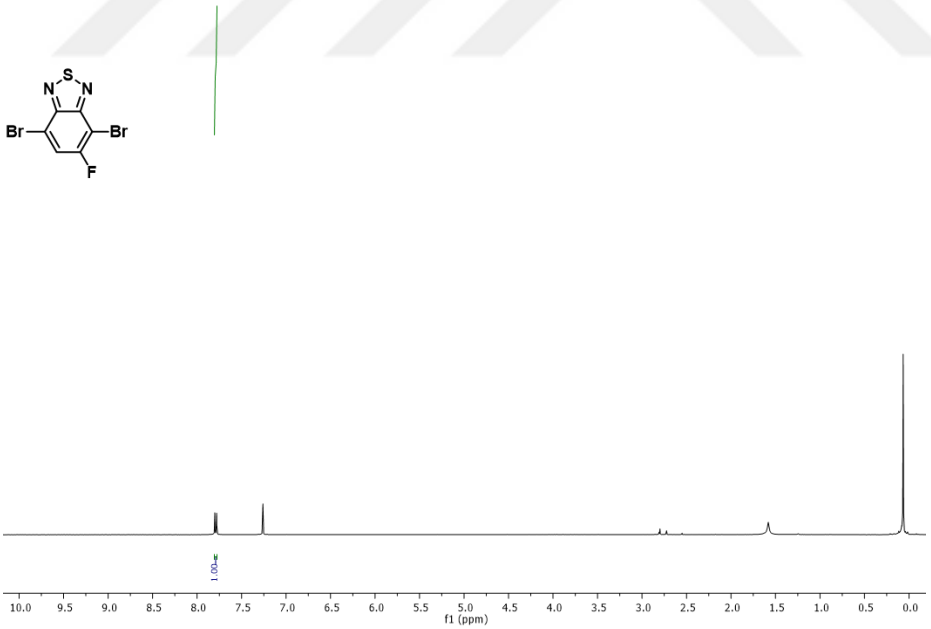


Figure A.5. ^{1}H NMR spectrum of **Molecule 13** in $CDCl_3$

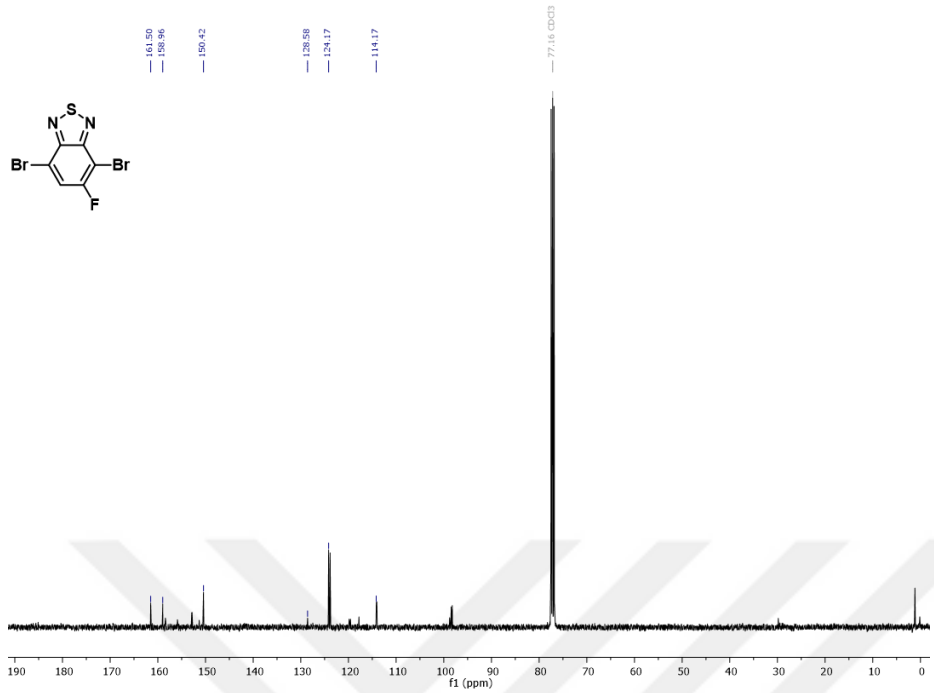


Figure A.6. ^{13}C NMR spectrum of **Molecule 13** in $CDCl_3$

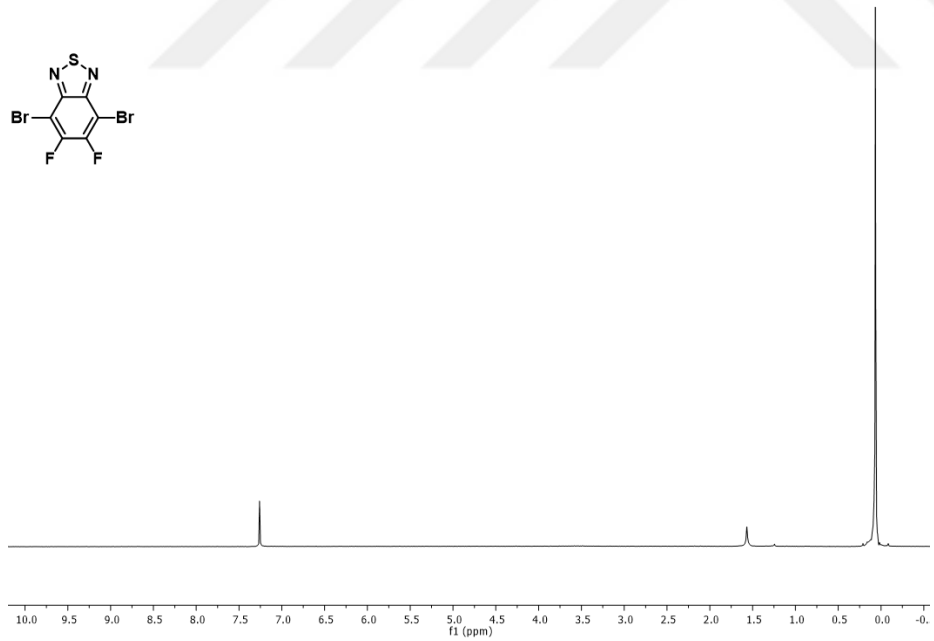


Figure A.7. ^{1}H NMR spectrum of **Molecule 14** in $CDCl_3$

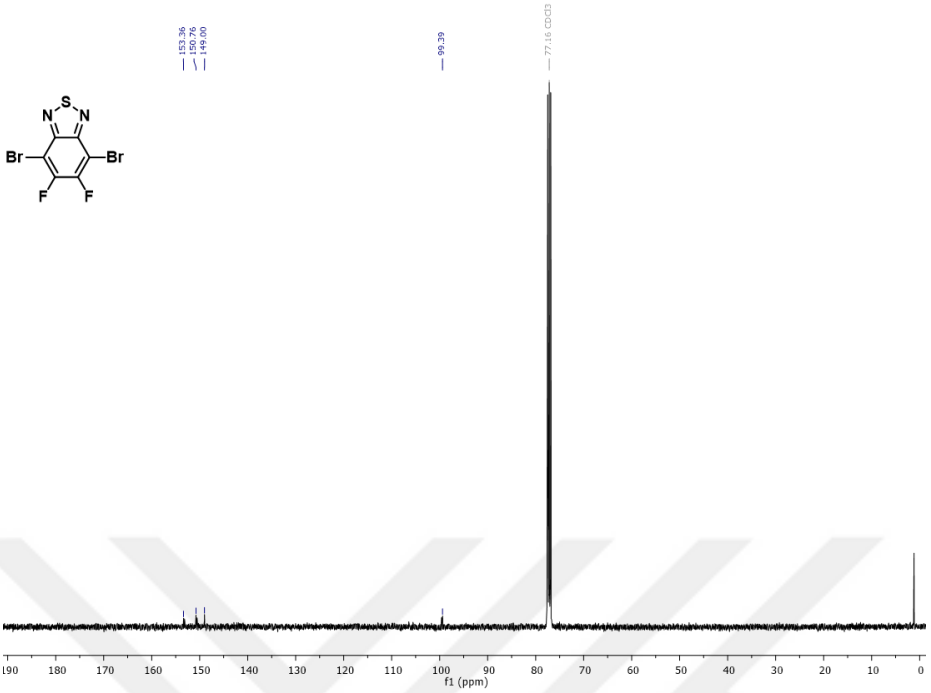


Figure A.8. ^{13}C NMR spectrum of **Molecule 14** in $CDCl_3$

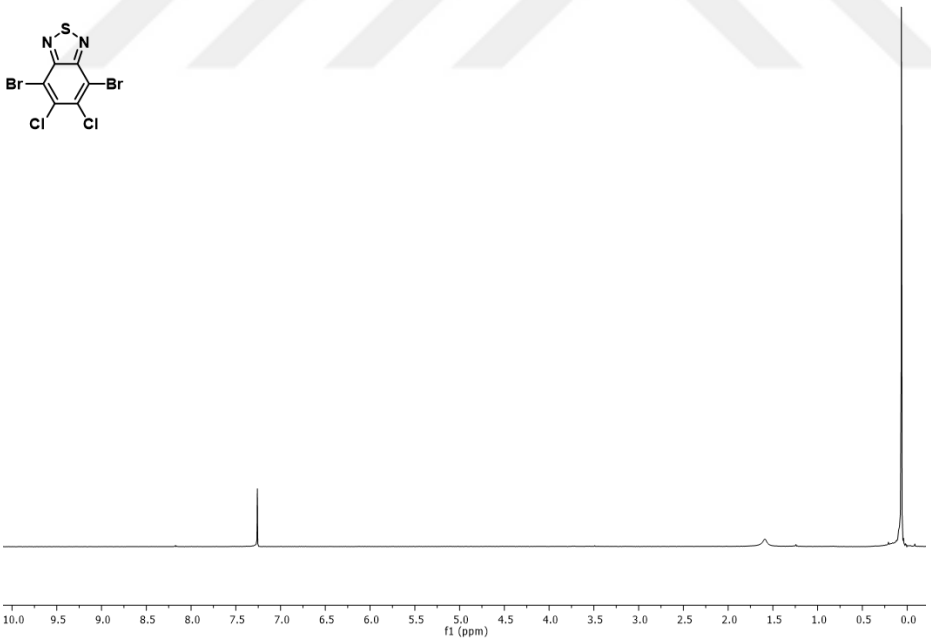


Figure A.9. ^{1}H NMR spectrum of **Molecule 15** in $CDCl_3$

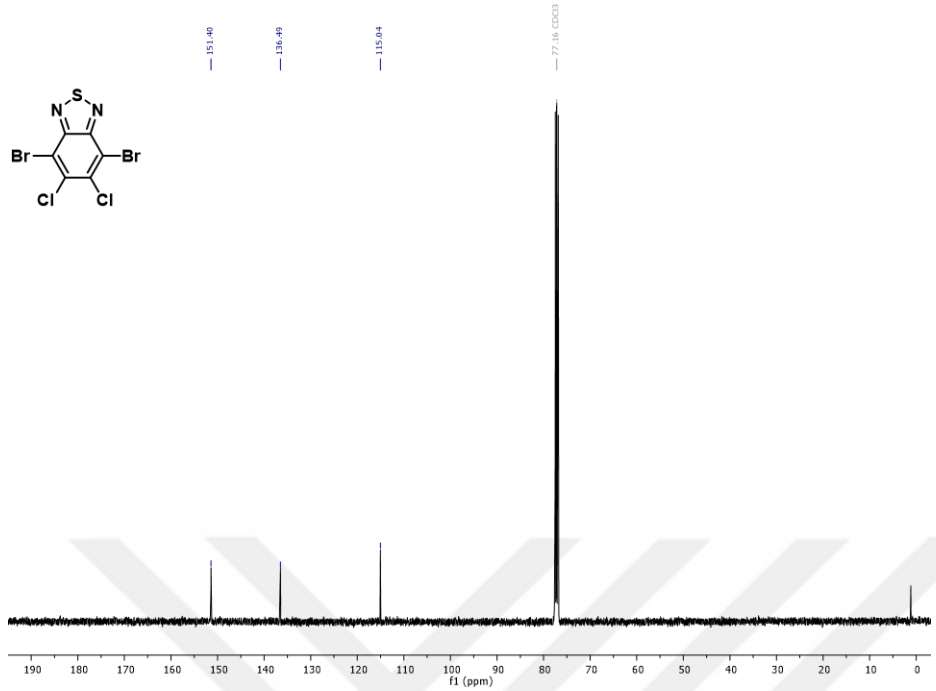


Figure A.10. ^{13}C NMR spectrum of **Molecule 15** in $CDCl_3$

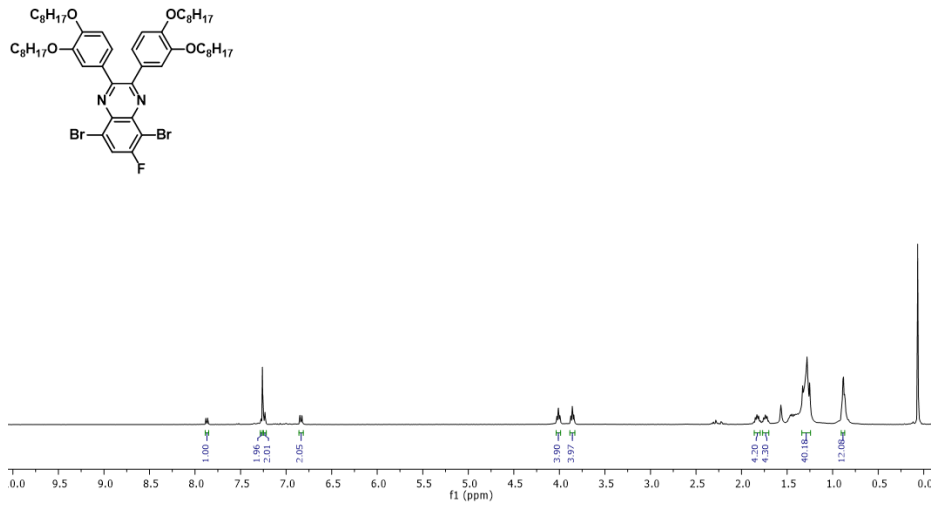


Figure A.11. ^{1}H NMR spectrum of **Molecule 19** in $CDCl_3$

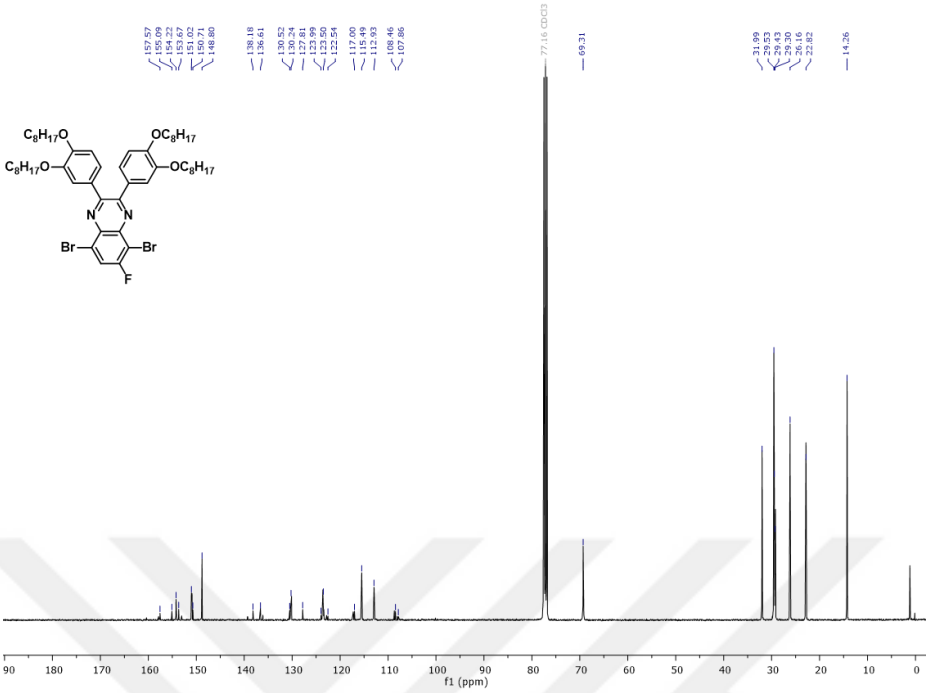


Figure A.12. ^{13}C NMR spectrum of **Molecule 19** in $CDCl_3$

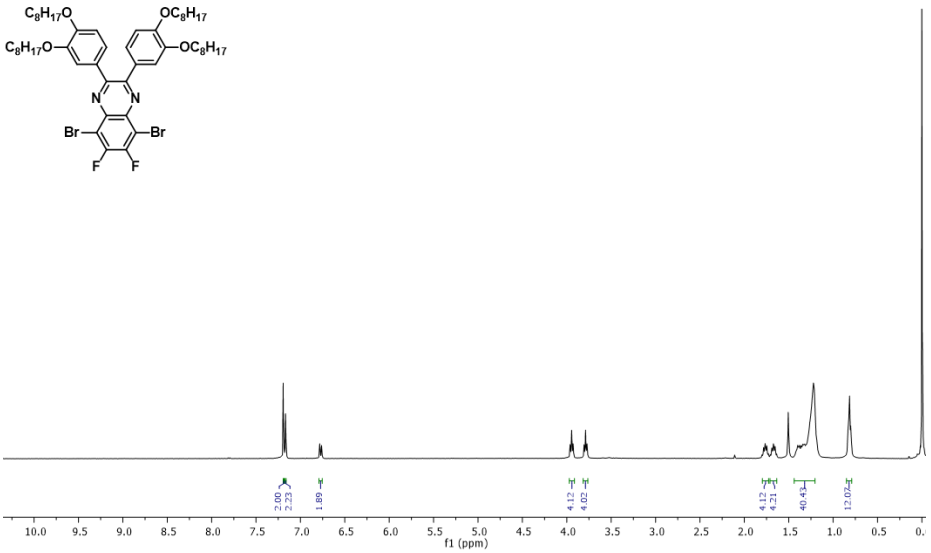


Figure A.13. ^{1}H NMR spectrum of **Molecule 20** in $CDCl_3$

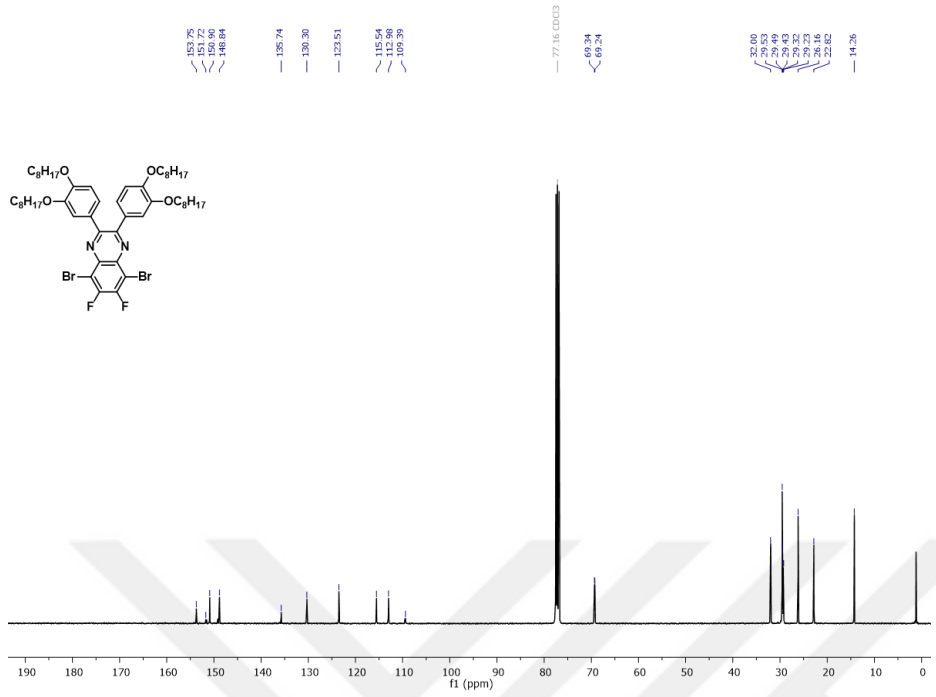


Figure A.14. ^{13}C NMR spectrum of **Molecule 20** in $CDCl_3$

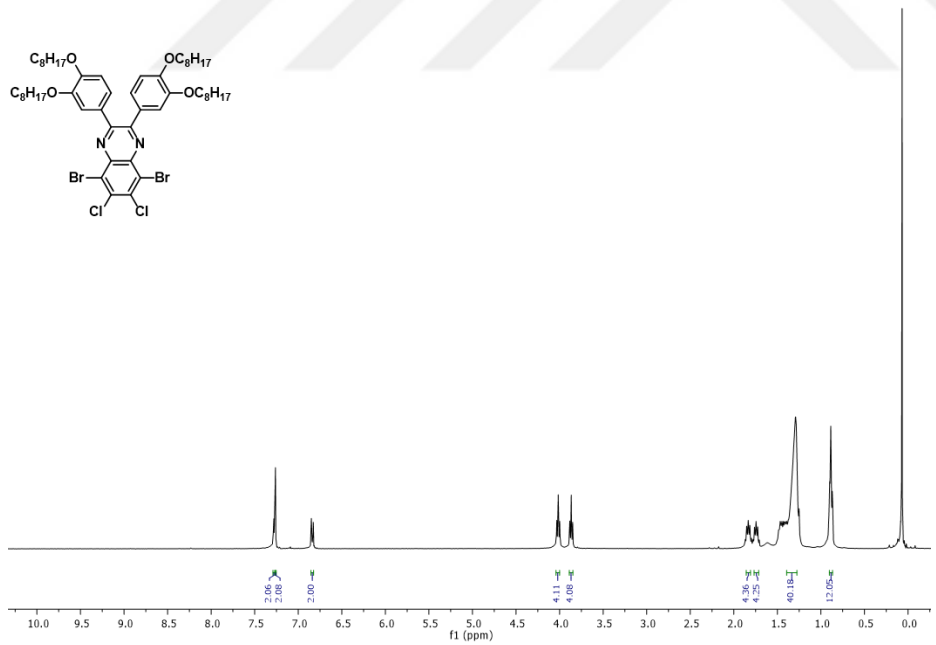


Figure A.15. ^{1}H NMR spectrum of **Molecule 21** in $CDCl_3$

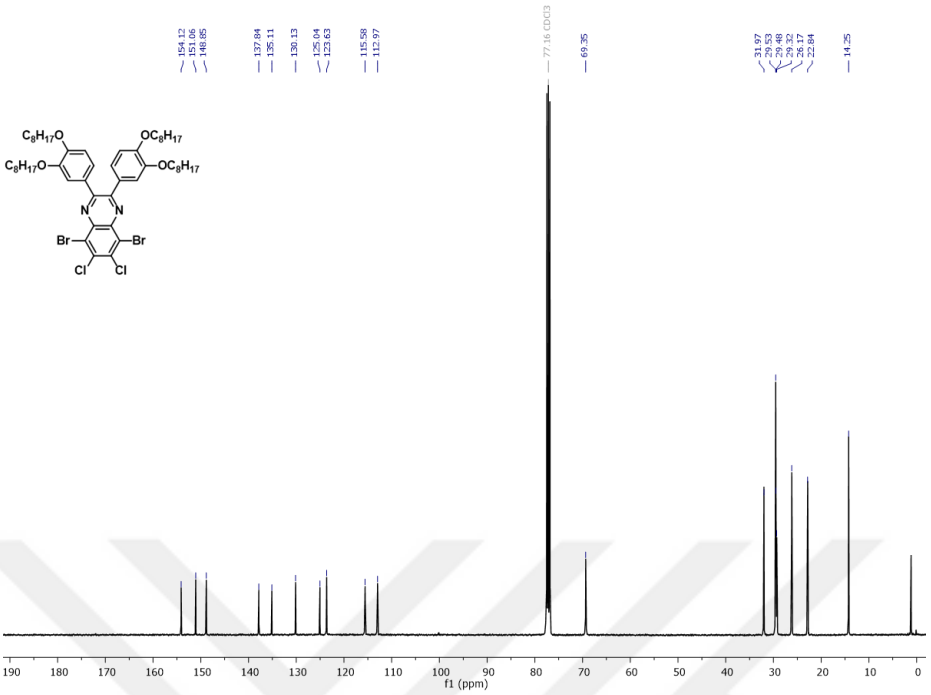


Figure A.16. ^{13}C NMR spectrum of **Molecule 21** in $CDCl_3$

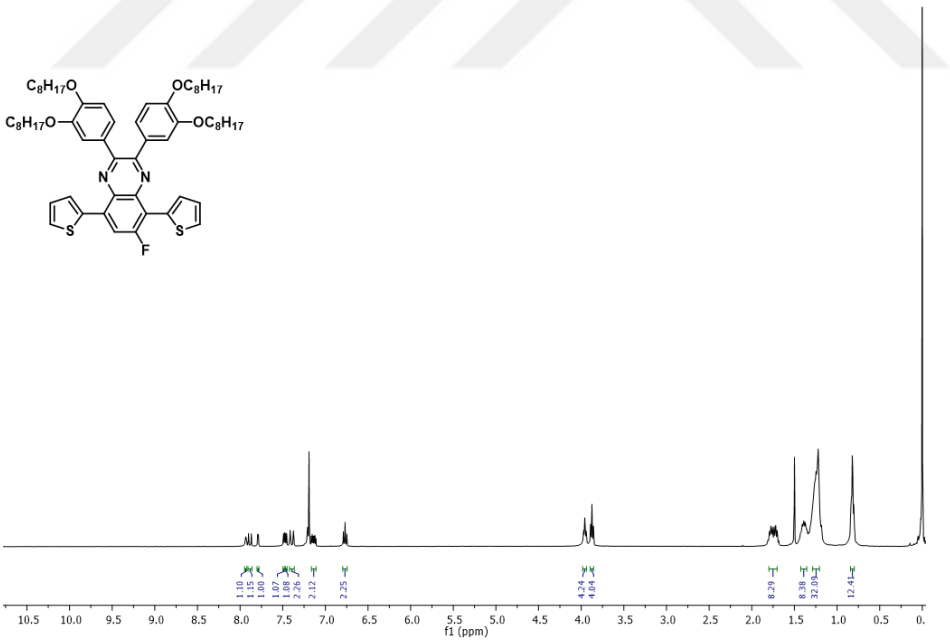


Figure A.17. ^{1}H NMR spectrum of **Molecule 22** in $CDCl_3$

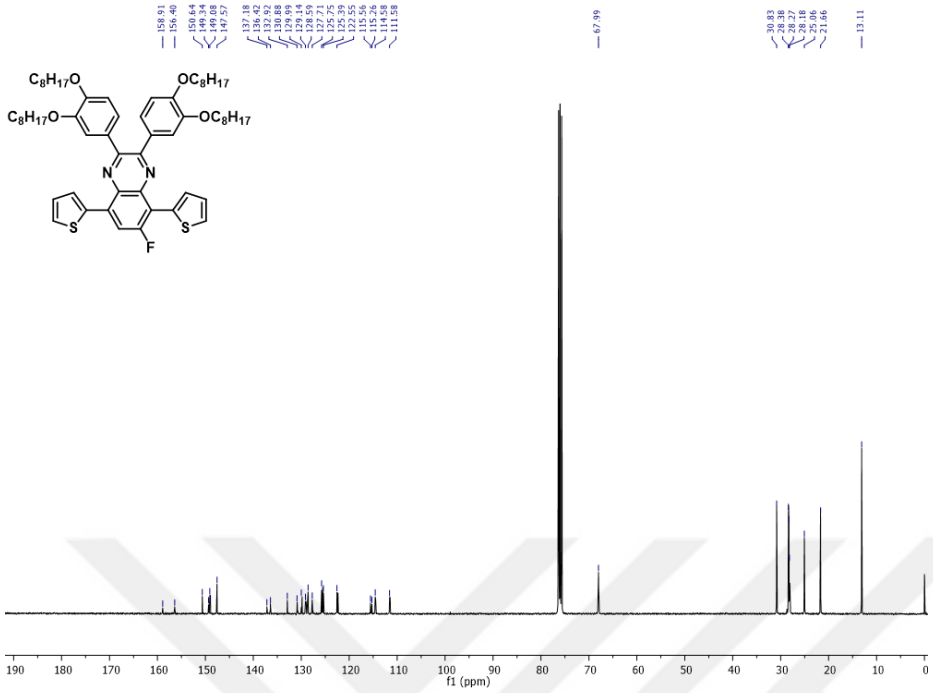


Figure A.18. ^{13}C NMR spectrum of **Molecule 22** in $CDCl_3$

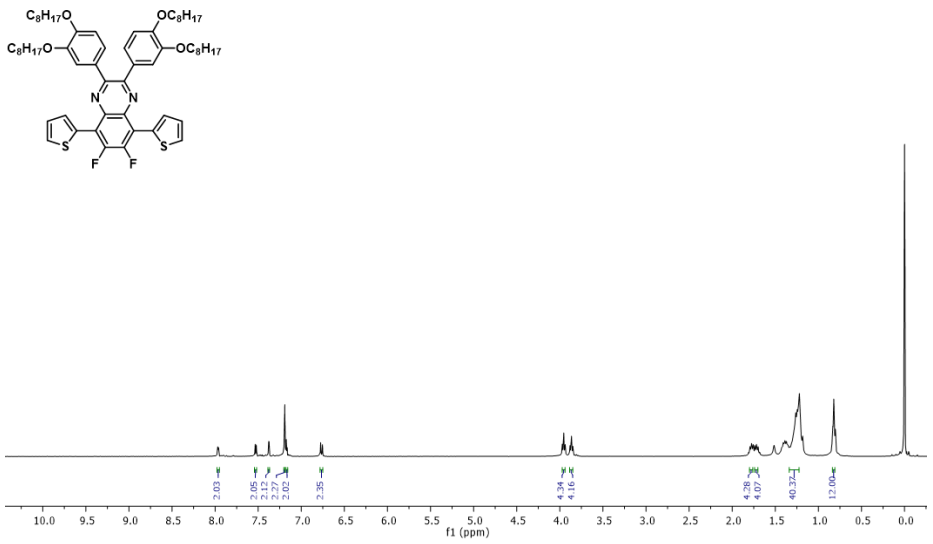


Figure A.19. ^{1}H NMR spectrum of **Molecule 23** in $CDCl_3$

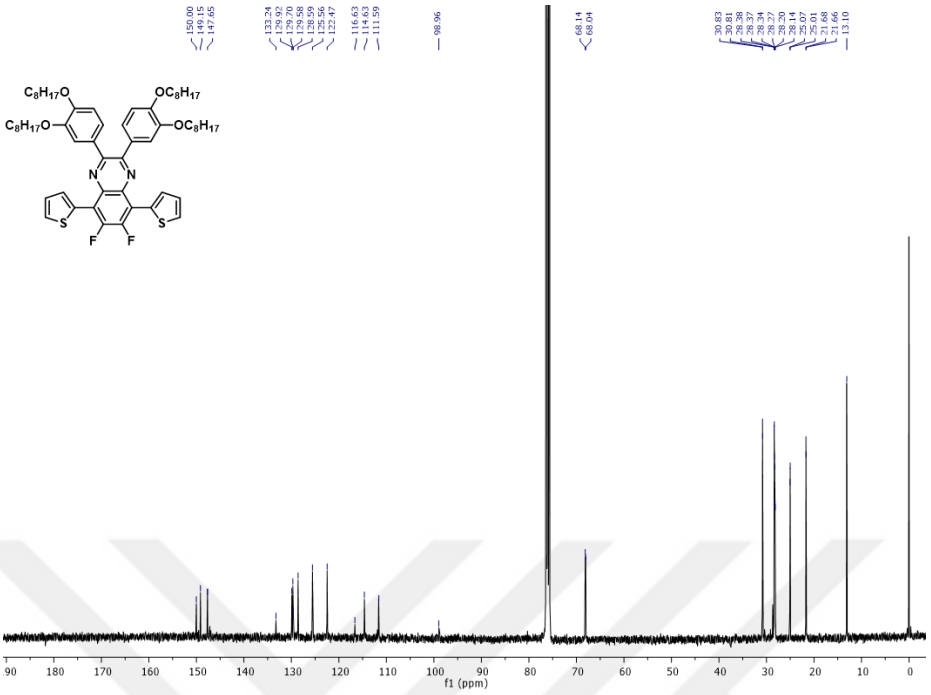


Figure A.20. ^{13}C NMR spectrum of **Molecule 23** in $CDCl_3$

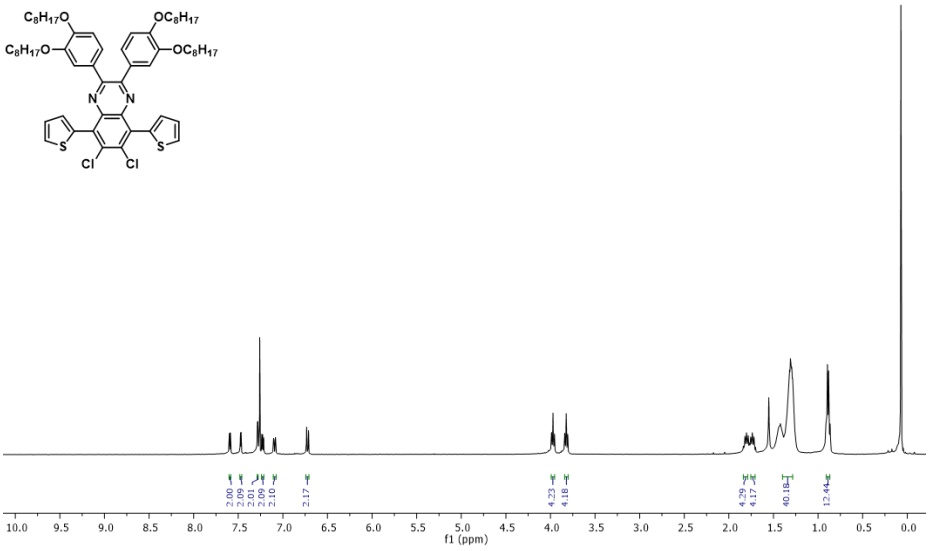


Figure A.21. ^{1}H NMR spectrum of **Molecule 24** in $CDCl_3$

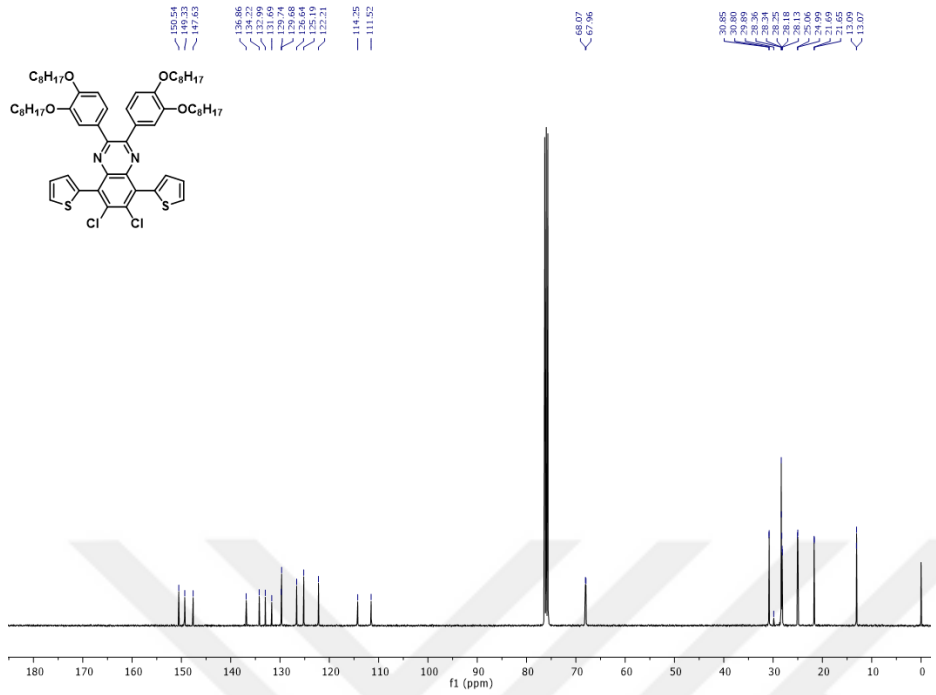


Figure A.22. ^{13}C NMR spectrum of **Molecule 24** in $CDCl_3$

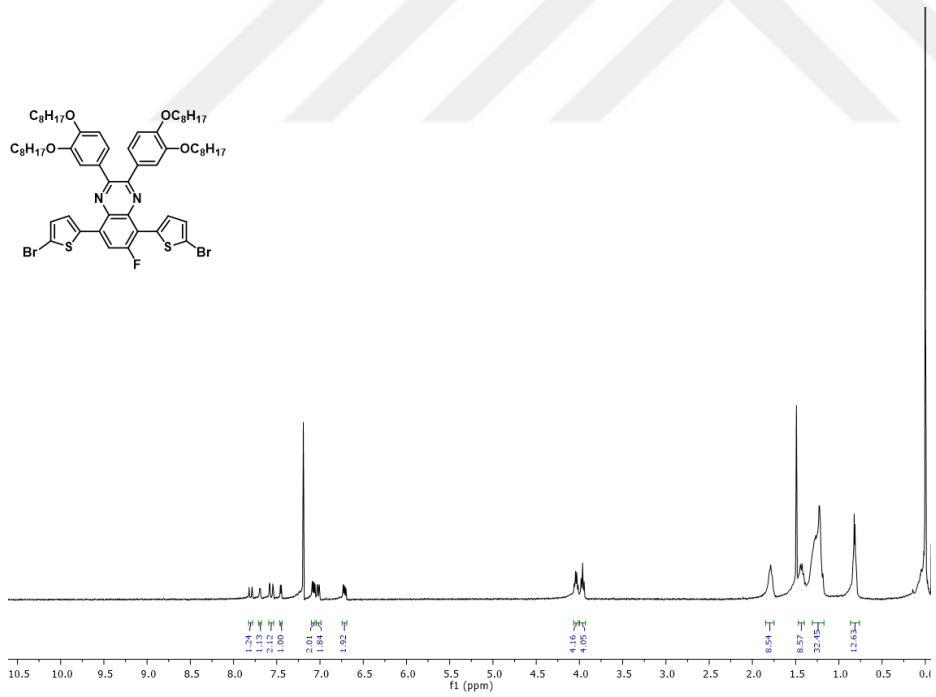


Figure A.23. ^{1}H NMR spectrum of **Molecule 25** in $CDCl_3$

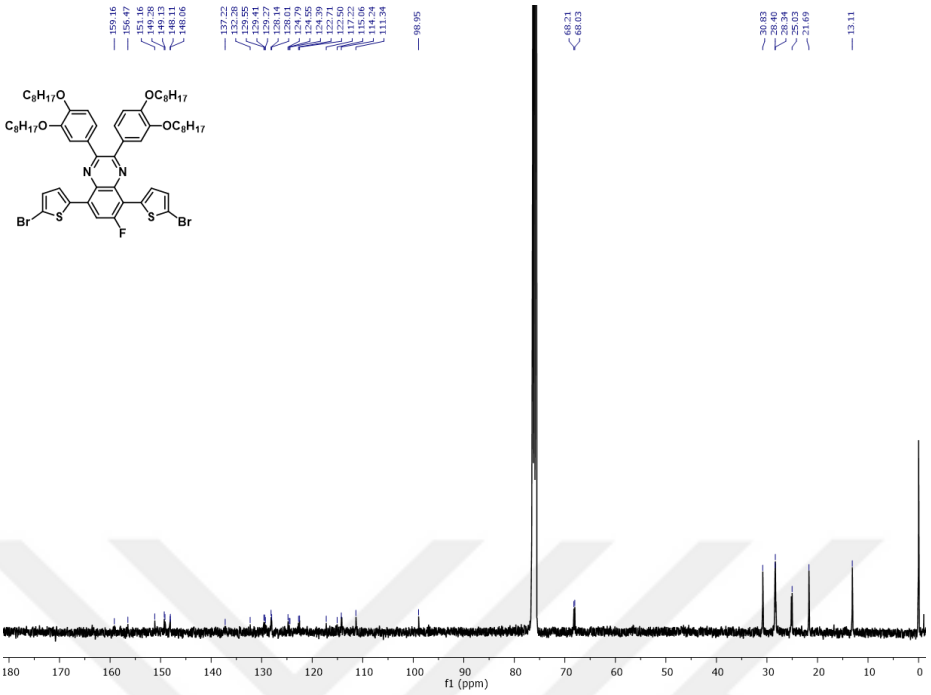
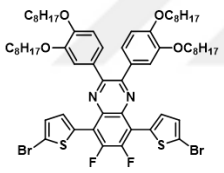


Figure A.24. ^{13}C NMR spectrum of **Molecule 25** in $CDCl_3$



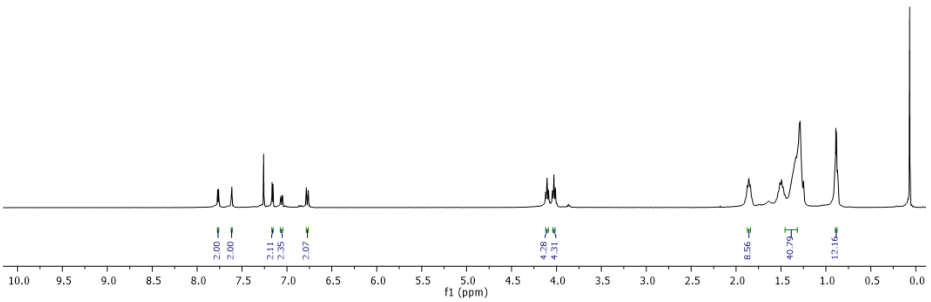


Figure A.25. ^{1}H NMR spectrum of **Molecule 26** in $CDCl_3$

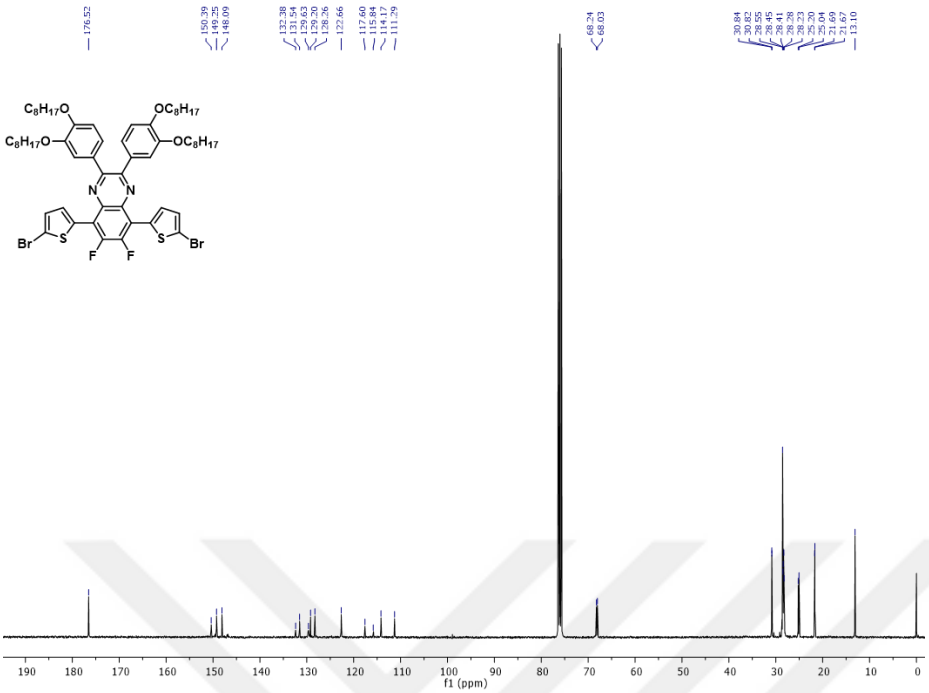


Figure A.26. ^{13}C NMR spectrum of **Molecule 26** in $CDCl_3$

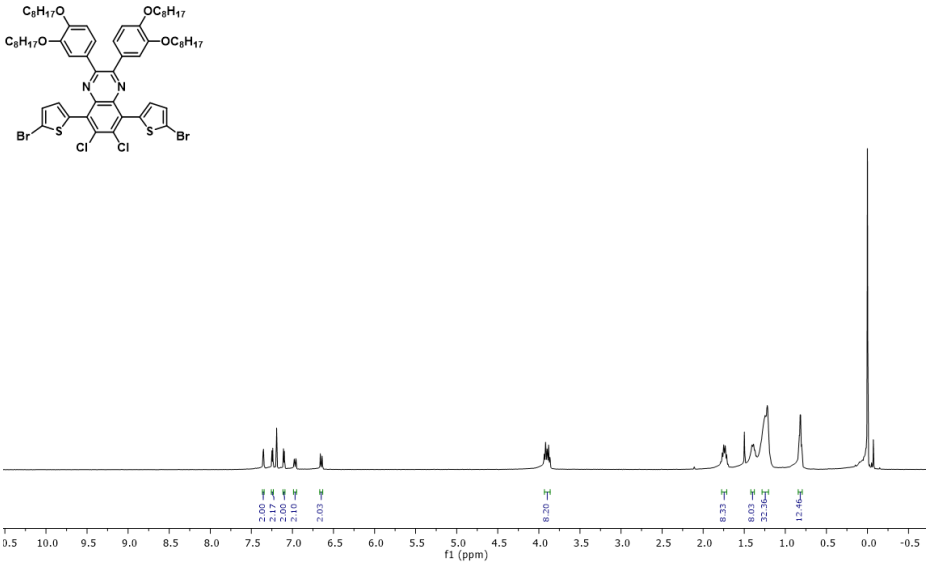


Figure A.27. ^{1}H NMR spectrum of **Molecule 27** in $CDCl_3$

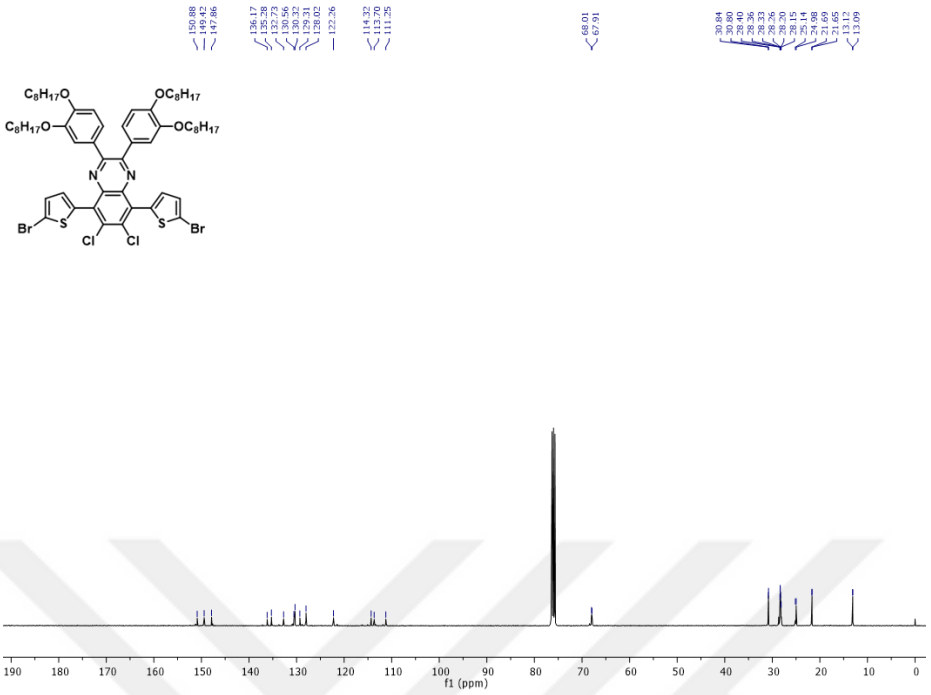


Figure A.28. ^{13}C NMR spectrum of **Molecule 27** in $CDCl_3$

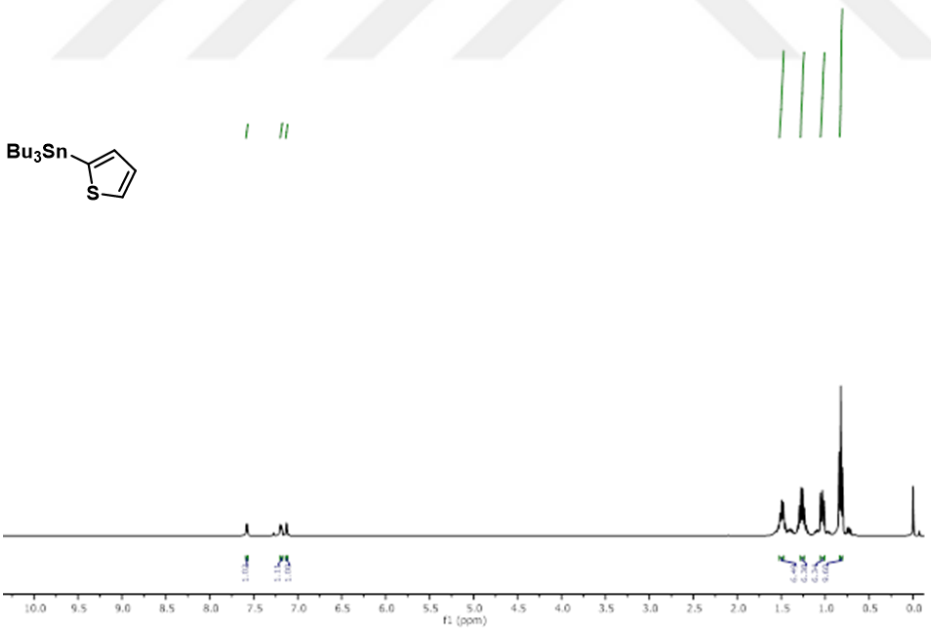
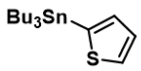


Figure A.29. ^{1}H NMR spectrum of **Molecule 29** in $CDCl_3$



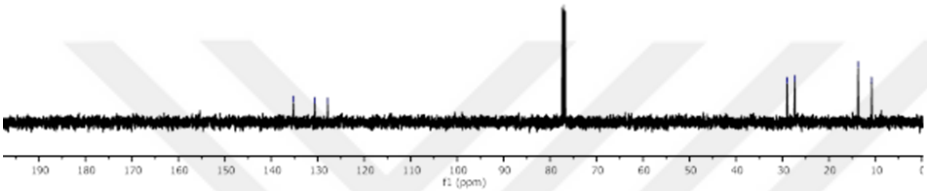
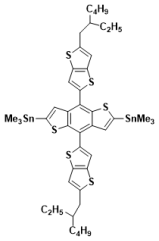


Figure A.30. ^{13}C NMR spectrum of **Molecule 29** in $CDCl_3$



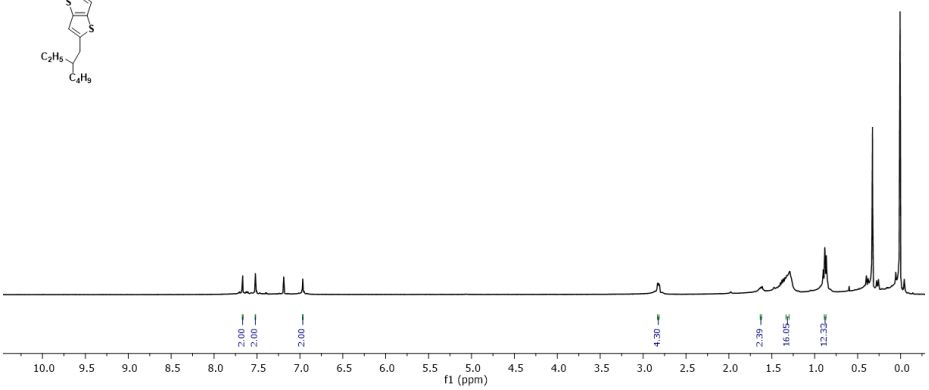


Figure A.31. ^{1}H NMR spectrum of **Molecule 31** in $CDCl_3$

High Resolution Mass Spectrometry

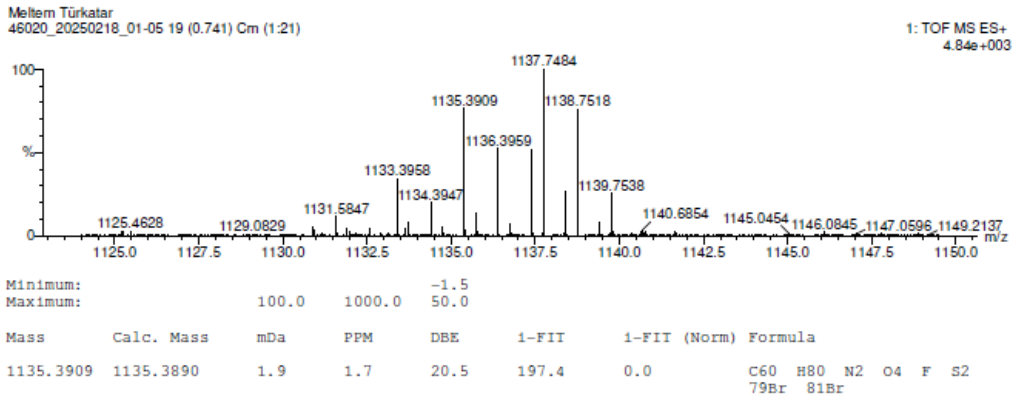


Figure A.32. HRMS spectrum of **Molecule 25**

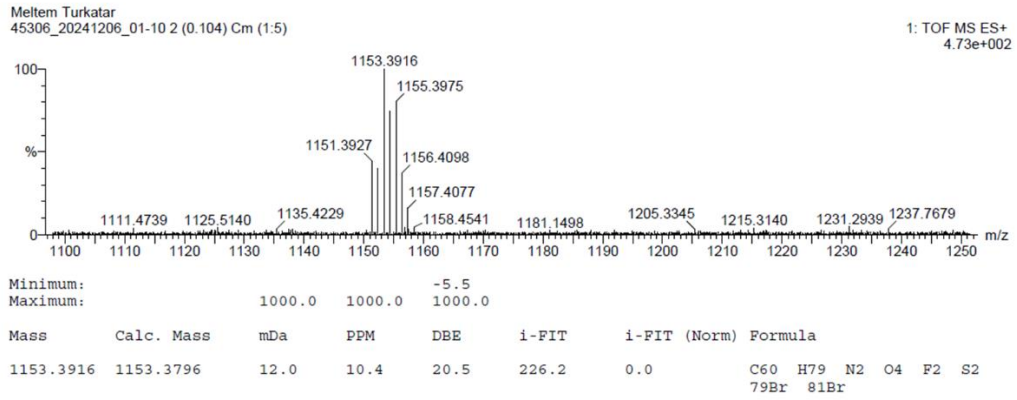
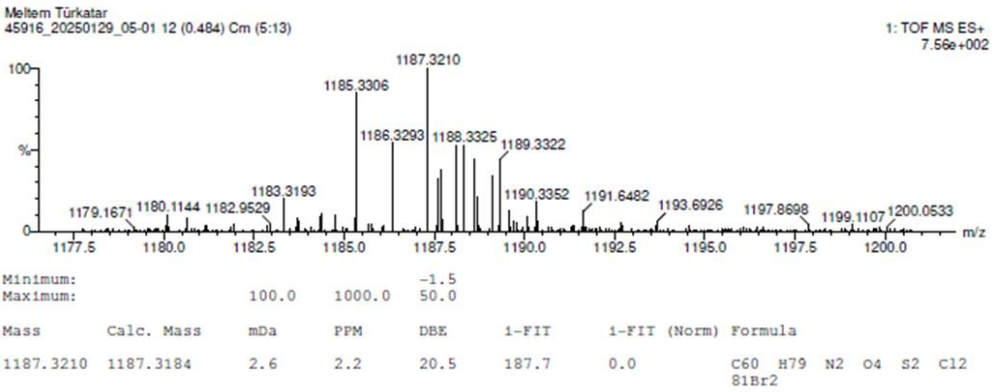


Figure A.33. HRMS spectrum of **Molecule 26**



Minimum:				-1.5			
Maximum:		100.0	1000.0	50.0			
Mass	Calc. Mass	mDa	PPM	DBE	i-FIT	i-FIT (Norm)	Formula
1187.3210	1187.3184	2.6	2.2	20.5	187.7	0.0	C60 H79 N2 O4 S2 Cl2 81Br2

Figure A.34. HRMS spectrum of **Molecule 27**

Thermogravimetric Analysis

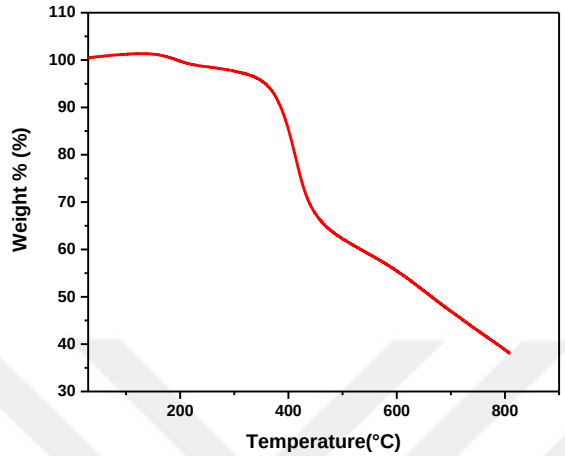


Figure A.35. Thermogram of **P1**

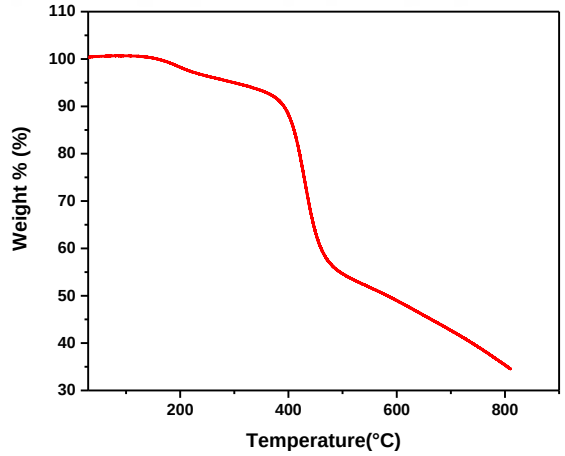


Figure A.36. Thermogram of **P2**

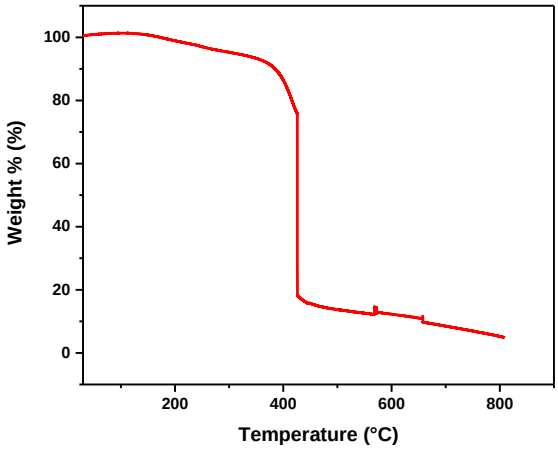


Figure A.37. Thermogram of **P3**

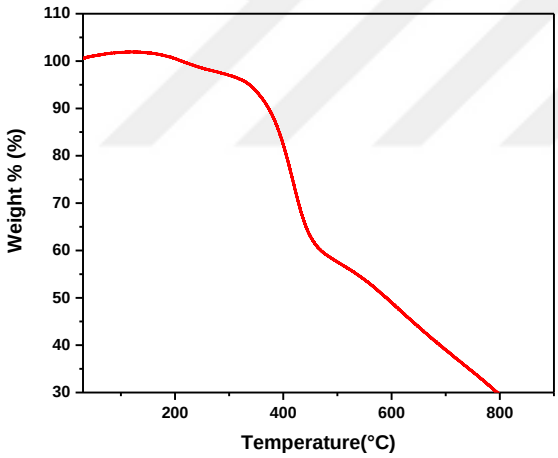


Figure A.38. Thermogram of **P4**

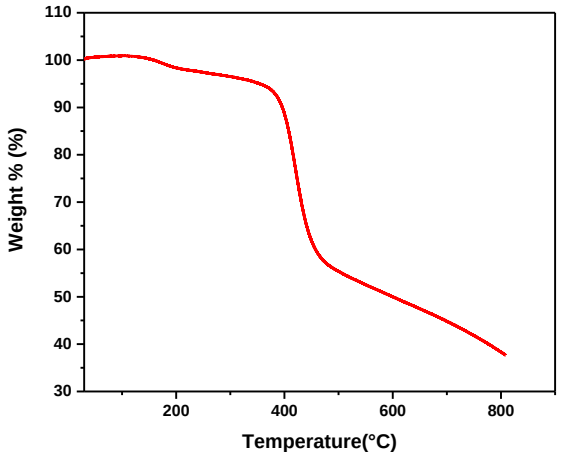


Figure A.39. Thermogram of **P5**

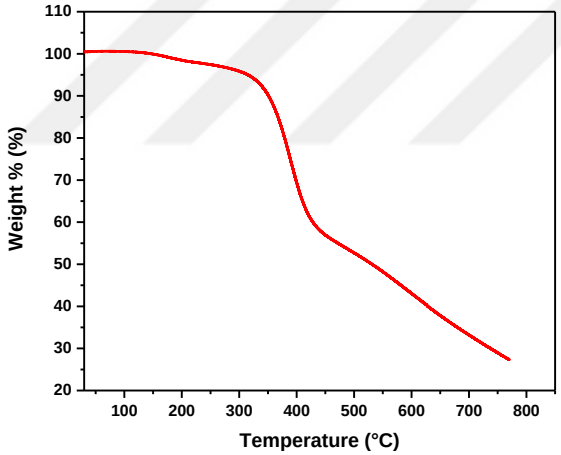


Figure A.40. Thermogram of **P6**